Characterisation of AlInAsSb Photodiodes and Type-II InGaAs/GaAsSb Superlattice Photodiodes

Yuting Ji

A thesis submitted in fulfilment of the requirements for the degree of

Doctor of Philosophy

Department of Electronic and Electrical Engineering

The University of Sheffield

July 2022

Acknowledgements

First and foremost, I would like to express my deepest gratitude to my supervisor, Prof. Jo Shien Ng for her endless guidance, supervision and encouragement throughout my Ph.D journey. I also wish to express my gratitude to Prof. Chee Hing Tan and Prof. John David, for their insightful remarks and suggestions.

I would like to thank entire members of the Impact Ionisation group, past and present, especially Dr. Leh Woon Lim, Dr. Jonathan Petticrew, Dr. Vladimir Shulyak, Jonathan Taylor-Mew, Dr. Elizabeth Stark, Dr Benjamin White, Dr. Simon Dimler, Dr. Lucas Pinel, Dr. Salman Abdullah, Tarick Osman, Nada Adham, Mohammad Riduwan, Yifan Liu, Dr. Yuchen Liu, Dr. Xin Yi and Dr. Jeng Shiuh Cheong for their friendship, and enriching my experience throughout my Ph.D. Thank you so much to all EEE departmental staffs for helping out in every aspect to finish my study.

I am thankful to Prof. Mark Hopkinson's MBE group and III-V lab for their help in growing the wafers used in this thesis.

To my dear parents and brother, your moral and financial support during these number of years, has allowed me to complete my studies.

Abstract

Photodiodes operating in the short wavelength range of 1 - 3 μm are essential in many applications with significant societal benefits. Example applications include short wavelength infrared imaging, remote gas detection, and non-invasive optical blood glucose monitoring. Hence, development of SWIR photodetectors with good performance has been an area of active research in the past few decades. This thesis presents experimental investigations on two detector materials suitable for this wavelength range, which are InGaAs/GaAsSb type-II superlattice (lattice matched to InP substrates) and $Al_{0.1}In_{0.9}As_{0.83}Sb_{0.17}$ (lattice-matched to GaSb substrates).

Two MBE grown InGaAs/GaAsSb type-II superlattice *p-i-n* wafers contained strained and lattice matched $GaAs_{1-x}Sb_x$ (x = 0.49 and 0.40) are reported. Optical and electrical characterisations of the devices are performed. Both devices exhibited room temperature cutoff wavelength of ~ 2 μm. Temperature dependence of cut-off wavelength was extracted from photoresponse data between 200 K and room temperature. These results along with literature were then used to validate a nextnano model for temperature dependent cutoff wavelength of T2SL. Good agreement across the temperature range was demonstrated for both lattice matched and strained T2SL after correcting the GaAsSb valance band offset bowing parameter from 0 to -1.06 eV. Nevertheless, these low type-II superlattice photodiodes exhibit relatively low quantum efficiency, leading to an experimental investigation on $Al_{0.1}In_{0.9}As_{0.83}Sb_{0.17}$, so that the photodiode uses a bulk material for photon absorption.

The work $Al_{0.1}In_{0.9}As_{0.83}Sb_{0.17}$ was carried out to establish the relationship between the impact ionisation coefficients, since it has been used as the absorber material in Separate-Absorption-Multiplication Avalanche Photodiodes (SAM APD) competitive avalanche material in an APD. The work used homojunction diodes with 2 and 4 μm nominal intrinsic region widths. Dark current, capacitance, and avalanche gain versus reverse bias as functions of temperatures for $Al_{0.1}In_{0.9}As_{0.83}Sb_{0.17}$ were measured. Using

three laser wavelengths to produce three carrier injection profiles, extensive avalanche gain data were obtained at three temperatures. The data show that electron ionisation coefficient, α, is larger than hole ionisation coefficient, β. Hence, when $Al_{0.1}In_{0.9}As_{0.83}Sb_{0.17}$ is used as the absorber material in SAM APD, the avalanche material used should also have $\alpha > \beta$, in order to avoid degradation in the SAM APD excess noise performance.

List of Publications

Journal paper in preparation

J. Petticrew, **Y. Ji**, I. S. Han, B. White, A. Evirgen, J. Reverchon, M. Hopkinson, C. H. Tan, and J. S. Ng, "Temperature dependent cut-off wavelength of InGaAs/GaAsSb Type-II Superlattices"

Conference

Y. Ji, J. Petticrew, L. W. Lim, C. H. Tan, and J. S. Ng, "Short-wave infrared $Al_{0.1}In_{0.9}As_{0.83}Sb_{0.17}$ Photodiodes", Semiconductor and Integrated Optoelectronics (SIOE), Cardiff, Apr. 2022.

J. Petticrew, **Y. Ji**, I. S. Han, B. White, C. H. Tan, M. Hopkinson, and J. S. Ng, "Asymmetric-strained InGaAs/GaAsSb Type-II Superlattice Photodiodes for SWIR detection", Semiconductor and Integrated Optoelectronics (SIOE), Cardiff, Apr. 2022.

Glossary -List of symbols

A	Area of device
α_{abs}	Optical absorption coefficient
α	Electron impact ionisation coefficient
β	Hole impact ionisation coefficient
$\forall$	Pre-exponential factor of Arrhenius equation
c	Speed of light
C	Capacitance
C_j	Junction capacitance
D	Diffusion constant
E_A	Activation energy
E_g	Bandgap energy
E_{field}	Electric field strength
E_{ph}	Photon's energy
E_{th}	Impact ionisation threshold energy
ε_0	Vacuum permittivity
ε_r	Relative permittivity pf material
f_{-3dB}	-3 dB bandwidth
h	Planck's constant
$\hbar$	Reduced Planck's constant
$I(x)$	Intensity of light
$I_{(x=0)}$	Initial intensity of light
I_{ph}	Photocurrent
I_B	Current from background radiation
I_D	Dark current
I_f	Forward current
I_0	Saturation current
I_{bulk}	Bulk current
I_{diff}	Diffusion current
$I_{g\text{-}r}$	Generation-recombination current
I_{pri}	Primary current

I_{surf}	Surface current
I_{tun}	Tunnelling current
J	Current density
k_B	Boltzmann's constant
L	Minority carrier diffusion length
λ	Wavelength
λ_c	Cutoff wavelength
M	Multiplication factor
M_e	Pure electron multiplication factor
M_h	Pure hole multiplication factor
m_e	Carrier effective mass
n	Ideality factor
n_i	Intrinsic carrier concentration
$N_{A,D}$	Acceptor/hole doping concentration
η	Quantum efficiency
η_{ext}	External quantum efficiency
P_{opt}	Optical power
q	Electron charge
R	Responsivity
R_L	Load resistance
R_{eq}	Equivalent resistance of the amplifier
R_s	Series resistance
R_{shunt}	Shunt resistance
r	Radius of device
σ_{tun}	Tunnelling parameter
T	temperature
τ_r	The carrier's transit time
τ_{eff}	Effective carrier lifetime
V_{bi}	Built-in voltage
V	Voltage
v	Frequency of light
v_s	Carrier saturation velocity
W_D	Depletion region

Contents

1. Introduction

Over the past five decades, applications as diverse as light detection and ranging (LiDAR) [1], telecommunication [2], medical and environmental imaging, and astronomy [3] have come to rely heavily on light detection. Photodiodes are the vital components to convert incoming optical signal power into electrical signal current in these systems. Within the electromagnetic spectrum (Figure 1.1), the optical signals of concern in this work are infrared light, which are utilised in a wide range of applications ranging from commercial, military, and research. Unlike visible light imaging ranging from 400 to 700 nm imaging in infrared wavelength can convey information without being perceivable by the human eyes. To date, no single photodetector could efficiently detect the radiation which covers the entire electromagnetic spectrum range without exhibiting excessive noise, so different materials are utilised to produce high-sensitivity photodetectors for detection of light at different wavelength bands.

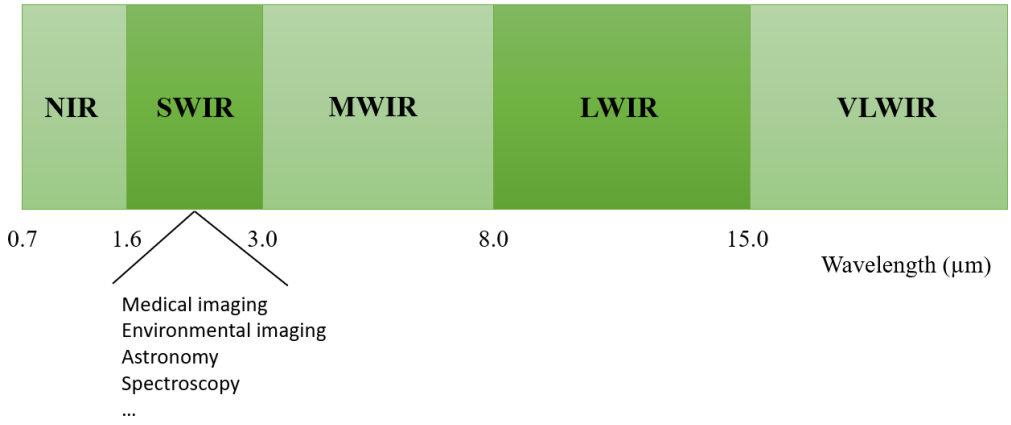

Figure 1.1: Infrared bands within the electromagnetic spectrum.

The infrared radiation band from 0.7 μm to 30 μm is usually divided into the following bands:

- near-infrared (NIR) for 0.7 – 1.6 μm
- short-wave infrared (SWIR) for 1.7 - 3 μm
- mid-wave infrared (MWIR) for 3 – 8 μm
- long-wave infrared (LWIR) for 8 – 15 μm
- very long-wave infrared (VLWIR) for 15 μm onwards

The NIR band is essential for fibre-based optical communication systems [4]. The first generation of optical fibre communication systems operated in the 800 - 900 nm wavelength range, by utilising $Al_xGa_{1-x}As$ lasers (on GaAs substrates) and Si optical receivers [5]. Following improvements in manufacturing of high purity silica fibres, the preferred wavelengths of operations shifted to ~ 1.31 and 1.55 µm. They coincide with optical attenuation loss minimum points for silica fibres as well as being less affected by Rayleigh scattering (compared to the shorter wavelengths of 800 - 900 nm). Consequently, the photodetectors for fibre-based optical communication systems must be sensitive to light with wavelength up to 1.55 µm. $In_{0.53}Ga_{0.47}As$, a III-V semiconductor material with a 0.75 eV bandgap energy at room temperature (corresponding to a 1.7 µm cutoff wavelength, λ_c) and is lattice-matched to InP substrates [2], satisfy this need. Hence $In_{0.53}Ga_{0.47}As$ is the dominant optical absorption material in photodetectors for fibre-based optical communication systems operating from 1.3 to 1.6 µm.

Just outside the NIR band, there has been increasing interest into SWIR range at ~ 2 µm from applications such as short wavelength infrared imaging [6] and remote gas detection [7]**.** Over the past century, increasing greenhouse gases concentration in the earth's atmosphere has contributed towards climate change, as stated in various reports from Intergovernmental Panel on Climate Change [8]. The most potent greenhouse gases are ozone (O_3), carbon dioxide (CO_2), methane (CH_4), and nitrous oxide (N_2O), whose absorption peaks are mainly located within the range of 1.5 – 4 µm [9]–[15]. Therefore, utilising SWIR band for atmospheric light detection and ranging (LiDAR) [16] to achieve remote detection of greenhouse gases have been proposed. In addition, researchers have explored medical diagnostic applications in the SWIR range, such as non-invasive optical blood glucose monitoring (2.0 - 2.5 µm) [17]. Therefore, SWIR photodetectors with good performance are of importance to many applications with significant societal benefits.

The aim of this work was to investigate materials/structures suitable for SWIR band detection, mainly focusing on two SWIR detector technologies, InGaAs/GaAsSb T2SL grown on InP substrates and AlInAsSb grown on GaSb substrates.

1.1. Literature review

The ideal SWIR photodiode exhibits high quantum efficiency for light detection, low dark current, low capacitance, and low noise at room temperature. In addition, its manufacturing process is straightforward so is low cost. Currently, competing SWIR photodiode technologies rely on a number of semiconductor materials, including Mercury Cadmium Telluride (HgCdTe or MCT), InAs, extended-InGaAs, InGaAs/GaAsSb type-II superlattice (T2SL) and AlInAsSb. Each technology satisfies the long list of desired photodiode properties to a different extent, but none satisfies the entire list.

1.1.1. Mercury Cadmium Telluride (MCT) photodiodes

The alloy MCT is made up of II-VI materials and its composition can be altered to achieve the desired band gap (from - 0.3 to 1.6 eV). Following decades of developments, MCT has emerged as the almost ideal material for infrared photodiodes. MCT photodiodes offer excellent detectivity compared to other competing SWIR photodiodes, with some devices reaching nearly 100% [18]. Currently, commercially available MCT photodiodes of different compositions offer continuous λ_c coverage from SWIR to LWIR band. Depending on the manufacturers, they are grown on nearly lattice matched CdZnTe (CZT) substrates or GaAs substrates [19]. CdZnTe substrates are costly and limited in size, compared to the GaAs substrates. Hence MCT photodiodes grown on GaAs substrates are more technologically advanced.

Early research in MCT photodiodes was initiated by Lawson *et al.* in 1959, which reported that the absorption edge of HgCdTe varies from 0.8 µm in wide-bandgap pure CdTe to 13 µm in the mixed HgTe-CdTe as mercury fraction of 0.9 [20]. Research efforts soon focused on photodiodes for detection at 3 - 5 µm and 8 - 14 µm, the atmospheric transmission windows, which are crucial for passive IR imaging applications. The first-generation HgCdTe detector system used a scanning system with single-element detector. In 1970s, small two-dimensional (2-D) focal plane arrays (FPAs) with > 1 million pixels were introduced [21].

Significant improvements in MCT photodiode performance were achieved when more complicated, efficient photodiode design, such as double-heterostructure *p-i-n* diode, was adopted [22]. Commercially available MCT photodiodes with low dark current and low noise

are now available in formats up to 4096 × 4096 are available from several suppliers worldwide [23].

Later, feasibility of SWIR HgCdTe APDs with low excess noise for astronomy applications was investigated. An example is SAPHIRA linear mode APD arrays [24]. HgCdTe APDs with λ_c of 3 µm on a 30 µm pitch 320 × 526 FPA were reported to achieve a mean gain of 7.5 at -6.3 V bias voltage for temperature < 110 K [25]. Linear arrays of HgCdTe APDs in λ_c of 4.34 µm with 64 µm pitch pixels were demonstrated with high gain of 852 and low dark current density of 3.4 nA/cm^2 at - 12.5 V and 77 K [26].

MCT photodiodes require cryogenic cooling (down to 80 – 100 K) to suppress their dark currents. Other than cryogenic operation temperature, there are some other considerable disadvantages associated with MCT photodiodes, including high specialised manufacturing technologies [27], limited suppliers [19], high substrate cost (if using CdZnTe) as well as restrictions of mercury (Hg) and cadmium (Cd) use. Therefore, MCT photodiodes are restricted to specific applications for space and military applications that could afford the relatively high cost [28].

1.1.2. InAs

InAs is a III-V semiconductor material with a direct bandgap of ~ 0.35 eV (λ_c ~ 3.5 µm) at room temperature. InAs photodiodes have been investigated for a range of applications including radiation thermometry [29] and X-ray detection [30]. Over the years, InAs epitaxial growth method have developed from liquid phase epitaxy (LPE) [31] to molecular beam epitaxy (MBE) [32] and metal-organic vapour phase epitaxy (MOVPE) [33].

An early study of temperature-dependent electrical characteristics of InAs photodiode was carried out by Lucovsky [34] in 1961, using a p-n junction diode formed via Cd diffusion into an n-type InAs layer. Later reports using InAs *p-i-n* photodiodes [35], [36] showed that surface and bulk leakage currents reduced drastically with *i*-layer thickness and decreasing temperature (~ 6 orders of magnitude reduction from 300 to 40 K).

For InAs APDs, Mikhailova *et al.* provided the first estimates for InAs impact ionisation coefficients and showed that carrier multiplication in InAs occurs at relatively low electric field [37]. It is now well-established that the avalanche gain in InAs APDs is entirely derived from the impact ionisation of electrons [38], hence they are called ‘e-APDs’. The e-APD

characteristics exist at low temperature as well as room temperature [39], [40]. Such property gives rise to highly desirable APD performance characteristics including low excess noise [41] and gain-independent bandwidth [42].

Being a bulk semiconductor material, InAs photodiodes or APDs also offer high quantum efficiency for photon absorption. Peak responsivity of 1.28 A/W at 3.35 μm (corresponding to 48 % external quantum efficiency across the whole spectrum down to 0.633 μm) were reported for on InAs mesa photodiodes with 8 μm intrinsic region and λ_c of 3.55 μm operated at room temperature [29]. The dark current density is 0.35 A/cm^2 at - 0.5 V at room temperature. However, mesa InAs diodes fabricated using chemical wet etching produces varying bevel angles (depending on the etchants used), limiting the fill factor of small area diode arrays. Also, InAs APDs with mesa topology were insufficiently robust to endure repeated measurements at low operation temperatures, resulting in eventual degradation in device performance.

To improve device robustness and facilitate commercialisation, Be-ion implantation was used to produce individual pixels of planar InAs diodes [43] and InAs APDs [44]. So far, the best (lowest) dark current density achieved in these planar InAs diodes with 7 μm intrinsic regions is 0.52 A/cm^2 at – 0.2 V at room temperature [28], a factor of 3 lower than earlier planar InAs APDs produced using higher implantation energy [43]. The responsivity and EQE value at 1520 nm wavelength are 0.62 A/W and 50% at - 0.3 V.

1.1.3. Extended InGaAs

Photodiodes made with $In_{0.53}Ga_{0.47}As$ as the absorption material can only cover the optical spectrum up to 1.65 μm wavelength. Consequently, they cannot be used in SWIR band. An approach to extend the cutoff wavelength whilst using InGaAs was using strain-compensated InGaAs multiple quantum well (MQW) photodiodes [45]. The MQWs consisted of compressively strained $In_{0.83}Ga_{0.17}As$ wells and tensile strained $In_{0.83}Ga_{0.17}P$ barriers. The photodiode exhibited a single pass quantum efficiency of 30% and dark current of 130 pA (J_{dark} of 2.94 μA/cm^2) at - 5 V. This approach was abandoned when it became obvious that another approach, extended-wavelength InGaAs or extended InGaAs photodiodes (ex-InGaAs), produces more impressive quantum efficiency values.

Ex-InGaAs photodiodes are made with $In_xGa_{1-x}As$ with $x > 0.53$. Increasing the indium content beyond 0.53 reduces the bandgap of $In_xGa_{1-x}As$ to less than 0.75 eV, extending the operating

wavelength range into the SWIR band. Wafer growth of ex-InGaAs material takes advantages of fast epitaxy growth rate of Hydride Vapor Phase Epitaxy (HVPE) or MOVPE, both of which are mature wafer growth technologies. Different variants of extended InGaAs photodiodes with λ_c up to 2.6 µm are available commercially. The longer λ_c come from materials with smaller bandgaps, which bring higher bulk dark currents. There exists a clear tradeoff between dark current density and λ_c for ex-InGaAs is shown in Figure 1.2 using room temperature data from commercial ex-InGaAs photodiodes with different Indium compositions. As discussed in Section 1.1.1, 'Rule 07' is a simple empirical relationship used for comparing performances of infrared imagers with different λ_c and operation temperature [46]. It succeeds in predicting dark current densities for the best HgCdTe device cutoff wavelength-temperature products above 400 µm·K [47]. There ex-InGaAs photodiodes are ~ one order of magnitude higher than values obtained using Rule 07 at room temperature [47]. Figure 1.3 shows comparison of dark current densities at room temperature of ex-InGaAs photodiodes with different Indium compositions, *x*, which are similar to that of commercial ex-InGaAs photodiodes.

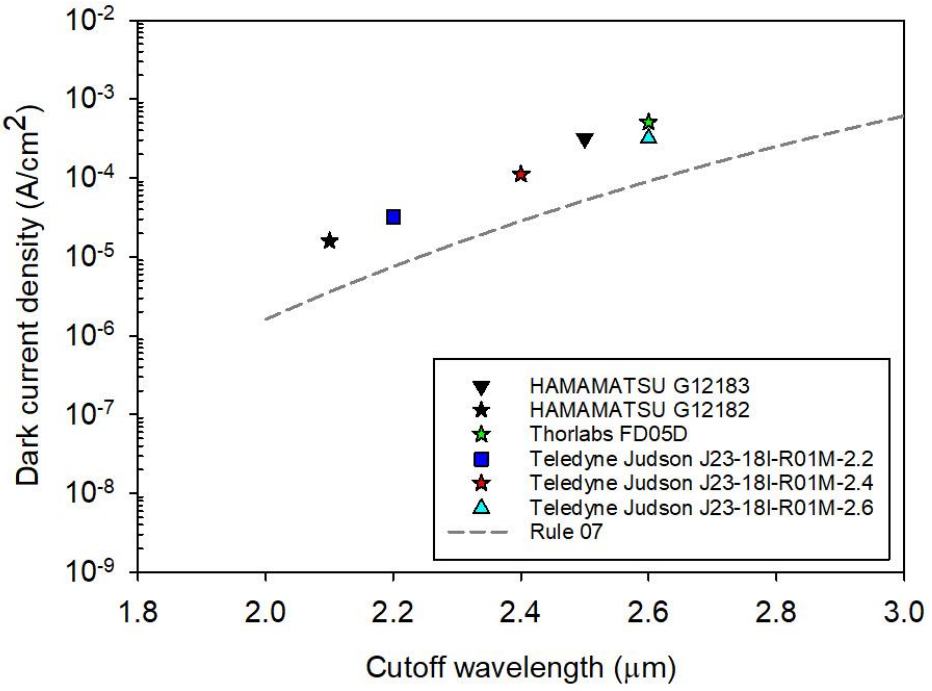

Figure 1.2: Comparison of dark current density vs cutoff wavelength for commercial ex-InGaAs photodiodes at - 0.5 V [48]–[51] to MCT Rule 07 at room temperature [47].

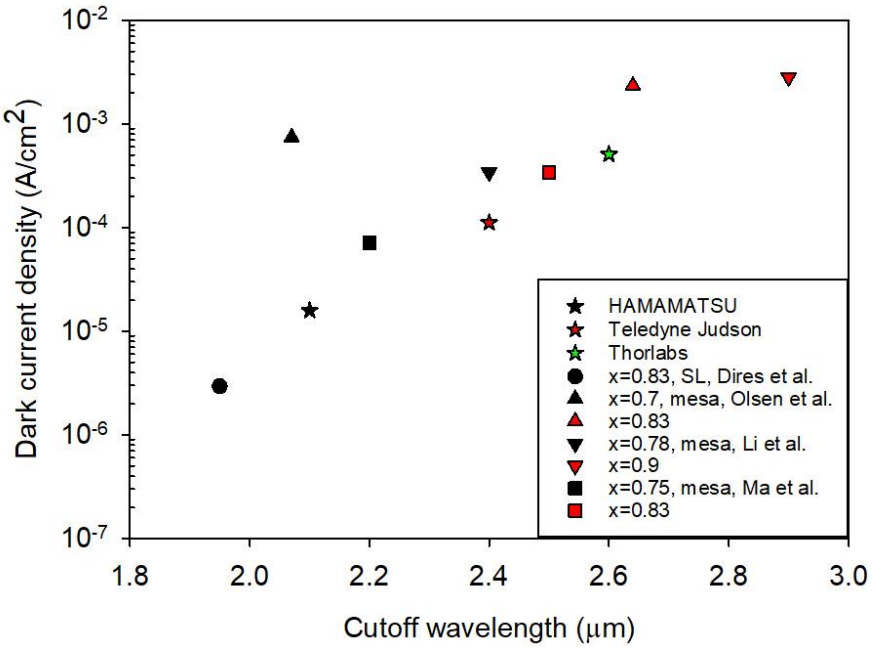

Figure 1.3: Comparison of dark current densities at room temperature of ex-InGaAs photodiodes with different Indium compositions, x, [45], [52]–[54].

In 1986, $In_{0.72}Ga_{0.28}As/In_{0.72}Al_{0.28}As$ heterojunction photodiodes with cutoff wavelength extending out to 2.4 μm were reported by Moseley *et al.* [55], with a responsivity of 1.31-1.58 A/W corresponding to a peak efficiency of ~ 95 % in the wavelength range of 1.6 - 2.2 μm. The dark current density at room temperature is 0.194 mA/cm^2 at - 0.5 V. Increasing the indium fraction $In_{0.82}Ga_{0.18}As$ photodiodes with cutoff wavelength of 2.65 μm were demonstrated with peak quantum efficiency of 75% at 2.55 μm [56]. However, the room temperature dark current density increased to 18 mA/cm^2 at - 0.5 V.

Later, ex-InGaAs photodiodes were developed with demonstration of a three-wavelength InGaAs FPA for operation wavelengths from 1.0 to 2.5 μm [52]. Each pixel consisted of active regions with three different InGaAs compositions, namely $In_{0.53}Ga_{0.47}As$, $In_{0.7}Ga_{0.3}As$ and $In_{0.85}Ga_{0.15}As$ (bandgaps of 0.75, 0.60 and 0.47 eV, respectively). When operated at room temperature, they exhibited peak quantum efficiencies from 55 to 95% in the wavelength range of 1.0 to 2.5 μm and 0.0025 to 2.3 mA/cm^2 dark current density. Li *et al.* [53] demonstrated two GSMBE grown mesa-type ex-InGaAs photodiodes with different InGaAs compositions, $In_{0.9}Ga_{0.1}As$ and $In_{0.78}Ga_{0.22}As$ have the cutoff wavelengths of 2.9 and 2.4 μm, respectively. The dark current densities are 2.8 and 0.34 mA/cm^2 at - 0.1 V and at 290 K, respectively.

Lattice mismatch between ex-InGaAs layers and InP substrates is large, at +1.85% ~ +2.2% for λ_c > 2.5 µm. Hence ex-InGaAs photodiodes contain significantly more growth defects compared to their lattice-matched counterpart. A study on commercial ex-InGaAs photodiode FPAs established a link between the growth defects (misfit dislocations) and *1/f* noise [54]. It is therefore unsurprising that, ex-InGaAs photodiodes were found to be more susceptible to radiation damage, compared to Si and InGaAs detectors, in a space trial [57]. This is a major disadvantage for remote gas sensing applications, which are highly likely to be employed in space environments if applied to greenhouse gases monitoring.

1.1.4. InGaAs/GaAsSb Type-II superlattice

Most existing high-performance SWIR photodiodes require significant cooling in order to suppress the photodiode's dark current, which contributes to noise. In type-II superlattice (T2SL) structures which are formed by materials with staggered band offsets, the thermal carrier generation is lower than that in the case of a direct band gap transition, hence there has been interest in developing photodiodes based on T2SL for both SWIR and MWIR bands.

When the thickness of each superlattice (SL) layer is sufficiently thin, minibands are formed in the materials. Electrons and holes in the adjacent wells interact, resulting in a continuous energy state across different wells in the superlattice.

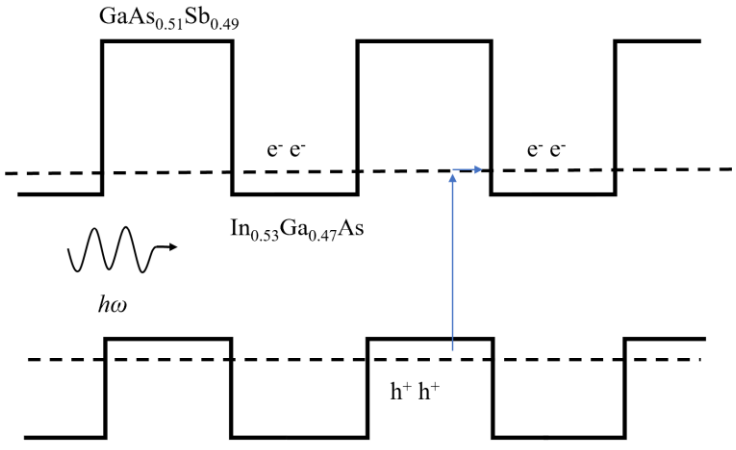

Figure 1.4: The bandgap diagram for InGaAs/GaAsSb type-II superlattice layers, with optical absorption taking place between states.

For SWIR band, the typical T2SL structures consist of alternate layers of InGaAs and GaAsSb, whose band diagram is shown in Figure 1.4. Electrons and holes are largely confined within the InGaAs wells and GaAsSb barriers, respectively. There is however sufficient wavefunction overlap, enabling optical absorption to take place without the presence of phonon. Compared to the bandgap of either InGaAs or GaAsSb bulk materials, the type-II optical absorption offers a narrower effective bandgap and hence a longer cutoff wavelength [2]. In terms of dark currents, the relatively large bandgaps of InGaAs and GaAsSb (compared to MCT with and InAs) are expected to cause less thermally generated dark currents.

Figure 1.5 compares dark current density of $In_{0.53}Ga_{0.47}As/GaAs_{0.51}Sb_{0.49}$ T2SL photodiodes at different temperatures from the literature, focusing on those with cutoff wavelengths of 2 to 3 µm [58]–[62]. Some of these are SAM APD structures ([58] and [60]) and the dark current density values for these were taken from their punch-through voltages.

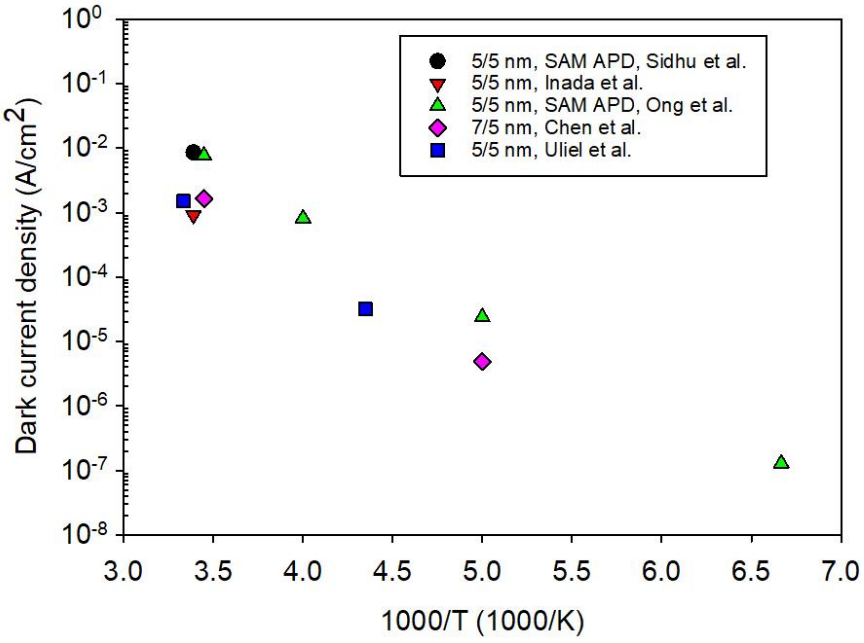

Figure 1.5: Comparison of dark current densities at different temperature of T2SL InGaAs/GaAsSb photodiodes.

10 K photoluminescence spectra in the range of 2.3 – 2.8 µm were obtained from $In_{0.53}Ga_{0.47}As/GaAs_{0.51}Sb_{0.49}$ T2SL lattice-matched to InP substrates include [63], well beyond the emission wavelengths expected from either $In_{0.53}Ga_{0.47}As$ or $GaAs_{0.51}Sb_{0.49}$. Later, Brown *et al.* [64] confirmed that photoluminescence and photoresponse from these InGaAs/GaAsSb T2SL structures originated from type-II transition.

This was followed by the first demonstration of $In_{0.53}Ga_{0.47}As/GaAs_{0.51}Sb_{0.49}$ mesa photodiode on InP substrate in 2005 [65]. Using a 5 nm/ 5 nm T2SL design, it exhibited a cutoff wavelength of 2.39 µm, dark current density of 5.09 mA/cm^2 at -1 V, and peak room-temperature EQE of 43% at 2.23 µm. As with wafers in earlier SWIR T2SL works, the wafer used was grown by MBE. Inada *et al.* [59] reported Low dark current density of 0.92 mA/cm^2 at -1 V, more than one order of magnitude lower than that of conventional HgCdTe photodiode. T2SL using MBE-grown planar *p-i-n* photodiodes with 250 pair InGaAs (5 nm) /GaAsSb (5 nm). EQE at ~2.2 µm was slightly lower at 34% (responsivity ~ 0.6 A/W) at room temperature.

In 2011, Inada *et al.* [66] reported the successful operation of planar type *p-i-n* photodiodes and FPA using T2SL wafers grown by MOVPE. For photodiode with 250 pairs InGaAs/GaAsSb QWs, dark current density was 9.0 µA/cm^2 at -1 V at 233 K and responsivity was 0.5 A/W at 2 µm (slightly lower than their earlier work [62]). By increasing the T2SL repeats to 450 pairs, the responsivity was increased to 0.8 A/W at 2 µm. Further data from these MOVPE-grown T2SL photodiodes [67] included. Under 2 µm wavelength illumination and -1 V, the maximum EQE was obtained as ~ 30% with 250 T2SL pairs and ~ 48% with 450 T2SL pairs.

Since photodiodes made with narrow bandgap materials exhibit relatively high band-to-band tunnelling currents at the high electric fields, Separate Absorption Multiplication avalanche photodiodes (SAM-APDs) structures can be used. In a SAM-APD, the design aims for a low electric field in the narrow bandgap absorption region to minimise the tunnelling current while a high electric field in the multiplication region. The electric field difference is achieved using a moderately-doped charge sheet (or field-control layer). Sidhu *et al.* [58] first reported that InP-based SAM-APD with InP multiplication region and T2SL absorption region of 150 pairs of T2SL $In_{0.53}Ga_{0.47}As/GaAs_{0.51}Sb_{0.49}$ quantum wells has responsivity > 2 µm. This device exhibited λ_c of 2.4 µm, EQE of 38% at 2.2 µm, gain > 30 and dark current density near breakdown of less than 0.66 mA/cm^2 at room temperature. Ong *et al.* [60] reported the similar SAM-APD with InAlAs multiplication region (instead of InP), which its characteristics include 2.5 µm cutoff wavelength, EQE of 32% at 2.0 µm, gain > 50 and dark current density near breakdown of 30 mA/cm^2 at room temperature.

1.1.5. AlInAsSb

Compared to HgCdTe, the quaternary material system AlInAsSb is attractive because it uses conventional, established wafer growth method as well as the absence of mercury and cadmium in the material. Being a bulk material means that its optical absorption coefficients are likely to be higher than those of T2SL. In addition, wide bandgap barrier layers (which are often needed to block diffusion currents) could be obtained using the same material system (by increasing the Al fraction).

AlInAsSb of different compositions can be grown lattice matched to GaSb, InP [68] or InAs [69] substrates. By choosing suitable AlInAsSb compositions, high performance AlInAsSb photodiodes have the potential to cover a wide wavelength range within SWIR band. Using room temperature PL spectra, bandgap of $Al_xIn_{1-x}As_ySb_{1-y}$ digital alloy for x = 0 to 0.75 lattice-matched to GaSb substrates is given by [70]

$$E_g(x) = 0.247 + 0.97x + 0.47x^2 \text{ eV}. \quad (1.1)$$

For SWIR photodiodes, the composition range is from x = 0.1 to 0.4 with corresponding bandgap of 0.35 to 0.73 eV (λ_c: 3.5 to 1.7 μm). The low excess noise and low dark current density of $Al_{0.79}In_{0.21}As_{0.74}Sb_{0.26}$-based APDs on InP substrates at high gain were demonstrated by Kodati *et al.* [68]. However, due to the large bandgap, high performance AlInAsSb APDs grown on InP substrates are only suitable for short wavelength infrared spectrum. In 1991, Charykov *et al.* determined the bandgap for LPE-grown $Al_xIn_{1-x}As_ySb_{1-y}$ layers lattice matched to InAs substrates, for x = 0 (λ_c of 3.0 μm) to x = 0.08 (λ_c of 2.5 μm) [69]. Nonetheless, InAs lacks large commercially available substrates.

The vast majority of researches on AlInAsSb photodiodes or APDs focused on materials grown on GaSb substrates. In 2016, the low-noise 1-step AlInAsSb staircase APD grown on n-type GaSb substrate with near-ideal gain of 1.8 ± 0.2 per step over a broad range of wavelengths shorter than ~ 950 nm was demonstrated by taking advantage of the large ratio of the conduction-band discontinuity to the threshold energy between $Al_{0.7}In_{0.3}As_{0.31}Sb_{0.69}$ and $InAs_{0.91}Sb_{0.09}$ [71]. The results suggest AlInAsSb staircase APDs can be a promising platform on which to build enhanced night vision, thermal imaging, and free-space telecommunications capabilities [71].

Later, APDs were demonstrated using different MBE-grown $Al_xIn_{1-x}As_ySb_{1-y}$ wafers with different Al fractions on GaSb (001) substrate [72], [73]. The $Al_xIn_{1-x}As_ySb_{1-y}$ layers were

grown as a digital alloy of the binary alloys of AlAs, AlSb, InAs, and InSb, using a digital alloy period of 3 nm and the following shutter sequence: AlSb, AlAs, AlSb, InSb, InAs, and Sb. This was adopted to overcome the wide miscibility gap present in the $Al_xIn_{1-x}As_ySb_{1-y}$ material system [70], [74]. Bank *et al.* [75] demonstrated the further work that $Al_xIn_{1-x}As_ySb_{1-y}$/GaSb APDs with decreasing x from 0.7 to 0.3 exhibit that the cutoff wavelengths increase from 1 to > 1.6 μm with decreasing bandgaps and low excess noise corresponding to k = 0.01 ~ 0.05 with peak quantum efficiencies of $\geq$ 50%.

Jones *et al.* [76] demonstrated low-noise, 2 μm SAM-APDs with narrow bandgap $Al_{0.3}In_{0.7}AsSb$ (~ 0.58 eV) absorption region and wide bandgap $Al_{0.7}In_{0.3}AsSb$ (~ 1.16 eV) multiplication layers to achieve very low excess noise ($k \approx 0.01$), gain > 100 at room temperature, and EQEs of ~ 20% at unity gain without antireflection coating under 2 μm illumination. J_{dark} is 0.186 mA/cm^2 at gain =10 when operating between 200 - 220 K. This performance is comparable to HgCdTe at nearly 100 K higher operating temperature.

The low-noise characteristics, substrate availability of GaSb and bandgap tunability of the $Al_xInAsSb$ materials system make it a promising candidate for highly sensitive detectors across SWIR spectrum.

1.2. Motivations and thesis overview

The main advantages and disadvantages of the existing and emerging semiconductor materials for SWIR photodiodes covered in the literature review above are summarised in Table 1.1. In this work, experimental studies of InGaAs/GaAsSb Type-II superlattice photodiodes and AlInAsSb photodiodes were carried out to assess their potentials to meet the needs of 2 - 3 μm wavelength light detection without the use of cryogenic cooling.

Table 1.1. Comparison of SWIR photodiode materials

Materials	Main Advantages	Main disadvantages
HgCdTe	• High detectivities • Low dark current • High gain	• Cryogenic operating temperatures • Restricted use due to Hg and Cd • Highly specialised manufacturing technologies • Expensive
Ex-InGaAs	• High operating temperatures • Low dark current	• Lattice mismatched to the InP substrates • Susceptible to radiation damage
InAs	• High gain at low noise and high operation temperature • Low dark current	• High surface leakage currents • Unnecessarily long cutoff wavelength for SWIR applications • Cryogenic operating temperatures
T2SL	• Low dark current • Large capability to tailor the bandgap with different materials, layers' thicknesses and compositions. • Reduced Auger recombination	• Low and temperature-dependent quantum efficiency
AlInAsSb	• High gain at low noise and high operation temperature • Low dark current	• The onset of band-to-band tunneling at low electric fields • Cryogenic operating temperatures

The rest of the thesis is organised as follows.

Chapter 2 provides background theory on quantum efficiency, responsivity, response speed, noise, impact ionisation process, avalanche multiplication, and photodetector technologies.

Chapter 3 describes the experimental techniques used for characterising type-II InGaAs/GaAsSb type-II superlattice and AlInAsSb *p-i-n* photodiodes. These include temperature dependent current-voltage, capacitance-voltage, and avalanche gain setups.

Chapter 4 reports the details of the InGaAs/GaAsSb type-II superlattice *p-i-n* mesa and planar photodiodes. Temperature dependent electrical and optical characterisation results are presented and analysed.

Chapter 5 presents temperature dependent electrical characterisation results and analysis of AlInAsSb photodiodes for 3 μm detection. Photomultiplication results from temperature dependent photomultiplication measurements and the normalisation procedure used to determine multiplication factors are also reported.

Chapter 6 summarises and draws the conclusions from the work. In addition, suggestions for future work are included.

1.3. Reference

[1] M. Franceschi, M. Martinelli, L. Gislimberti, A. Rizzi, and M. Massironi, 'Integration of 3D modeling, aerial LiDAR and photogrammetry to study a synsedimentary structure in the Early Jurassic Calcari Grigi (Southern Alps, Italy)', *Eur. J. Remote Sens.*, vol. 48, no. 1, pp. 527–539, Jan. 2015, doi: 10.5721/EuJRS20154830.

[2] J. C. Campbell, 'Recent Advances in Avalanche Photodiodes', *J. Light. Technol.*, vol. 34, no. 2, pp. 278–285, Jan. 2016, doi: 10.1109/JLT.2015.2453092.

[3] M. H. M. Reddy, J. T. Olesberg, C. Cao, and J. P. Prineas, 'MBE-grown high-efficiency GaInAsSb mid-infrared detectors operating under back illumination', *Semicond. Sci. Technol.*, vol. 21, no. 3, pp. 267–272, Mar. 2006, doi: 10.1088/0268-1242/21/3/009.

[4] G. P. Agrawal, *Fiber-optic Communication Systems (Wiley series in microwave and optical engineering)*. John Wiley & Sons Incorporated.

[5] H. Melchior, A. R. Hartman, D. P. Schinke, and T. E. Seidel, 'Atlanta Fiber System Experiment: Planar Epitaxial Silicon Avalanche Photodiode', *Bell Syst. Tech. J.*, vol. 57, no. 6, pp. 1791–1807, Jul. 1978, doi: 10.1002/j.1538-7305.1978.tb02127.x.

[6] E. Repasi, P. Lutzmann, O. Steinvall, M. Elmqvist, B. Göhler, and G. Anstett, 'Advanced short-wavelength infrared range-gated imaging for ground applications in monostatic and bistatic configurations', *Appl. Opt.*, vol. 48, no. 31, p. 5956, Nov. 2009, doi: 10.1364/AO.48.005956.

[7] X. Liu, S. Cheng, H. Liu, S. Hu, D. Zhang, and H. Ning, 'A Survey on Gas Sensing Technology', *Sensors*, vol. 12, no. 7, pp. 9635–9665, Jul. 2012, doi: 10.3390/s120709635.

[8] Winston Chow, Richard Dawson, Bruce Glavovic, Marjolijn Haasnoot, Mark Pelling, and William Solecki, 'IPCC Sixth Assessment Report (AR6): Climate Change 2022 - Impacts, Adaptation and Vulnerability: Factsheet Human Settlements', Feb. 28, 2022. https://policycommons.net/artifacts/2264360/ipcc_ar6_wgii_factsheet_humansettlements/

[9] N. Menyuk and D. K. Killinger, 'Atmospheric remote sensing of water vapor, HCI and CH_4 using a continuously tunable Co:MgF2 laser', p. 5.

[10] T. F. Refaat *et al.*, 'Backscatter 2-μm Lidar Validation for Atmospheric CO_2 Differential Absorption Lidar Applications', *IEEE Trans. Geosci. Remote Sens.*, vol. 49, no. 1, pp. 572–580, Jan. 2011, doi: 10.1109/TGRS.2010.2055874.

[11] E. V. Browell, S. Ismail, and S. T. Shipley, 'Ultraviolet DIAL measurements of O_3 profiles in regions of spatially inhomogeneous aerosols', *Appl. Opt.*, vol. 24, no. 17, p. 2827, Sep. 1985, doi: 10.1364/AO.24.002827.

[12] G. Ehret, C. Kiemle, M. Wirth, A. Amediek, A. Fix, and S. Houweling, 'Space-borne remote sensing of CO_2, CH_4, and N_2O by integrated path differential absorption lidar: a sensitivity analysis', *Appl. Phys. B*, vol. 90, no. 3–4, pp. 593–608, Mar. 2008, doi: 10.1007/s00340-007-2892-3.

[13] S. Kuang, J. F. Burris, M. J. Newchurch, S. Johnson, and S. Long, 'Differential Absorption Lidar to Measure Subhourly Variation of Tropospheric Ozone Profiles', *IEEE Trans. Geosci. Remote Sens.*, vol. 49, no. 1, pp. 557–571, Jan. 2011, doi: 10.1109/TGRS.2010.2054834.

[14] N. Sugimoto and A. Minato, 'Long-path absorption measurement of CO_2 with a Raman-shifted tunable dye laser', *Appl. Opt.*, vol. 32, no. 33, p. 6827, Nov. 1993, doi: 10.1364/AO.32.006827.

[15] A. Minato, MD. M. A. Joarder, S. Ozawa, M. Kadoya, and N. Sugimoto, 'Development of a Lidar System for Measuring Methane Using a Gas Correlation Method', *Jpn. J. Appl. Phys.*, vol. 38, no. Part 1, No. 10, pp. 6130–6132, Oct. 1999, doi: 10.1143/JJAP.38.6130.

[16] A. I. Carswell, 'Lidar measurements of the atmosphere', *Can. J. Phys.*, vol. 61, no. 2, pp. 378–395, Feb. 1983, doi: 10.1139/p83-049.

[17] J. T. Olesberg, 'Noninvasive blood glucose monitoring in the 2.0-2.5 μm wavelength range', in *LEOS 2001. 14th Annual Meeting of the IEEE Lasers and Electro-Optics Society (Cat. No.01CH37242)*, San Diego, CA, USA, 2001, vol. 2, p. 529. doi: 10.1109/LEOS.2001.968909.

[18] S. D. Gunapala, D. R. Rhiger, and C. Jagadish, Eds., *Advances in infrared photodetectors*, 1st ed. Amsterdam ; Boston: Academic Press, 2011.

[19] W. Lei, R. J. Gu, J. Antoszewski, J. Dell, and L. Faraone, 'GaSb: A New Alternative Substrate for Epitaxial Growth of HgCdTe', *J. Electron. Mater.*, vol. 43, no. 8, pp. 2788–2794, Aug. 2014, doi: 10.1007/s11664-014-3049-x.

[20] W. D. Lawson, S. Nielsen, E. H. Putley, and A. S. Young, 'Preparation and properties of HgTe and mixed crystals of HgTe-CdTe', *J. Phys. Chem. Solids*, vol. 9, no. 3–4, pp. 325–329, Mar. 1959, doi: 10.1016/0022-3697(59)90110-6.
[21] A. Rogalski, 'HgCdTe infrared detectors - Historical prospect', *Proc SPIE*, vol. 4999, pp. 431–442, Jul. 2003, doi: 10.1117/12.479679.
[22] J. M. Arias, M. Zandian, R. Zucca, and R. E. DeWames, '*p - i - n* HgCdTe photodiodes grown by molecular beam epitaxy', *Appl. Phys. Lett.*, vol. 58, no. 24, pp. 2806–2808, Jun. 1991, doi: 10.1063/1.104742.
[23] A. Rogalski, K. Adamiec, and J. Rutkowski, *Narrow-gap semiconductor photodiodes*. Bellingham, Wash.: Bellingham, Wash. : SPIE Press, c2000, 2000.
[24] I. M. Baker *et al.*, 'Linear-mode avalanche photodiode arrays in HgCdTe at Leonardo, UK: the current status', in *Image Sensing Technologies: Materials, Devices, Systems, and Applications VI*, Baltimore, United States, May 2019, p. 20. doi: 10.1117/12.2519830.
[25] O. Gravrand *et al.*, 'HgCdTe Detectors for Space and Science Imaging: General Issues and Latest Achievements', *J. Electron. Mater.*, vol. 45, no. 9, pp. 4532–4541, Sep. 2016, doi: 10.1007/s11664-016-4516-3.
[26] J. Beck *et al.*, 'The HgCdTe electron avalanche photodiode', *J. Electron. Mater.*, vol. 35, no. 6, pp. 1166–1173, 2006.
[27] D. Z. Ting *et al.*, 'Antimonide type-II superlattice barrier infrared detectors', presented at the SPIE Defense + Security, Anaheim, California, United States, Feb. 2017, p. 101770N. doi: 10.1117/12.2266263.
[28] L. W. Lim, C. H. Tan, J. S. Ng, J. D. Petticrew, and A. B. Krysa, 'Improved Planar InAs Avalanche Photodiodes With Reduced Dark Current and Increased Responsivity', *J. Light. Technol.*, vol. 37, no. 10, pp. 2375–2379, May 2019, doi: 10.1109/JLT.2019.2905535.
[29] X. Zhou, X. Meng, A. B. Krysa, J. R. Willmott, J. S. Ng, and C. H. Tan, 'InAs Photodiodes for 3.43 µm Radiation Thermometry', *IEEE Sens. J.*, vol. 15, no. 10, pp. 5555–5560, Oct. 2015, doi: 10.1109/JSEN.2015.2443563.
[30] R. B. Gomes, C. H. Tan, P. J. Ker, J. P. R. David, and J. S. Ng, 'InAs avalanche photodiodes for X-ray detection', *J. Instrum.*, vol. 6, no. 12, pp. P12005–P12005, Dec. 2011, doi: 10.1088/1748-0221/6/12/P12005.
[31] A. Krier and X. L. Huang, 'Design considerations for uncooled InAs mid-infrared light emitting diodes grown by liquid phase epitaxy', *J. Phys. Appl. Phys.*, vol. 39, no. 2, pp. 255–261, Jan. 2006, doi: 10.1088/0022-3727/39/2/004.
[32] Ş. Kalem, 'Molecular-beam epitaxial growth and transport properties of InAs epilayers', *J. Appl. Phys.*, vol. 66, no. 7, pp. 3097–3103, Oct. 1989, doi: 10.1063/1.344141.
[33] S. K. Haywood, R. W. Martin, N. J. Mason, and P. J. Walker, 'Growth of InAs by MOVPE: A comparative study using arsine, tertiarybutylarsine and phenylarsine', *J. Cryst. Growth*, vol. 97, no. 2, pp. 489–496, Sep. 1989, doi: 10.1016/0022-0248(89)90231-5.
[34] G. Lucovsky, 'Electrical characteristics of diffused InAs p-n junctions', *Br. J. Appl. Phys.*, vol. 12, no. 6, pp. 311–312, Jun. 1961, doi: 10.1088/0508-3443/12/6/111.
[35] Ray-Ming Lin *et al.*, 'Room temperature unpassivated InAs p-i-n photodetectors grown by molecular beam epitaxy', *IEEE Trans. Electron Devices*, vol. 44, no. 2, pp. 209–213, Feb. 1997, doi: 10.1109/16.557708.
[36] R.-M. Lin, S.-F. Tang, S.-C. Lee, and C. H. Kuan, 'Improvement of current leakage in the InAs photodetector by molecular beam epitaxy', *J. Cryst. Growth*, vol. 227–228, pp. 167–171, Jul. 2001, doi: 10.1016/S0022-0248(01)00657-1.
[37] M. Mikhailova, N. Smirnova, and S. Slobodchikov, 'Carrier multiplication in InAs and InGaAs p-n junctions and their ionization coefficients', *Sov. Phys.-Semicond.*, vol. 10, no. 5, pp. 509–513, 1976.
[38] A. R. J. Marshall, P. Vines, P. J. Ker, J. P. R. David, and C. H. Tan, 'Avalanche Multiplication and Excess Noise in InAs Electron Avalanche Photodiodes at 77 K', *IEEE J. Quantum Electron.*, vol. 47, no. 6, pp. 858–864, Jun. 2011, doi: 10.1109/JQE.2011.2128299.
[39] A. R. J. Marshall, C. H. Tan, M. J. Steer, and J. P. R. David, 'Electron dominated impact ionization and avalanche gain characteristics in InAs photodiodes', *Appl. Phys. Lett.*, vol. 93, no. 11, p. 111107, Sep. 2008, doi: 10.1063/1.2980451.

[40] A. R. J. Marshall, Chee Hing Tan, M. J. Steer, and J. P. R. David, 'Extremely Low Excess Noise in InAs Electron Avalanche Photodiodes', *IEEE Photonics Technol. Lett.*, vol. 21, no. 13, pp. 866–868, Jul. 2009, doi: 10.1109/LPT.2009.2019625.
[41] P. J. Ker, J. P. R. David, and C. H. Tan, 'Temperature dependence of gain and excess noise in InAs electron avalanche photodiodes', *Opt. Express*, vol. 20, no. 28, p. 29568, Dec. 2012, doi: 10.1364/OE.20.029568.
[42] A. R. J. Marshall, P. J. Ker, A. Krysa, J. P. R. David, and C. H. Tan, 'High speed InAs electron avalanche photodiodes overcome the conventional gain-bandwidth product limit', *Opt. Express*, vol. 19, no. 23, p. 23341, Nov. 2011, doi: 10.1364/OE.19.023341.
[43] B. S. White, I. C. Sandall, J. P. R. David, and Chee Hing Tan, 'InAs Diodes Fabricated Using Be Ion Implantation', *IEEE Trans. Electron Devices*, vol. 62, no. 9, pp. 2928–2932, Sep. 2015, doi: 10.1109/TED.2015.2456434.
[44] B. S. White *et al.*, 'High-Gain InAs Planar Avalanche Photodiodes', *J. Light. Technol.*, vol. 34, no. 11, pp. 2639–2644, Jun. 2016, doi: 10.1109/JLT.2016.2531278.
[45] J. C. Dries, M. R. Gokhale, K. J. Thomson, S. R. Forrest, and R. Hull, 'Strain compensated $In_{1-x}Ga_xAs(x<0.47)$ quantum well photodiodes for extended wavelength operation', *Appl. Phys. Lett.*, vol. 73, no. 16, pp. 2263–2265, Oct. 1998, doi: 10.1063/1.121696.
[46] W. E. Tennant, D. Lee, M. Zandian, E. Piquette, and M. Carmody, 'MBE HgCdTe Technology: A Very General Solution to IR Detection, Described by "Rule 07", a Very Convenient Heuristic', *J. Electron. Mater.*, vol. 37, no. 9, pp. 1406–1410, Sep. 2008, doi: 10.1007/s11664-008-0426-3.
[47] W. E. Tennant, '"Rule 07" Revisited: Still a Good Heuristic Predictor of p/n HgCdTe Photodiode Performance?', *J. Electron. Mater.*, vol. 39, no. 7, pp. 1030–1035, Jul. 2010, doi: 10.1007/s11664-010-1084-9.
[48] 'InGaAs PIN photodiodes- G12182 series'. HAMAMATSU. Accessed: Jun. 10, 2022. [Online]. Available: https://www.hamamatsu.com/content/dam/hamamatsu-photonics/sites/documents/99_SALES_LIBRARY/ssd/g12182_series_kird1118e.pdf
[49] 'InGaAs PIN photodiodes- G12183 series'. HAMAMATSU. Accessed: Jun. 10, 2022. [Online]. Available: https://www.hamamatsu.com/content/dam/hamamatsu-photonics/sites/documents/99_SALES_LIBRARY/ssd/g12183_series_kird1119e.pdf
[50] 'InGaAs photodiode - FD05D'. Accessed: Jun. 12, 2022. [Online]. Available: https://www.thorlabs.com/drawings/e9ce1ea564cbd16c-773224F4-E0E7-AE18-CBE0C38F41528CC5/FD05D-SpecSheet.pdf
[51] 'J22 and J23 SERIES InGaAs PHOTODIODES'. Accessed: Jun. 17, 2022. [Online]. Available: teledynejudson.com/prods/Documents/PB4206.pdf
[52] G. H. Olsen, M. J. Lange, M. J. Cohen, D.-S. Kim, and S. R. Forrest, 'Three-band 1.0-2.5 um near-infrared InGaAs detector array', presented at the SPIE's International Symposium on Optical Engineering and Photonics in Aerospace Sensing, Orlando, FL, Jul. 1994, pp. 151–159. doi: 10.1117/12.179693.
[53] X. Li *et al.*, 'Extended wavelength InGaAs SWIR FPAs with high performance', in *Infrared Sensors, Devices, and Applications VII*, San Diego, United States, Sep. 2017, p. 14. doi: 10.1117/12.2273550.
[54] Y. Ma *et al.*, '320×256 Extended Wavelength $In_x Ga_{1-x} As$/InP Focal Plane Arrays: Dislocation Defect, Dark Signal and Noise', *IEEE J. Sel. Top. Quantum Electron.*, vol. 28, no. 2, pp. 1–11, Mar. 2022, doi: 10.1109/JSTQE.2021.3087182.
[55] A. J. Moseley, M. D. Scott, A. H. Moore, and R. H. Wallis, 'High-efficiency, low-leakage MOCVD-grown GaInAs/AlInAs heterojunction photodiodes for detection to 2.4μm', *Electron. Lett.*, vol. 22, no. 22, pp. 1206-1207(1), Oct. 1986.
[56] R. U. Martinelli, T. J. Zamerowski, and P. A. Longeway, '2.6 μm InGaAs photodiodes', *Appl. Phys. Lett.*, vol. 53, no. 11, pp. 989–991, Sep. 1988, doi: 10.1063/1.100050.
[57] Q. L. Kleipool *et al.*, 'In-flight proton-induced radiation damage to SCIAMACHY's extended-wavelength InGaAs near-infrared detectors', *Infrared Phys. Technol.*, vol. 50, no. 1, pp. 30–37, Mar. 2007, doi: 10.1016/j.infrared.2006.08.001.
[58] R. Sidhu, L. Zhang, N. Tan, N. Duan, J. C. Campbell, and A. L. Holmes, '2.4 μm cutoff wavelength avalanche photodiode on InP substrate', *Electron. Lett.*, vol. 42, no. 3, pp. 181–182, 2006.

[59] H. Inada *et al.*, 'Low dark current SWIR photodiode with InGaAs/GaAsSb Type II quantum wells grown on InP substrate', in *2009 IEEE International Conference on Indium Phosphide & Related Materials*, Newport Beach, CA, USA, May 2009, pp. 149–152. doi: 10.1109/ICIPRM.2009.5012464.
[60] D. S. G. Ong, J. S. Ng, Y. L. Goh, C. H. Tan, S. Zhang, and J. P. R. David, 'InAlAs Avalanche Photodiode With Type-II Superlattice Absorber for Detection Beyond 2 $\mu\hbox{m}$', *IEEE Trans. Electron Devices*, vol. 58, no. 2, pp. 486–489, Feb. 2011, doi: 10.1109/TED.2010.2090352.
[61] B. Chen, W. Jiang, J. Yuan, A. L. Holmes, and Bora. M. Onat, 'SWIR/MWIR InP-Based p-i-n Photodiodes With InGaAs/GaAsSb Type-II Quantum Wells', *IEEE J. Quantum Electron.*, vol. 47, no. 9, pp. 1244–1250, Sep. 2011, doi: 10.1109/JQE.2011.2160450.
[62] Y. Uliel *et al.*, 'InGaAs/GaAsSb Type-II superlattice based photodiodes for short wave infrared detection', *Infrared Phys. Technol.*, vol. 84, pp. 63–71, Aug. 2017, doi: 10.1016/j.infrared.2017.02.003.
[63] J. F. Klem, S. R. Kurtz, and A. Datye, 'Growth and properties of GaAsSb/InGaAs superlattices on InP', *J. Cryst. Growth*, vol. 111, no. 1–4, pp. 628–632, May 1991, doi: 10.1016/0022-0248(91)91053-D.
[64] G. J. Brown, J. E. Van Nostrand, S. M. Hedge, W. J. Siskaninetz, and Q. Xie, 'Type-II InGaAs/GaAsSb superlattice for photodetection in the near infrared', presented at the Symposium on Integrated Optoelectronic Devices, San Jose, CA, May 2002, p. 179. doi: 10.1117/12.467662.
[65] R. Sidhu, Ning Duan, J. C. Campbell, and A. L. Holmes, 'A long-wavelength photodiode on InP using lattice-matched GaInAs-GaAsSb type-II quantum wells', *IEEE Photonics Technol. Lett.*, vol. 17, no. 12, pp. 2715–2717, Dec. 2005, doi: 10.1109/LPT.2005.859163.
[66] H. Inada *et al.*, 'MOVPE grown InGaAs/GaAsSb type II quantum well photodiode for SWIR focal plane array', presented at the SPIE Defense, Security, and Sensing, Orlando, Florida, United States, May 2011, p. 801220. doi: 10.1117/12.888096.
[67] K. Fujii, T. Ishizuka, Y. Nagai, Y. Iguchi, and K. Akita, 'MOVPE growth for photodiodes in 2.5 μm region with InGaAs/GaAsSb type-II quantum wells', *Phys. Status Solidi C*, vol. 10, no. 5, pp. 732–735, May 2013, doi: 10.1002/pssc.201200611.
[68] S. H. Kodati *et al.*, 'AlInAsSb avalanche photodiodes on InP substrates', *Appl. Phys. Lett.*, vol. 118, no. 9, p. 091101, Mar. 2021, doi: 10.1063/5.0039399.
[69] N. A. Charykov, A. M. Litvak, K. D. Moiseev, and Y. P. Yakovlev, 'New semiconductor material A1xInAsySb/InAs: LPE synthesis and properties', presented at the ECO4 (The Hague '91), The Hague, Netherlands, Sep. 1991, pp. 198–203. doi: 10.1117/12.47163.
[70] S. J. Maddox, S. D. March, and S. R. Bank, 'Broadly Tunable AlInAsSb Digital Alloys Grown on GaSb', *Cryst. Growth Des.*, vol. 16, no. 7, pp. 3582–3586, Jul. 2016, doi: 10.1021/acs.cgd.5b01515.
[71] M. Ren, S. Maddox, Y. Chen, M. Woodson, J. C. Campbell, and S. Bank, 'AlInAsSb/GaSb staircase avalanche photodiode', *Appl. Phys. Lett.*, vol. 108, no. 8, p. 081101, Feb. 2016, doi: 10.1063/1.4942370.
[72] M. E. Woodson, M. Ren, S. J. Maddox, Y. Chen, S. R. Bank, and J. C. Campbell, 'Low-noise AlInAsSb avalanche photodiode', *Appl. Phys. Lett.*, vol. 108, no. 8, p. 081102, Feb. 2016, doi: 10.1063/1.4942372.
[73] M. Ren, S. J. Maddox, M. E. Woodson, Y. Chen, S. R. Bank, and J. C. Campbell, 'AlInAsSb separate absorption, charge, and multiplication avalanche photodiodes', *Appl. Phys. Lett.*, vol. 108, no. 19, p. 191108, May 2016, doi: 10.1063/1.4949335.
[74] Leslie G. Vaughn *et al.*, 'Type I mid-infrared MQW lasers using AlInAsSb barriers and InAsSb wells', presented at the Proc.SPIE, Apr. 2005, vol. 5722. doi: 10.1117/12.606226.
[75] S. R. Bank *et al.*, 'Avalanche Photodiodes Based on the AlInAsSb Materials System', *IEEE J. Sel. Top. Quantum Electron.*, vol. 24, no. 2, pp. 1–7, Mar. 2018, doi: 10.1109/JSTQE.2017.2737880.
[76] A. H. Jones, S. D. March, S. R. Bank, and J. C. Campbell, 'Low-noise high-temperature AlInAsSb/GaSb avalanche photodiodes for 2-μm applications', *Nat. Photonics*, vol. 14, no. 9, pp. 559–563, Sep. 2020, doi: 10.1038/s41566-020-0637-6.

2. Background

Both photodiodes and APDs could detect and amplify weak incoming optical signal. Materials used in photodiodes for photon absorption can be utilised for APDs, to ensure good quantum efficiency in the operation wavelength range. Photodiodes can be operated by applying no reverse bias, though providing a small reverse bias can reduce the capacitance and increase quantum efficiency. In contrast, to obtain high internal gain from APDs, it is essential to apply reverse bias. Although the value of reverse bias is entirely dependent on the APD used, APDs are always operated at much higher reverse bias voltage than photodiodes.

Key performance parameters for photodiodes, such as quantum efficiency, responsivity, response speed, and device noise, are introduced here. Additional performance parameters that are applicable to avalanche photodiodes. These are followed by background theory of different detector technologies (distinct from semiconductor materials).

2.1. Quantum Efficiency and Responsivity

When a semiconductor material absorbs a photon, the energy of the photon is used to promote a bound electron in the valence band to become a free electron in the conduction band, leaving behind a free hole in the valence band. Movements of these free carriers result in current, or more specifically photocurrent.

Efficient collection of these carriers helps to maximise the photocurrent, which is the signal in an optical detection system. This can be achieved using a *p-i-n* diode structure under reverse bias, as illustrated in Figure 2.1. The electron-hole pairs are produced by light absorption in the *p-i-n* diode. Eventually, these pairs created in the depletion region, W_D, or within their diffusion lengths (*p* or *n* regions) will be separated by the electric field, resulting in the current flow. Carriers created by photon absorption outside the depletion region may still be collected, since they may diffuse towards the depletion junction. However, some of them will be lost through carrier recombination, especially for those created far from the depletion junction edges.

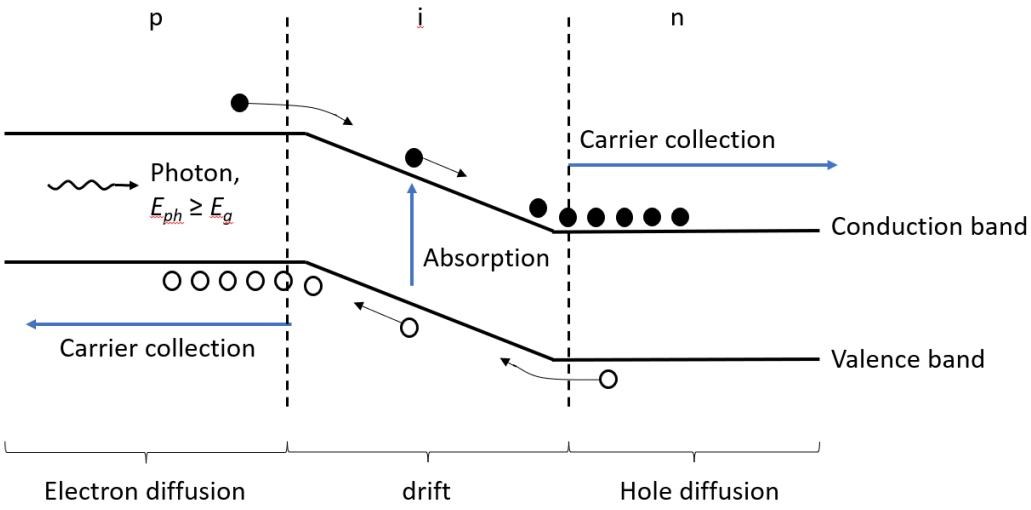

Figure 2.1: The energy band diagram of p-i-n diode under reverse-bias and illumination conditions.

Photon absorption can only take place if the photon's energy, E_{ph}, is equal to or greater than the semiconductor material's bandgap. The photon's energy is related to the photon's wavelength, λ, according to

$$E_{ph} = \frac{hc}{\lambda}, \tag{2.1}$$

where h is the Planck's constant (6.626×10^{-34} J·s), and c is the speed of light (3×10^{8} ms^{-1}). Similarly, bandgap of a given semiconductor material determines its cut-off wavelength (λ_c) through $\lambda_c = \frac{hc}{E_g}$ (in µm).

For light with $\lambda < \lambda_c$, the material's optical absorption coefficient, α_{abs}, determines how strongly the light is absorbed by the material. The intensity of light remaining in the material after traversing the material for a distance x, $I(x)$, is given by

$$I(x) = I_{(x=0)}\exp(-\alpha_{abs}x), \tag{2.2}$$

where $I_{(x=0)}$ is the initial intensity of the light. In addition to being material dependent. α_{abs} also depends on wavelength, temperature, and doping density. For $\lambda > \lambda_c$, the value of absorption coefficient is too small to give appreciable absorption.

A photodiode's quantum efficiency (η) is defined as the number of the electron-hole pairs generated per incident photon [1]. It is expressed as

$$\eta = \frac{I_{ph}}{q} \times \left(\frac{P_{opt}\lambda}{hc}\right)^{-1}, \quad (2.3)$$

where I_{ph} is the photocurrent generated from the absorbed incident optical power P_{opt}, and electron charge q is 1.6×10^{-19} C. Maximising the signal I_{ph} therefore maximises η. Good photodiode designs usually aim to have most of the incoming light absorbed within the depletion region hence W_D should be ~ 1/ α_{abs}.

For a given photodiode operated at identical conditions, its quantum efficiency varies with wavelength due to wavelength dependence of optical absorption coefficient. The unity quantum efficiency (the ideal case) is achieved by absorption of all photons and collection of all the photogenerated carriers. In practical photodiodes, $\eta < 1$ so external quantum efficiency (η_{ext}) is used to account for losses, which could range from reflection loss at the air/semiconductor surface just outside the photodiode to loss of photogenerated carriers through carrier recombination within the photodiode.

Responsivity (R) is another commonly used performance parameter used to describe a photodiode's ability to detect the incoming light. Responsivity is defined as the ratio of the photocurrent to the incident optical power. Responsivity is closely related to quantum efficiency and their relationship is given as

$$R = \frac{I_{ph}}{P_{opt}} = \frac{\eta q}{h\nu} = \frac{\eta\lambda\,(\mu m)}{1.24}. \quad [\text{A/W}] \quad (2.4)$$

For ideal photodiodes ($\eta = 1$), $R = \frac{\lambda}{1.24}$ A/W, where λ is in μm. For high quantum efficiency, high responsivity and $\alpha_{abs}W_D \gg 1$, are desired. However, the transit-time delay may be considerable when $W_D \gg 1/\alpha_{abs.}$

In many applications, having high quantum efficiency or responsivity at wavelengths outside the operation wavelength is detrimental to the optical detection system. The background light produces currents that are in fact considered as noise. For example, free-space communication systems prefer the photodiodes to have spectral full-width-half-maximum as narrow as possible to minimise current due to background light. This often necessitates addition of appropriate optical filters in front of the photodiodes.

2.2. Detector noise

There are several factors contributing to noise of an optical detection system incorporating a photodiode. Hence it is useful to consider the overall effect using the system's signal-noise ratio (SNR), defined as the ratio of the desired signal power to the total noise power.

The signal power is given by $I_{ph}^2 = (R\,P_{in})^2$. The noise power is the sum of the photodiode's shot noise and the post-detection amplifier circuit's noise power. The former is given by $2qB\,(I_{ph} + I_B + I_D)$, where I_D is the photodiode's dark current, I_B is the current resulting from background radiation, such as black-body radiation from the detector housing. The amplifier's noise power is given by $\langle {i_{amplier}}^2 \rangle = \frac{4kTB}{R_{eq}}$, where R_{eq} is the equivalent resistance of the amplifier. Hence, SNR for an optical detection system using a photodiode is expressed as [2]

$$SNR = \frac{\text{signal power}}{shot\ noise\ power + amplifier\ noise} = \frac{\frac{1}{2}\times(\frac{q\eta P_{opt}}{h\nu})^2}{2q(I_{ph}+I_B+I_D)B+4kTB/R_{eq}}. \quad (2.5)$$

A higher optical signal power could increase signal current and hence the shot noise, but this is usually not a dominant noise mechanism in SWIR band applications.

2.3. Response speed

Photodiodes must respond sufficiently quickly to changes in magnitude of incoming optical signals for the optical detection systems employing them. For optical fibre communication systems, high transmission data rate (e.g. > 40 Gb/s) is required. However, SWIR band applications have much lower requirements in terms of response speed. Response speed of a photodiode is limited by the following factors: (i) carriers' transit time through the depletion region (τ_r), (ii) carriers' diffusion time to the depletion region edges, and (iii) capacitance of the depletion region.

The carriers' transit time through the depletion region is given by $\tau_r = \frac{W_D}{\upsilon_s}$, where υ_s is carrier saturation velocity. The upper limit of -3dB bandwidth imposed by carriers' transit time is given by ($\omega\tau_r = 2.4$) [1]

$$f_{-3dB} = \frac{2.4}{2\pi\tau_r} \approx \frac{0.4\upsilon_s}{W_D}. \quad (2.6)$$

There is therefore a trade-off between quantum efficiency and response speed. For faster response speed, the depletion region must be thin to reduce the transit time. For higher quantum efficiency, the depletion region must be thick enough to absorb more incident light.

Carriers generated outside the depletion region must diffuse to the junction before being collected, resulting in reduced quantum efficiency (section 2.1) and time delay. To minimise the length that photogenerated carriers need to diffuse and the time taken, the depletion region's edge should be very close to the surface.

The final factor limiting the -3dB bandwidth arises from interaction between the detection circuit's load resistance (R_L) and the photodiode's junction capacitance (C_j). They form a low-pass filter circuit with a time constant of R_LC and introduce another bandwidth limit given by $f_{-3dB} = \frac{1}{2\pi RC}$. Since the photodiode's junction capacitance is inversely proportional to W_D (details in Chapter 3), having very narrow depletion region will cause excessive capacitance and hence a large R_LC time constant.

2.4. Impact Ionisation and avalanche multiplication

APDs are sometimes used instead of photodiodes, to benefit from the internal gains provided by the former. The mechanism responsible these internal gains is a process called impact ionisation.

When a large reverse electric field is applied to a semiconductor diode, carriers travelling along the field can acquire energy. When some of these energetic carriers could collide with the lattice atoms and produce new free electrons and holes. These are termed impact ionisation events. They can either be electron-initiated or hole-initiated, as illustrated in Figure 2.2. In the electron-initiated process, the initiating electron descents to a lower energy state (compared to the original condition) on the conduction band by losing some/all its energy to promote another electron from the top of the valence band of the atom into the bottom of the conduction band. The 'new' electron leaves behind a hole in the valence band.

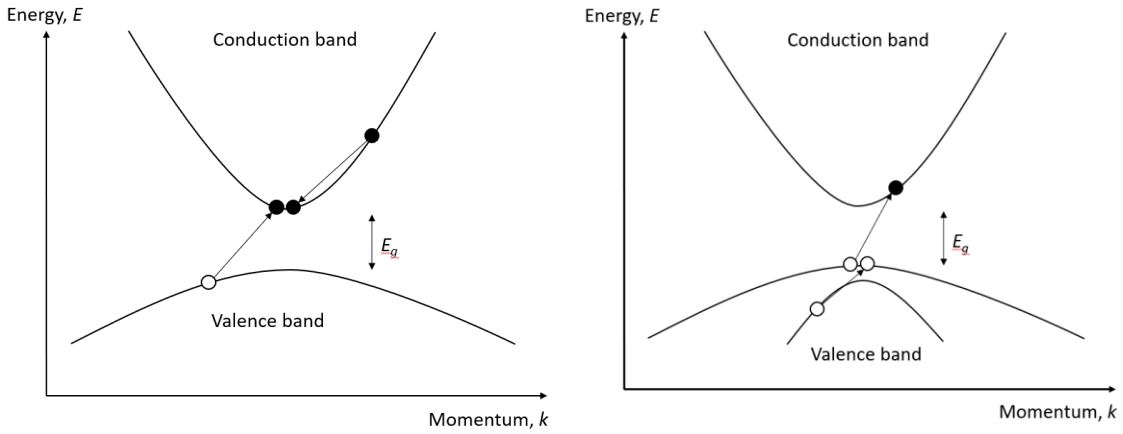

(a) (b)

Figure 2.2: E-k diagrams of (a) electron-initiated and (b) hole-initiated impact ionisation events.

Impact ionisation coefficients for electrons and holes, α and β, respectively are used to to describe how easily impact ionisation events will occur for a given set of conditions. The reciprocal of α (β) is the mean path length of an electron (a hole) between consecutive impact ionisation events. Generally, values of α and β are unequal and they are strongly dependent on electrical field, temperature, and material. α and β reported for various semiconductor materials at a given temperature are often expressed as

$$\alpha(E_{field}) = A_e \exp(-\frac{B_e}{E_{field}})^C$$

and

$$\beta(E_{field}) = A_h \exp(-\frac{B_h}{E_{field}})^C, \quad (2.7)$$

where E_{field} is electric field strength. A, B and C are the constants of the material.

There is a minimum distance that the carriers must travel before gaining enough energy to initiate impact ionisation. This is termed carrier's dead space. It is closely related to impact ionisation threshold energy, E_{th}, which is the minimum ionisation energy needed for impact ionisation and must be larger than the bandgap. There are often different values of E_{th} for electrons and holes for a given material and temperature.

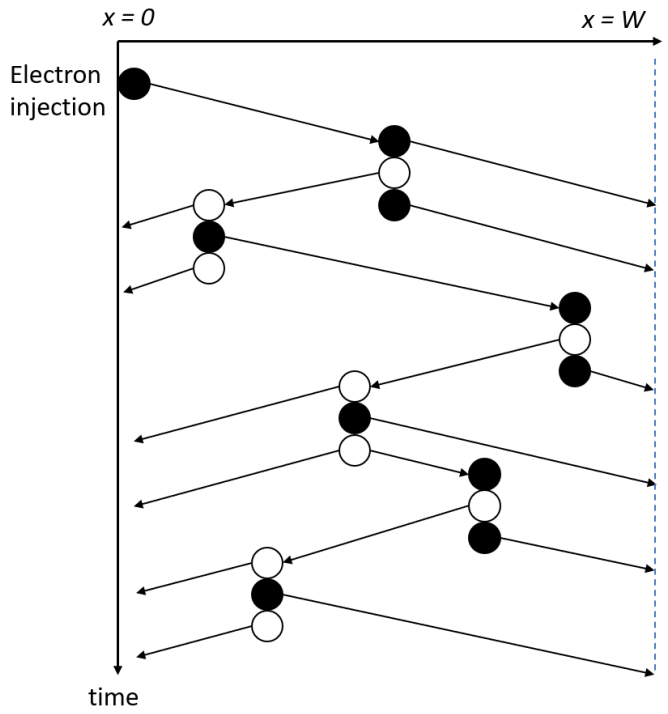

Figure 2.3: Avalanche multiplication process in the high-field depletion region with width w for pure electron injection at x = 0.

When consecutive impact ionisation events occur, the device will produce an appreciable avalanche multiplication (*M*), which is defined as the ratio of the total number of carriers exiting the high electric field to the number of carriers injected into the electric field. Magnitude of the avalanche multiplication is determined by the carrier-injection conditions and avalanche width, in addition to the ionisation coefficients for the electric field and the threshold energies.

Consider a *p*-*i*-*n* diode (with $x = 0$ and $x = w$ the positions of the *p*/*i* and *i*/*n* junctions, respectively) illustrated in Figure 2.3. If carrier dead space is insignificant compared to the avalanche region width, the avalanche multiplication resulted from an electron-hole pair being injected at position *x*, is given by

$$M(x) = \frac{exp\left(-\int_0^x (\alpha(x') - \beta(x'))dx'\right)}{1 - \int_0^w a(x')\, exp\left(-\int_0^{x'} (a(x'') - \beta(x''))dx''\right)dx'} . \qquad (2.8)$$

For an ideal *p*-*i*-*n* diode, in which the electric field across the depletion region (*i*-layer) is constant, the ionisation coefficients are independent of position. Hence, Equation (2.6) is simplified into

$$M(x) = \frac{(\alpha - \beta) exp\,(-(\alpha - \beta)x)}{a\, exp(-(\alpha - \beta)w) - \beta} . \qquad (2.9)$$

When $\alpha > \beta$, M decreases with x so the maximum M occurs when $x = 0$. When $\alpha < \beta$, M increases with x so the maximum M could be achieved when $x = w$. Regardless of the relationship between α and β, the APD produces pure electron multiplication factor (M_e) or pure hole multiplication factor (M_h), when only electrons or holes are injected into the avalanche region, respectively. Assuming insignificant carrier dead space, these can be calculated as:

$$M_e = \frac{\alpha-\beta}{a\ exp(-(\alpha-\beta)w)-\beta} \tag{2.10}$$

and

$$M_h = \frac{(\alpha-\beta)exp\ (-(\alpha-\beta)w)}{a\ exp(-(\alpha-\beta)w)-\beta}. \tag{2.11}$$

The combination of M_e and M_h provides a simple way to obtain the ionsation coefficients which is given by

$$\alpha = \frac{1}{w}\left(\frac{M_e-1}{M_e-M_h}\right) ln\ (\frac{M_e}{M_h}) \tag{2.12}$$

and

$$\beta = \frac{1}{w}\left(\frac{M_h-1}{M_h-M_e}\right) ln\ (\frac{M_h}{M_e}) \tag{2.13}$$

2.5. Photodetector technologies

Photodiodes and avalanche photodiodes (APDs) make use of photovoltaic effect to detect incoming photons. There are other photodetector technologies relying on other mechanism for photon detections, such as photoelectric effect.

2.5.1. Avalanche photodiodes

Most APDs utilise materials with favourable impact ionisation characteristics as their multiplication regions. usually uses single wide-bandgap semiconductor or series of heterojunctions. Photogenerated carriers can be multiplied through the impact ionisation process when energy gained from accelerating through the electric field is higher than threshold energy of impact ionisation. The avalanche breakdown voltage associated with the multiplication layer. Because of amplification, the current would increase from few nano-amps to micro-amps, the breakdown voltage is typically measured at reverse current

of 10 μA. For APDs, the criteria with respect to quantum efficiency and response speed are similar to those for non-avalanching photodiodes. Additionally, there is a trade-off between avalanche gain and noise, as high gain is always accompanied by high noise.

Avalanche breakdown was firstly reported by McKay and McAfee in 1953 [3]. They demonstrated multiplications in both silicon and germanium P-N junction rod using a narrow light beam appeared to be avalanche formation. Initially APDs were developed to satisfy the demand of optical receivers for high speed long haul optical fibre communication. In 1960s, the first type of APDs was developed by Johnson [4].

2.5.1.1. Mesa and planar device topologies

When producing devices from semiconductor wafers, the devices may have one of two main types of device topologies. These are mesa and planar topologies, whose cross-sectional views are shown schematically in Figures 2.4 (a) and (b) respectively. In both cases, incoming light might be admitted through the substrate or the top layer.

The mesa devices are formed by etching away material surrounding the devices to leaving mesa-shaped devices. Front illumination through the etched opening in the top contact [5] or rear illumination through etched hole substrate [6] with different mesa geometries can been achieved. Passivation materials covered sidewalls of mesas can remove surface accumulation charges and suppress surface leakage currents.

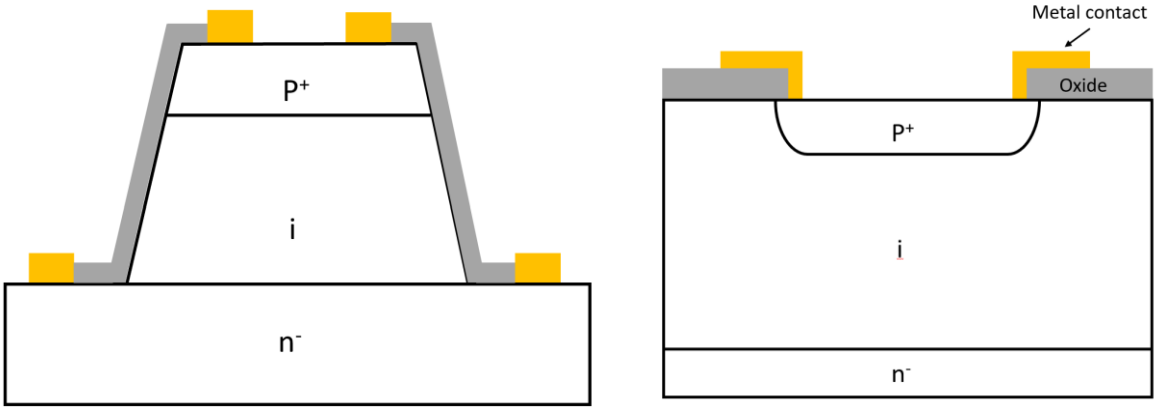

(a) ***(b)***

Figure 2.4: The front-illuminated p-i-n photodiode with (a) mesa geometry and (b) planar geometry.

Figure 2.4 (b) depicts a planar p-i-n photodiode. Through the ion implantation or diffusion into undoped material, regions of the material can become highly p-doped, creating diodes. For commercial InGaAs photodiodes or InGaAs-based APDs, Zn-diffusion is an established method to create p-doped material in otherwise undoped InP layers. Note that some degree of lateral dopant diffusion exists so the actual sizes of planar devices are slightly larger than the 'window' of Zn-diffusion (details in Chapter 4).

2.5.1.2. Superlattice bandgap structures

When two semiconductor materials form a heterostructure, their band line-up falls into one of four types depending on the values for the band discontinuities. These are type-I, type-II "staggered", and type-II "misaligned" as shown in Figure 2.5 [7]. Type-I occurs for systems with $\Delta E_c + \Delta E_v = E_{g2} - E_{g1}$. The type-I band line-up is used extensively to confine carriers in lasers' quantum wells and light-emitting diodes' heterojunctions to maximise efficiency of light emission.

Type-II bandgap structures can be divided into "staggered" and "misaligned". Type-II "staggered" structure is found in certain superlattices of ternary and quaternary III-Vs, where $\Delta E_c - \Delta E_v = E_{g2} - E_{g1}$. Examples include $InAs_xSb_{1-x}$/InSb and $In_{1-x}Ga_xAs$/ $GaSb_{1-y}As_y$ systems. The bottom of the conduction bands and the top of the valence bands are situated in opposing layers of SLs, allowing for the spatial separation of confined electrons and holes. Photon absorption is possible, giving rise to T2SL photodiodes.

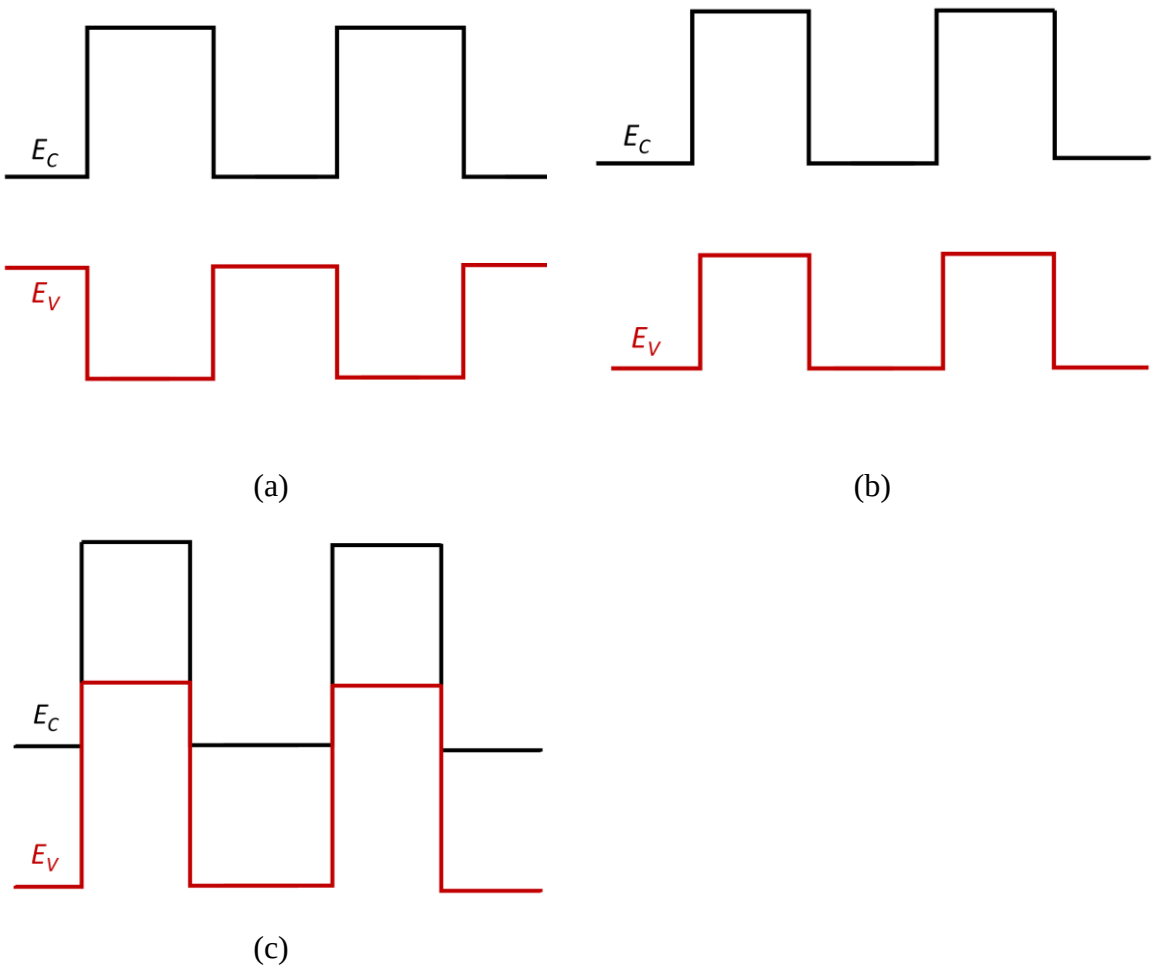

Figure 2.5: Various types of semiconductor SL structures: (a) type-I structure, (b) type-II "staggered" structure, and (c) type-II "misaligned" structure.

2.5.2. Photomultiplier tubes (PMT)

Photoelectric effect describes the process in which electrons are emitted from the surface of the metal/ semiconductor in the vacuum when the photons strike this metal/ semiconductor. PMTs exploit this for photon detection and secondary electron emission for internal gain, as illustrated in Figure 2.6. The PMT is a vacuum glass tube with a photocathode, a series of dynodes and an anode. When phonons arrive on the photocathode of PMT, photoelectrons would be produced and emitted from the photocathode. By applying a large electric field between the cathode and the anode, the electrons could be accelerated to the first dynode (Dynode 1). Electrons would be multiplied and emitted to the second dynode (Dynode 2) when the electrons strike the dynodes (secondary electron emission). This continues for subsequent dynode stages.

By using a large number of dynodes (up to 19), PMTs can provide very high gain (up to 10^8) with low excess noise. However they have significant disadvantages in terms of their dimensions (large compared to semiconductor devices) and requirement of high voltage supply (500 V to 3 kV) [8]. PMTs have very poor quantum efficiency for SWIR band detection (e.g. 1 % at 1000-1200 nm and no products at wavelengths > 1700 nm of PMT with InP/InGaAs (Cs) photocathode [9]). Hence, they are not suitable at all for SWIR applications.

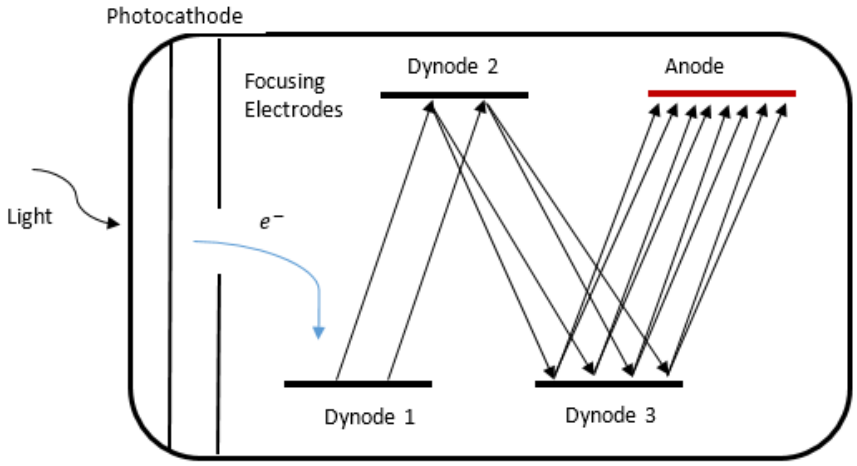

Figure 2.6: Basic structure of photomultiplier tube. Reduced dynode stages are shown for clarity.

2.6. Reference

[1] Simon M. Sze and Kwok K. Ng, *Physics of Semiconductor Devices, 3rd. Edition*. John Wilay and Sons Inc.

[2] 'Light Absorption by Water Molecules and Inorganic Substances Dissolved in Sea Water', in *Light Absorption in Sea Water*, New York, NY: Springer New York, 2006, pp. 11–81. doi: 10.1007/978-0-387-49560-6_2.

[3] K. G. McKay and K. B. McAfee, 'Electron Multiplication in Silicon and Germanium', *Phys Rev*, vol. 91, no. 5, pp. 1079–1084, Sep. 1953, doi: 10.1103/PhysRev.91.1079.

[4] K. M. Johnson, 'High-speed photodiode signal enhancement at avalanche breakdown voltage', *IEEE Trans. Electron Devices*, vol. 12, no. 2, pp. 55–63, Feb. 1965, doi: 10.1109/T-ED.1965.15453.

[5] R. F. Leheny, R. E. Nahory, and M. A. Pollack, '$In_{0.53}Ga_{0.47}As$ *p-i-n* photodiodes for long-wavelength fibre-optic systems', *Electron. Lett.*, vol. 15, no. 22, pp. 713-715(2), Oct. 1979.

[6] T. P. Pearsall and M. Papuchon, 'The Ga0.47In0.53As homojunction photodiode—A new avalanche photodetector in the near infrared between 1.0 and 1.6 μm', *Appl. Phys. Lett.*, vol. 33, no. 7, pp. 640–642, Oct. 1978, doi: 10.1063/1.90447.

[7] A. Rogalski, *Infrared detectors*, 2nd ed. Boca Raton: Taylor & Francis, 2011.

[8] J. S. Ng, 'Impact ionisation measurement and modelling of long wavelength avalanche photodiodes', University of Sheffield, 2003.

[9] 'PMT Handbook'. HAMAMATSU. Accessed: Jun. 24, 2022. [Online]. Available: https://www.hamamatsu.com/content/dam/hamamatsu-photonics/sites/documents/99_SALES_LIBRARY/etd/PMT_handbook_v3aE.pdf

3. Experimental techniques

The characterisation techniques employed to evaluate the performance of InGaAs/GaAsSb T2SL superlattice *p-i-n* photodiodes and AlInAsSb photodiodes include temperature dependent current-voltage (I-V), capacitance-voltage (C-V), photoresponse and photomultiplication measurements. Details of these techniques, typical experimental conditions and methods of analyses are presented below.

3.1. Current-Voltage Measurement

I-V measurement is the most elementary and fundamental measurement carried out to characterise the fabricated photodiodes. Forward/reverse I-V characteristics could give a wealth of information regarding the diode's properties including ideality factor, series resistance, dominant bulk current mechanism and breakdown voltage.

In an I-V measurement setup, a picoammeter or a source-measurement unit (SMU) simultaneously applies a forward/reverse bias voltage across the two terminals of the diode-under-test (DUT) and measures the resultant current flowing through the DUT. For a given DUT, the I-V measurement is first carried out in the dark to produce the dark I-V characteristics. Later measurements may include illumination on the DUT to produce photocurrent characteristics. In this work, several experimental setups were used to obtained I-V characteristics. The equipment was either a HP 4140B picoammeter, a Keithley 236 SMU or a Keithley 237 SMU. In each measurement, each data point was obtained by averaging over ~ 100nA.

3.1.1. Forward Current-Voltage Measurement

In the forward bias, the ideal I-V characteristics can be expressed by Shockley's diode equation [1]

$$I_f(V) = I_0 \exp\left(\frac{qV}{nkT} - 1\right), \tag{3.1}$$

with

$$I_0 = qA{n_i}^2\left(\frac{D_p}{L_p N_D} + \frac{D_n}{L_n N_A}\right), \tag{3.2}$$

where I_0 is saturation current, q is the electron charge, k is Boltzmann's constant, T is the temperature (in Kelvin), and n is the ideality factor. In Eqn. 3.2, D, L refers to the diffusion constant and minority carrier diffusion length, respectively; their subscripts p, n refer to the hole and electron minority carriers; N_D and N_A represent the donor concentration in the n-type material and the acceptor concentration in the p-type material, respectively. n_i is dependent on the bandgap of the material and temperature.

Value of n close to 1 or 2 indicates that the dominant leakage current mechanism is the diffusion current (I_{diff}) (Eqn. 3.3) or the generation-recombination current ($I_{g\text{-}r}$) (Eqn. 3.4), respectively. For a given DUT, the value of n can vary the forward voltage. For example, at high forward voltages, large forward current may fill up traps in the diodes such as the I-V characteristic becomes dominated by diffusion current.

$$I_{diff} = I_0[exp\left(\frac{qV}{k_BT}\right) - 1] \tag{3.3}$$

$$I_{g-r} = I_0[exp\left(\frac{qV}{2k_BT}\right) - 1] \tag{3.4}$$

Since I_{diff} and $I_{g\text{-}r}$ originate from the semiconductor junction of the DUT, they scale with the junction area, A, so are often categorized as bulk leakage mechanisms. If the different-sized devices have leakage currents that are dominated by either or both mechanisms, then their current density, $J = I/A$, would be in agreement. An example is shown in Figure 3.1.

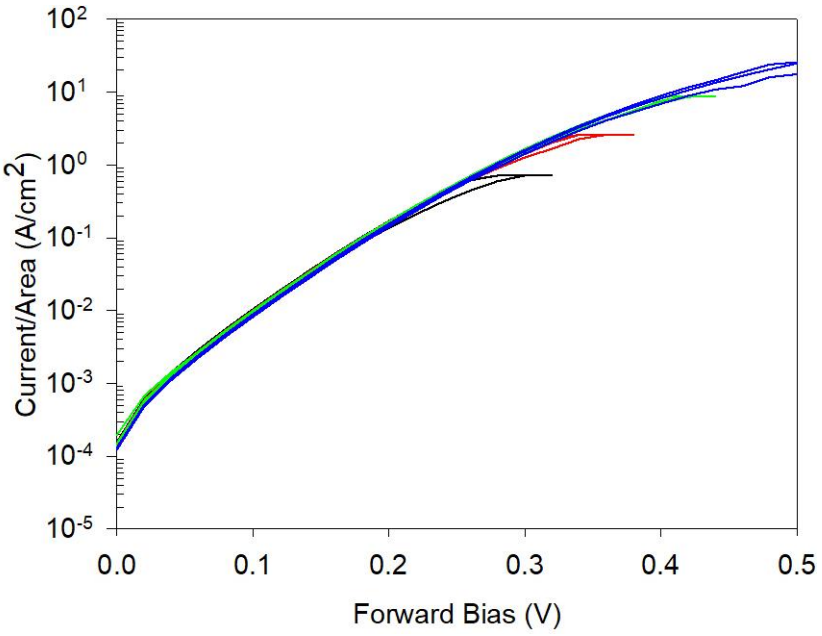

Figure 3.1: Room temperature forward J-V characteristics of GaAsSb p-i-n diodes.

In practical devices, there is often with the presence of series resistance due to resistance in the cladding layer and /or the metal contact, R_s, the forward diode current becomes

$$I_f(V) = I_0 exp\,(\frac{q(V-I_s R_s)}{nkT} - 1). \qquad (3.5)$$

The series resistance cannot be eliminated, however an undesirable large series resistance will dramatically diminish the voltage drop across the limit the DUT's frequency response due to low-pass filtering from a series R-C combination. These forward dark current density versus voltage characteristics shown in Figure 3.2 are fitted with Eqn. (3.5) using n = 1.28 and R_s = 50 Ω, indicating that the current densities are dominated by diffusion current mechanism. The contact resistance can be reduced by proper selection of metals as the p- and n-type contacts, and with an accurate scheme of the annealing temperature. Also, the doping concentrations of the semiconductor that the metals are deposited on can also be increased to reduce the contact resistance.

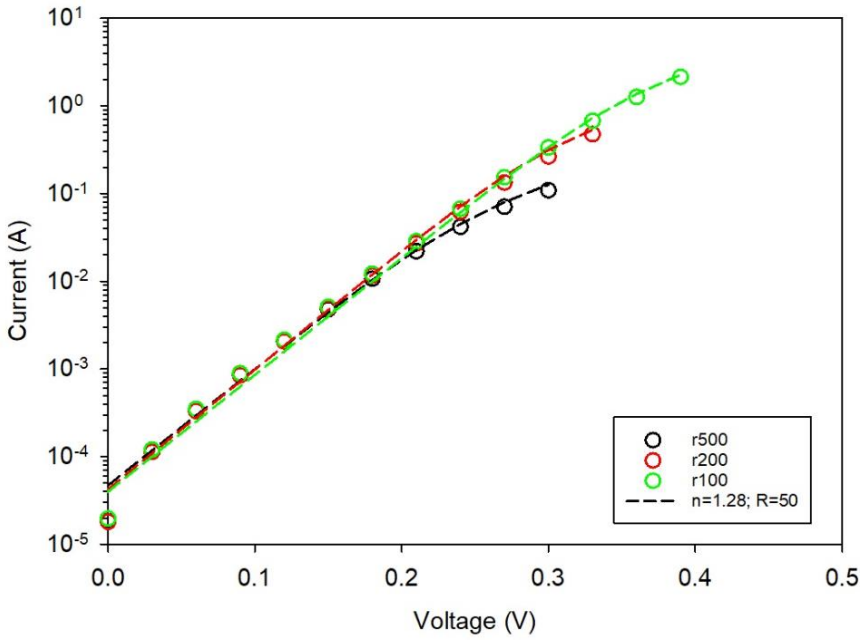

Figure 3.2: Measured and fitted room temperature forward I-V characteristics of InGaAs p-i-n diodes.

For research-grade devices used in this work, if there is noticeable series resistance, the exact value of series resistance often varies with the device size. Therefore, J-V characteristics of different-sized devices may even not be in agreement, as shown in Figure 3.3.

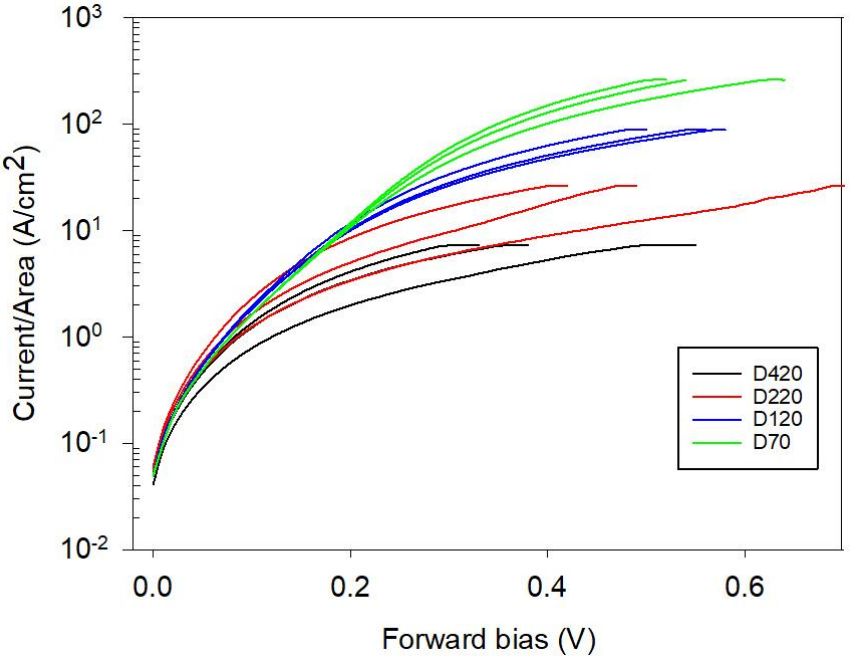

Figure 3.3: Room temperature forward J-V characteristics of AlInAsSb p-i-n diodes.

3.1.2. Reverse I-V characteristics

In the reverse bias, the aforementioned diffusion current and generation-recombination current still exist. Therefore Eqn. 3.3 and 3.4 still apply. However, the dependence of diffusion current on the reverse bias is weak.

In addition to the two bulk leakage mechanisms, there exists another bulk leakage mechanism, band-to-band tunnelling current (I_{tun}). Tunnelling current is the result of quantum mechanical tunnelling through potential barrier. This is illustrated in Figure 3.4(a) and (b), which depict a p-n diode with bandgap of E_g under 0 V bias and a large reverse electric field, respectively. In Figure 3.4(a), bound electrons in the valance band on the p-side faces a thick potential barrier so the probability of quantum tunnelling is small. When a large reverse field causes the energy band within the depletion region to bend significantly, as shown in Figure 3.4(b), the energy band within the depletion region to bend significantly. This reduces the barrier thickness for the bound electrons considerably and increases the probability of quantum tunnelling, resulting in a higher tunnelling current. Although band-to-band tunnelling is described above, it is also possible to have tunnelling current via traps or defect levels in the forbidden energy gap.

Since tunnelling current originates from the diode's depletion region, it is another bulk leakage current mechanism and hence scale with the diode's area. Potential barrier thickness strongly influence tunnelling current, hence diodes made with narrow band gap materials exhibit higher tunnelling currents than those made with wide band gap materials, for a given reverse electric field. This is however not always compatible with the need for narrow bandgap materials to produce SWIR band photodiodes.

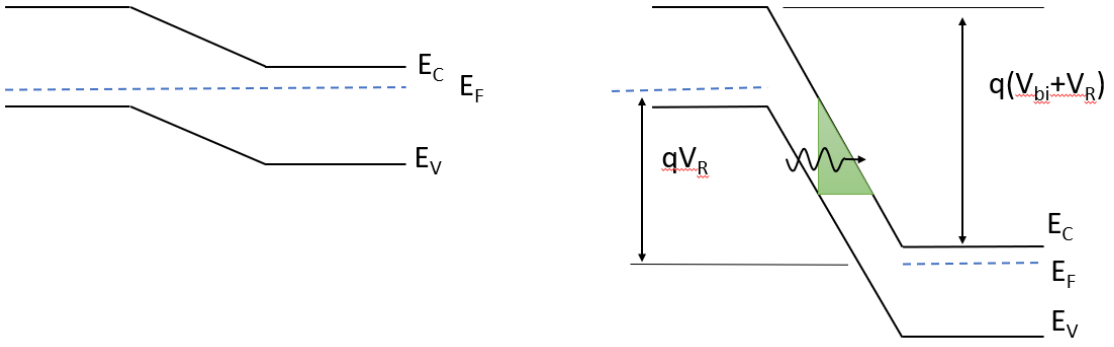

(a) (b)

Figure 3.4: Energy band diagrams under (a) thermal-equilibrium condition and (b) Reverse-bias condition.

The equation can be expressed as follows [1].

$$I_{tun}(V) = \frac{(2m_e)^{\frac{1}{2}} q^3 \xi V A}{4\pi^2 \hbar^2 E_g^{\frac{1}{2}}} exp\left(-\frac{\sigma_{tun} m_e^{\frac{1}{2}} E_g^{\frac{3}{2}}}{q\hbar\xi}\right), \qquad (3.6)$$

where V is the reverse bias across the device, m_e is the carrier effective mass, ξ is the electric field (given by $(V + V_{bi})/\, w$, for p-i-n diodes),τ_{eff} is the effective carrier lifetime, E_g is the direct bandgap and σ_{tun} is tunnelling parameter depending on the shape of the tunnelling barrier (from 1.11 to 1.88). Figure 3.5 represents the sample of tunnelling current fitting of AlInAsSb photodiodes with σ_{tun} = 1.75, which shows narrow tunnelling barrier. In Eqn. 3.6, tunnelling current does not have a direct temperature dependence but it does have a weak temperature dependence through the temperature dependence of bandgap. Hence, effective suppression of tunnelling current is usually achieved by having using materials with wide bandgaps and/or reducing the reverse electric field, instead of device cooling (which is effective for diffusion and generation-recombination currents).

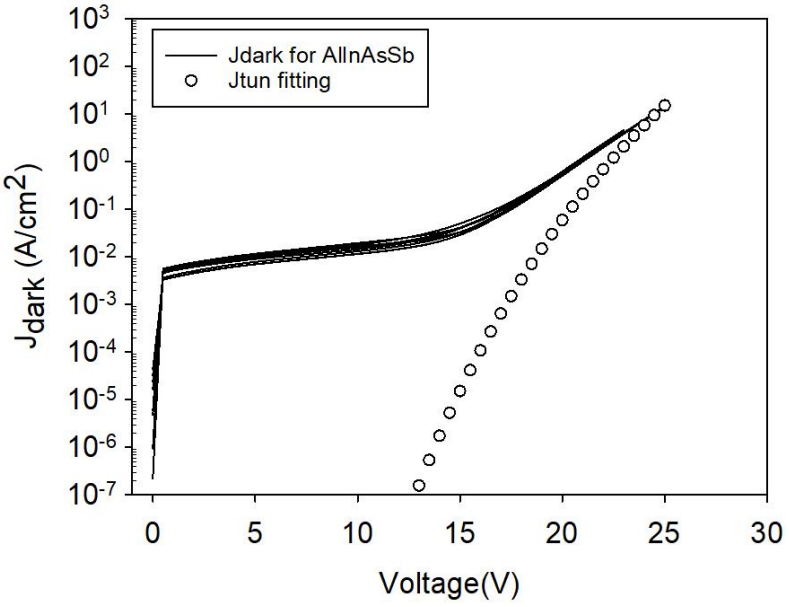

Figure 3.5: The sample of tunnelling current fitting for AlInAsSb photodiodes by using σ_{tun} = 1.75.

I-V characteristics of photodiodes often exhibit generation-recombination current and the diffusion current at low reverse bias. Depending on the device's material bandgap and applied electric field, the dark current at high reverse bias may be dominated by tunnelling current and/or avalanche gain.

3.1.3. Surface leakage currents

In addition to bulk leakage current mechanisms, there could be surface leakage current due to the presence of conducting paths in the mesa periphery. Mesa diodes are created by chemical etching which removes semiconductor materials between the neighbouring diodes. The process of material removal may have created damages on the mesa sidewalls. The surface leakage current is not desirable and should be minimised via appropriate etching and passivation procedures.

Total leakage current of the DUT is the sum of bulk leakage currents and surface leakage currents. Dark currents due to bulk and surface leakage mechanisms have different dependences on the device's radius, as described by

$$I_{dark} = I_{bulk} + I_{surf}. \tag{3.7}$$

So,
$$I_{dark} = \pi r^2 J_{bulk} + 2\pi r J_{surf}, \tag{3.8}$$

where J_{bulk} and J_{surf} are bulk dark current density (in unit of A/m^2) and surface dark current density (in unit of A/m). By comparing current density and I/A versus reverse bias characteristics extracted from experimental I-V characteristics of different-sized devices, it is possible to determine whether the dark current is dominated by bulk or surface leakage mechanism(s).

3.2. Capacitance-Voltage Measurement

The characteristics of capacitance as a function of applied voltage may disclose information regarding the background doping concentration, intrinsic region thickness, and built-in voltage of the p-i-n diode. Secondary Ion Mass Spectroscopy (SIMS) measurement is another alternative method of estimating the doping profiles and i region thicknesses.

C-V measurements are carried out using an HP4275A multifrequency LCR meter and a probe station. The LCR meter applies a DC reverse bias superimposed with a small sinusoidal test signal to the DUT, which can be represented by resistances (a series resistance R_{series} and a shunt resistor R_{shunt}) and capacitance (junction capacitor C_j) as shown in Figure 3.6. R_{shunt} represents the leakage current paths (both bulk and surface currents). The series resistance R_{series} represent the resistance between the devices and the contact metals. The LCR meter measures the DUT's impedance and phase angle to deduce the DUT's resistance and the capacitance. The deduction assumes a user-selected equivalent circuit mode, namely a series R_{series}-C_j or a parallel R_{shunt}-C_j connection. The capacitance measurement is repeated for a user-defined range of reverse bias using a LabVIEW program.

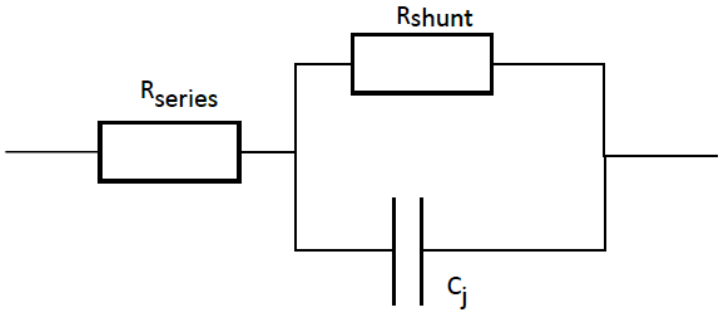

Figure 3.6. Equivalent circuit of a photodiode

Before each measurement session the LCR meter is calibrated (using auto-zero function) to prevent the setup's parasitic capacitance affecting the readings. In this work, the sinusoidal test signal has a frequency of 1MHz, as suggested by the LCR meter manual. The capacitance extraction assumes that the DUT is represented by a parallel combination of R_{shunt} and C_j, which is an appropriate choice because R_{shunt} is often significant in SWIR band diodes. In addition, capacitance readings used usually with phase angles > 80˚ to ensure measurement accuracy.

The capacitance measurements of the device under test were measured up to reverse voltages where the depletion region extended fully into the cladding layers, unless large dark currents prohibited it. The devices with different radii were tested to ensure that the capacitance scaled with area, therefore the doping profile uniformity can also be confirmed. Radius corrections by fitting capacitance per area of devices with different radii can help to determine the active areas of the diodes, because the wet chemical etching technique used to fabricate the devices might undercut the mesa edges by a small amount (estimated to be ~ ± 2-3 µm, depends on the etching depths/ types).

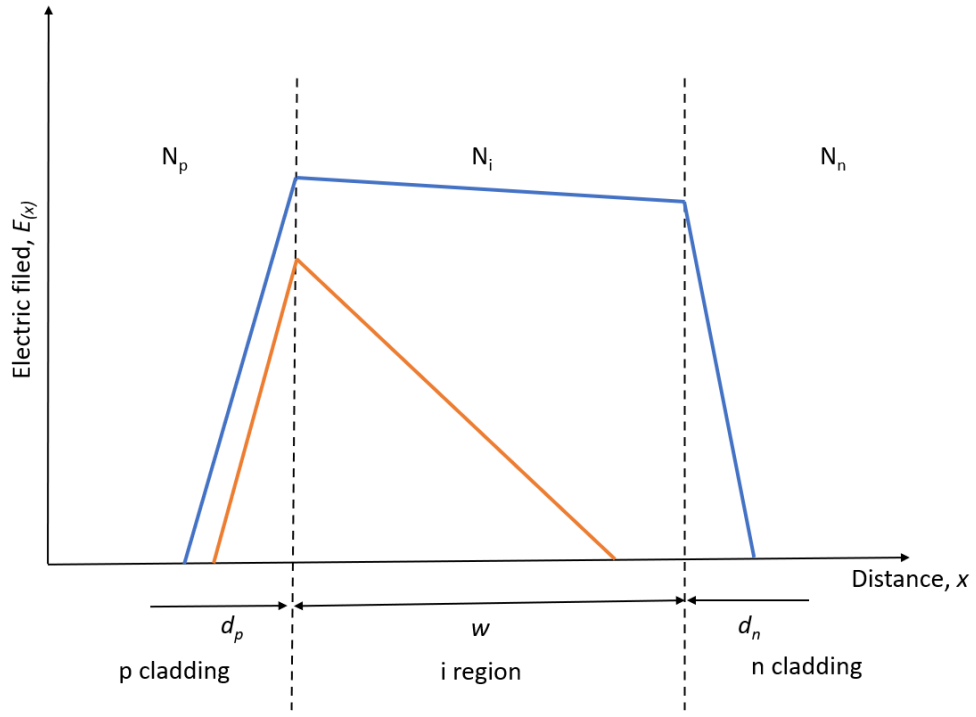

Figure 3.7: 3-region doping profile of pin photodiode assumed in the C-V fitting. Orange line: not-yet-fully depleted. Blue line: fully depleted.

To analyse the data, the doping profiles of the devices were fitted by using an electrostatic model (in Figure 3.7), assuming abrupt 3-region p^+-n^--n^+ doping profiles. N_p, N_i, N_n, and w are doping densities in the p^+ cladding, i-region, and n^+ cladding, and i-region thickness, respectively. d_p, d_i, and d_n are depletion distances in the three regions. The gradient of the electric field with an ionised dopant density N is given by Poisson's Equation [1]:

$$\frac{d\xi}{dx} = \frac{qN}{\varepsilon_r \varepsilon_0}, \tag{3.9}$$

where ε_o and ε_r are the permittivity in vacuum and dielectric constant, respectively. When the i-region becomes fully depleted, $C(V)$ is given by

$$\frac{1}{C(V)} = \frac{1}{A}\left(\frac{d_p(V)}{\varepsilon_p} + \frac{w}{\varepsilon_i} + \frac{d_n(V)}{\varepsilon_n}\right), \tag{3.10}$$

otherwise

$$\frac{1}{C(V)} = \frac{1}{A}\left(\frac{d_p(V)}{\varepsilon_p} + \frac{d_i(V)}{\varepsilon_i}\right). \tag{3.11}$$

The values of thicknesses and doping densities of p, i, and n layers can be adjusted to fit the calculated $C(V)$ to the experimental results.

In accordance with the depletion approximation, the device's capacitance under a reverse voltage is given by

$$C(V) = \frac{\varepsilon_r \varepsilon_0 A}{w_{(V)}} = A\sqrt{\frac{q\varepsilon N}{2\left(V_{bi} + V - \frac{2k_b T}{q}\right)}}. \tag{3.12}$$

Rearranging this gives,

$$\frac{d\left(\frac{1}{C^2}\right)}{dV} = -\frac{2}{q\varepsilon N A^2}. \tag{3.13}$$

Thus, built-in voltage V_{bi} can be estimated from CV measurements by plotting $1/C^2$ against V. Assuming an abrupt single sided junction with constant doping concentration, a straight-line graph is generated and the intercept at $\frac{1}{C^2} = 0$ gives $(V_{bi} - 2k_B T/q)$. An example using C-V data of an $Al_{0.1}In_{0.9}As_{0.83}Sb_{0.17}$ samples giving built-in voltage of -0.1 V is shown in Figure 3.8.

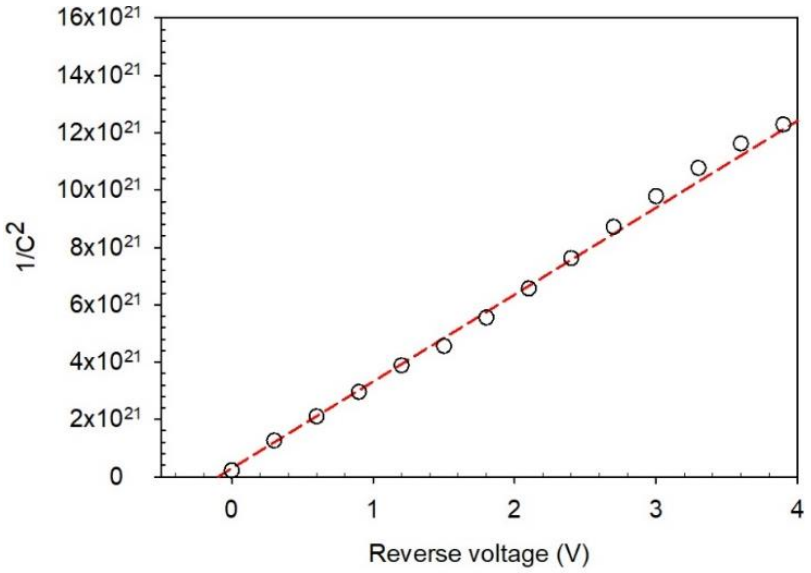

Figure 3.8: A plot of $1/C^2$ versus reverse bias derived from the C-V measurement at 200 K on the AlInAsSb p-i-n diode.

3.3. Photo-response Measurement

The experimental setup of photo-response is depicted schematically in Figure 3.9. A SMU applies reverse bias to the DUT connected with a resistor in series. Illumination on the DUT comes from the output of a monochromator (HORIBA Scientific iHR320), which in turns receives its broadband illumination from a light source (Bentham IL1-IR Halogen with 100W QTH illuminator) via a CaF_2 condenser lens. A diffraction grating in the monochromator splits the broadband illumination into light of different wavelengths. These are focused again by a concave mirror within the monochromator at the monochromator's exit slit. Only light with the chosen wavelength can pass through the exit slit and becomes the output light. The monochromatic light goes through a collimating lens and a microscope objective before being focused onto the DUT. Photocurrent flows in DUT in response to the monochromatic light.

In the setup, phase sensitive detection is used for measuring the DUT's photocurrent in the presence of the DUT's dark current and current due to the ambient light. This is implemented through a mechanical chopper for the light source and a Stanford Research SR830 lock-in amplifier (LIA) to measure the voltage drop across a series resistor induced by the DUT's photocurrent. The chopper rotates at a frequency of 180 Hz and its reference signal is fed to the LIA.

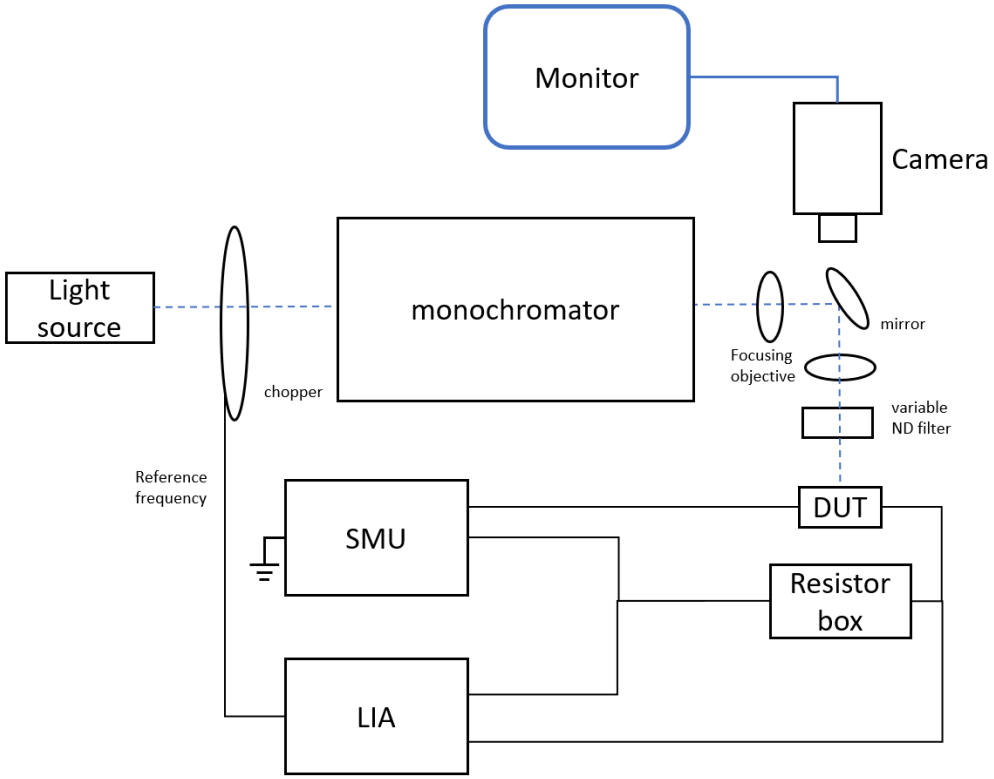

Figure 3.9: Schematic diagram of the experimental setup used to measure photo-response characteristics.

Choosing the correct monochromator grating is important to maximise the monochromator's throughput for the desired wavelength range. Gratings are classified by their number of grooves per unit length, with a specified blaze wavelength. 3 gratings are installed inside the monochromator, (i) 1800 groove/mm grating with blaze wavelength of 400 nm, (ii) 600 groove/mm grating with blaze wavelength of 1000 nm and (iii) 300 groove/mm grating with blaze wavelength of 2000 nm. In this work, 600 groove/mm grating was chosen to measure the photoresponse of the samples. The usable wavelength range of this grating is 667 - 2000 nm, as the wavelength range with reasonable efficiency has the lower limit and upper limit of 2/3 and 2 of λ_{blazed}, respectively, any wavelength outside this range will have a reduced efficiency. To measure the photoresponse of a given photodiode over the 900 to 2400 nm wavelength range, three scans were taken using the following wavelength ranges (a) 900-1600 nm (b) 1400-2000 nm and (c) 1800-2400 nm. Two optical long-pass filters, with transition wavelengths of 850 and 1300 nm, were used in combination with (b) and (c) to avoid second order light from the monochromator to affect the measurements. Although wavelength range (c) extends slightly beyond the typical usable range of the 600 groove/mm grating (~ 666 – 2000 nm), the photoresponse data were similar to those obtained using the 300 groove/mm grating (~ 1333 –

4000 nm). Therefore, the photoresponse measurements made use of the 600 groove/mm grating for all three scans, avoiding frequent changes in monochromator's grating.

By shining the light with high power (> band gap) on the photodiode, the photons will be absorbed to create the electron-hole pairs. The photogenerated carriers in the depletion region are separated by the electric field and collected, generation a current in the external load. Any absorption of light outside the depletion region has a negative effect on the device quantum efficiency because carriers photogenerated must diffuse to the depletion region to contribute to the photocurrent. As a resistor is connected in series with the DUT, LIA can measure the voltage drop across the resistor. Equation 3.14 shows the relationship between the conversion value of LIA and photovoltage drop across the devices. The factor of 0.45 relates the peak voltage value to the LIA's displayed output (the Root-Mean-Square value of the sine wave at the reference frequency (f_{ref}) [2]). Photocurrent will be calculated in Equation 3.15 for an input wave with $V_{p-p} = 2$ V.

$$LIA\ reading\ (V) = \frac{conversion}{10} \times sensitivity \tag{3.14}$$

$$I_{ph} = \frac{LIA\ reading(V) \times \sqrt{2} \times \pi}{2} \times \frac{1}{R_{sense}} \approx \frac{LIA\ reading(V)}{0.45 \times R_{sense}} \tag{3.15}$$

From Equation 2.3, optical power at each wavelength can be obtained, as shown in Equation 3.16.

$$P_{opt} = \frac{I_{ph}}{R} \tag{3.16}$$

In this work, 0.5 mm - diameter ex-InGaAs photodiode, FD05D, is used as reference sample because its similarity in the range of wavelength detection and active window area. The FD05D photodiode responsivity graph in shown in Appendix A.

3.4. Avalanche Gain Measurement

The basic photo-multiplication measurement was performed using the set-up shown schematically in Figure 3.10. It is similar to the photo-response setup except that the illumination has been replaced by a laser. A small laser light spot was focused to illuminate the top surface of the DUT via focusing and microscope objectives. A Stanford Research SR830 lock-in amplifier is used to measure the DUT's photocurrent via a series resistor. The light spot

size should be minimised (~ 10 μm) to prevent the light falling on the edge of the mesa, which can cause mixed carrier injection. The wavelengths of lasers can be altered to achieve pure injection of electrons (holes) or mixed injection of electrons and holes, as intended. These conditions produce electron-initiated (M_e), hole-initiated (M_h), or mixed multiplication (M_{mix}), respectively.

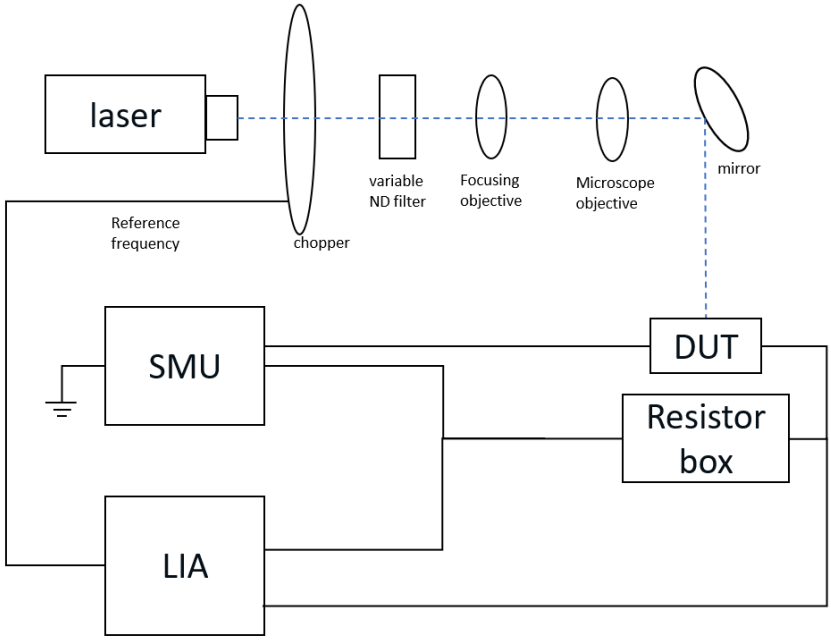

Figure 3.10: Schematic diagram of the experimental setup used to measure photo-multiplication characteristics.

The electrons and holes in the devices are generated by illuminating the devices and accelerated to impact ionise under high reverse voltage. The unmultiplied primary current I_{pri} is contributed by the initial injected carriers generated by photons. Under the high reverse bias in i-region, some or all injected carriers can give rise to impact ionisation events, so the current would be amplified by multiplication factor M and photocurrent I_{ph} flowing in the device can be generated. Then, the multiplication factor is given by:

$$I_{ph} = \frac{V_{LIA}}{R \times 0.45}, \tag{3.17}$$

And

$$M = \frac{I_{ph}}{I_{pri}}, \tag{3.18}$$

where the magnitude of I_{ph} needs be at least 2 orders larger than dark current. I_{pri} represents the gain is unity (M = 1) and it could be determined from the dark current characterisation.

3.5. Temperature dependence studies (300 – 77 K)

Since the electrical and optical properties of an APD show varying extents of temperature dependence, characterising photodiodes at low temperature is desirable and can provide more information on the behaviours of photodiodes. The temperature dependence studies in this thesis are conducted with either a a Model ST-500 continuous flow cryogenic probe station or a Model 22 CTI Cryodyne Refrigerator System.

In Model 22 CTI Cryodyne Refrigerator System, the devices can be packaged onto TO-5 headers using gold wire bonding and mounted into a closed cycle helium compressor system that can go down to ~ 15 K. The device temperature is monitored by a Si temperature sensor (LakeShore DT-471-CU) and controlled by a built-in heater via a temperature controller. Low-pressure and low temperature environments allow low temperature dark current measurements.

In Model ST-500 continuous flow cryogenic probe station, the unpackaged (bare die) samples are placed in a liquid nitrogen continuous flow cryostat. The cold fingers from the temperature controller for temperature monitoring is located underneath the sample positioning chuck, and the device temperature can be controlled from room temperature to 77 K. The cryostat system has four micromanipulator probe arms with two probes, a single mode fiber and a multi-mode fiber. Low temperature I-V, C-V and photoresponse characteristics can be measured by connecting SMU, LIA, monochromator to Janis Probe station. More experimental details will be discussed in chapter 4 and 5.

The temperature dependence of dark current can be fitted with the Arrhenius Equation as in Equation 3.19 where ∀ is a pre-exponential factor, E_A is the activation energy.

$$I = \forall exp\ (-\frac{E_A}{kT}) \tag{3.19}$$

E_A can be determined by obtaining a linear plot between ln I vs $1/T$. The value of activation energy reflects on the dominant mechanism of action. When activation energy close to E_g, the dominant leakage current mechanism is diffusion current, whereas activation energy close to $E_g/2$ suggests the presence of mid gap trap levels, the dominant leakage current mechanism is G-R current.

3.6. Reference

[1] S. M. Sze and K. K. Ng, *Physics of semiconductor devices*, 3rd ed. Hoboken, N.J: Wiley-Interscience, 2007.

[2] C. H. Tan, 'PhD Thesis: Measurements of excess avalanche noise in sub-micron Si and $Al_{0.6}Ga_{0.4}As$ avalanche photodiodes', in *Electronic & Electrical Engineering*: The University of Sheffield, 2001.

4. Characterisation of InGaAs/GaAsSb Type-II Superlattice Photodiodes

Compared to several SWIR photodiodes technologies, including HgCdTe, ex-InGaAs, and InAs, InGaAs/GaAsSb T2SL has been suggested as a good replacement. Cutoff wavelength of InGaAs/GaAsSb T2SL PDs on InP substrates can be engineered to cover the SWIR band by tailoring the superlattice well (InGaAs) and barrier (GaAsSb) thicknesses and/or compositions. Lattice-matched 5 nm/5 nm InGaAs/GaAsSb T2SL photodiodes were reported by different research groups with λ_c of 2.4 – 2.5 µm at near room temperature [1] and responsivities of 0.47– 1.4 A/W at 2.04 – 2.18 µm. Simulation studies for InGaAs/GaAsSb T2SL photodiodes were also limited to the lattice matched 5 nm/5 nm InGaAs/GaAsSb T2SL design [1]–[3]. Furthermore, the simulations were performed without experimental validation.

This chapter focuses on characterisations of InGaAs/GaAsSb T2SL photodiodes with a range of T2SL designs. The data include temperature dependence of I-V, C-V and photoresponse characteristics. Data of temperature dependent cutoff wavelength were used to validate a nextnano simulation model for InGaAs/GaAsSb T2SL designs. The model is applicable for both strained and lattice-matched SWIR InGaAs/GaAsSb T2SL.

4.1. Device Structure and Fabrication details

4.1.1. Planar photodiodes

The first round of wafer growths was carried out by III-V lab in France. These MBE grown wafers were designed for producing planar photodiodes (lattice matched to InP substrates) via Zn diffusion. The MBE reactor used was equipped with As and Sb crackers. During wafer growth processes, two Ga cells were used to facilitate independent control of the $In_{0.53}Ga_{0.47}As$ and $GaAs_{1-x}Sb_x$ growth conditions. Table 4.1 summarises structures of the 4 wafers from this round, namely wafer III-V-1, III-V-2, III-V-3, and III-V-4. Except for III-V-1 (bulk InGaAs), the rest were T2SL wafers. The intended InGaAs/GaAsSb T2SL designs for wafer III-V-2, III-V-3, and III-V-4 were 3 nm/3 nm, 5 nm/5 nm and 7 nm/7 nm, with λ_c of 2.09, 2.31 and 2.50 µm, respectively. Due to errors during wafer growths of III-V-3, and III-V-4, their T2SL thicknesses became 3 nm/5 nm and 3 nm/7 nm. Despite the changes, these wafers still offer a range of λ_c values (2 – 2.2 µm) appropriate for the work.

The wafers were capped with a 70 nm InGaAs layer, which serves to (i) encapsulate and protect the InAlAs, which is prone to oxidation, (ii) aid Zn diffusion, due to the high solubility of Zn in InGaAs, and (iii) minimise the contact resistance to the *p*-type region. 1.0 µm thick wide bandgap n^--InAlAs layers were included to minimise minority electron diffusion current into the depletion region. n^--InGaAs layers were included for all wafers to help create abrupt Zn profiles after Zn diffusion.

A schematic cross-sectional view of the fully fabricated device is shown in Figure 4.1. Zn diffusion was carried out by SRI International to diffuse Zn into part of the n^--InAlAs layer to create *p*-region. The conditions used were a temperature of 515 °C and a total diffusion time of 75 minutes. SIMS data from sample III-V-1 after Zn-diffusion is shown in Figure 4.2. It includes the Zn concentration profile as well as relative fractions of Al and Ga (to identify the two InAlAs/InGaAs heterojunctions). The Zn atoms extend ~ 200 nm into the 1500 nm thick InGaAs layer as intended.

A low diffusion temperature was used to preserve the superlattice interface quality. In an effort to reduce surface leakage currents, parts of the n^+-InGaAs layer were etched. Ti/Au (20/200 nm) was used to form *p*- and *n*- electrical contacts.

Table 4.1: Wafer structure details of planar p-i-n wafers.

Thickness (nm)				**Material**	**Doping type**	**Doping level (cm^{-3})**
III-V-1	**III-V-2**	**III-V-3**	**III-V-4**			
Bulk InGaAs	**T2SL**	**T2SL**	**T2SL**			
70	70	70	70	$In_{0.53}Ga_{0.47}As$	i	i
1000	1000	1000	1000	$In_{0.52}Al_{0.48}As$	n (Si)	2.0E16
3000	1500	1500	1500	$In_{0.53}Ga_{0.47}As$	n (Si)	5.0E15
-	3/3 (×165 repeats)	3/5 (×100 repeats)	3/7 (×70 repeats)	$In_{0.53}Ga_{0.47}As$/ $GaAs_{0.51}Sb_{0.49}$	i (Si)	5.0E15
200	200	200	200	$In_{0.53}Ga_{0.47}As$	n^+ (Si)	2.0E18
n^+ InP Substrate						

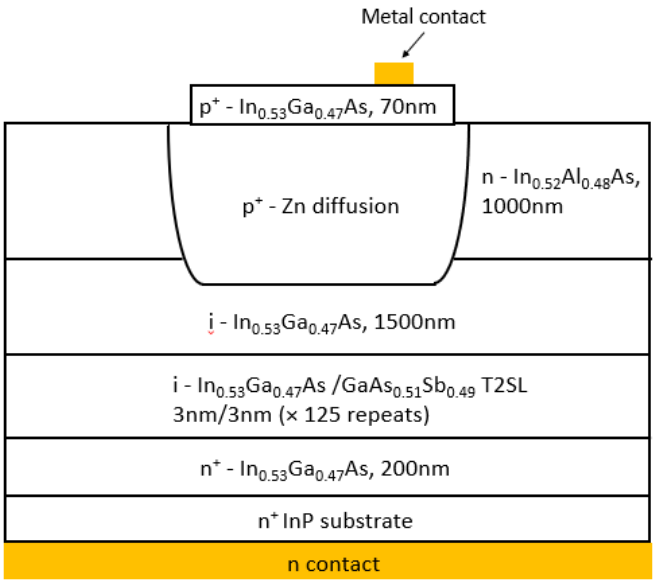

Figure 4.1: Schematic cross-sectional view of the planar InGaAs/GaAsSb T2SL photodiodes III-V-1.

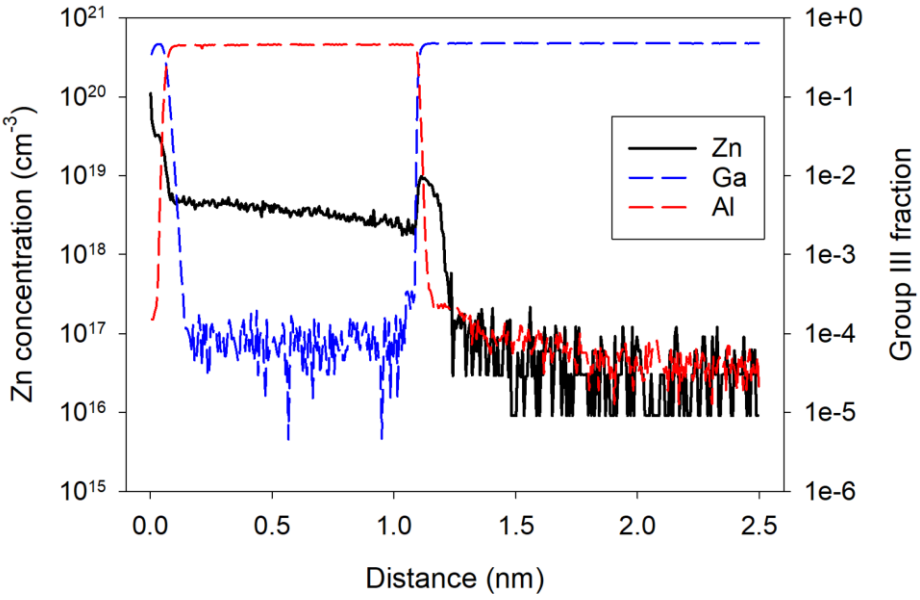

Figure 4.2: SIMS data (Zn profile and the relative fractions of Ga and Al) of III-V-1,

4.1.2. Mesa photodiodes

A further two T2SL wafers were grown by III-V Lab and Prof. Mark Hopkinson's group at the University of Sheffield to produce mesa T2SL photodiodes. The reasons to switch to mesa structure are (i) the delay in producing planar diodes, (ii) uncertainty in device sizes, and (iii) potential peripheral leakage currents (will be discussed in Chapter 4.2 and 4.3). Both were grown on n^+ InP substrates using MBE reactors equipped with two Ga cells to facilitate

independent control of the $In_{0.53}Ga_{0.47}As$ and $GaAs_{1-x}Sb_x$ growth conditions. Table 4.2 summarises of wafer structure details of K466 and III-V-5.

Table 4.2: Wafer structures of III-V-5 and K466

Thickness (nm)		**Material**	**Doping type**	**Doping level (cm^{-3})**
K466	**III-V-5**			
70		$In_{0.53}Ga_{0.47}As$	p^+ (Be)	1.0E19
1000		$In_{0.52}Al_{0.48}As$	p (Be)	2.0E18
1000		$In_{0.53}Ga_{0.47}As$	i	i
5/3 (×125 repeats) XRD fitting: 5.5/3	5/3 (×250 repeats) XRD fitting: 2/6	$In_{0.53}Ga_{0.47}As$/ $GaAs_{1-x}Sb_x$	i	i
800	200	$In_{0.53}Ga_{0.47}As$	n^+ (Si)	2.0E18
n^+ InP Substrate				

Wafer III-V-5 used compositions of $In_{0.53}Ga_{0.47}As/GaAs_{1-x}Sb_x$ (x = 0.49) that are meant to be lattice matched to InP substrates, as in the case of the wafers for planar photodiodes. In contrast, wafer K466 contains lattice mismatched $GaAs_{1-x}Sb_x$ with x = 0.40. T2SL periods and compositions of K466 and III-V-5 were assessed using theta-theta X-Ray diffraction (XRD) spectrometry and Transmission electron microscopy images (TEM). XRD spectra (Figure 4.3) were measured by Dr Jonathan Petticrew at the University of Sheffield using an Empyrean XRD from Malvern Panalytical. The XRD system was fitted with a copper x-ray source, PIXcel 3D detector, and 4 bounce Ge022 monochromator. TEM measurements were completed by Integrity Scientific Ltd, UK.

X-Ray Server was used to perform the fitting to the XRD data [4]. To fit the XRD data, first the T2SL period was obtained from the spacing of the fringe peaks. Then the bulk InGaAs layers were fitted. In both wafers the composition of InGaAs was the lattice matching one, i.e. [In] = 0.53. Finally, assuming identical composition for InGaAs in the T2SL and the bulk InGaAs, the GaAsSb composition was adjusted so that the XRD fitting matches with the data (focusing on the position of the T2SL peaks). These GaAsSb compositions from the XRD fittings are similar to prior GaAsSb calibration wafers.

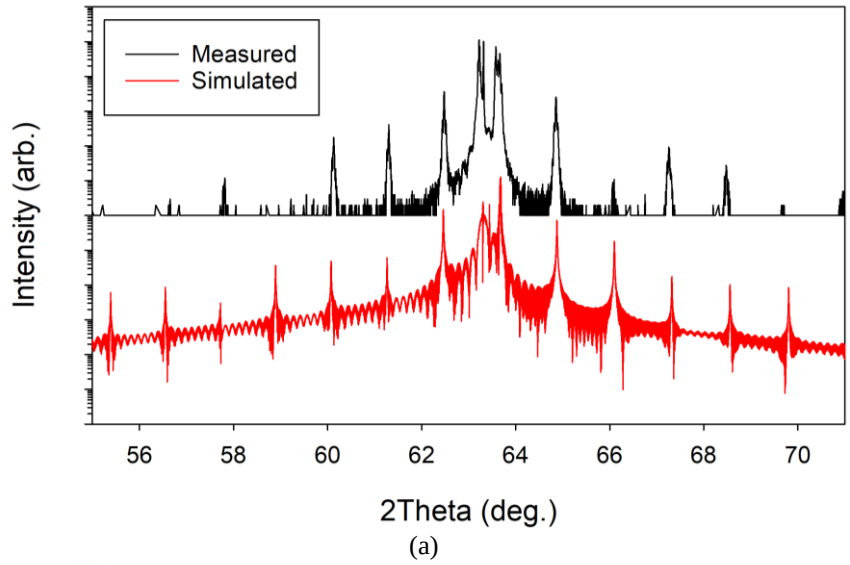

(a)

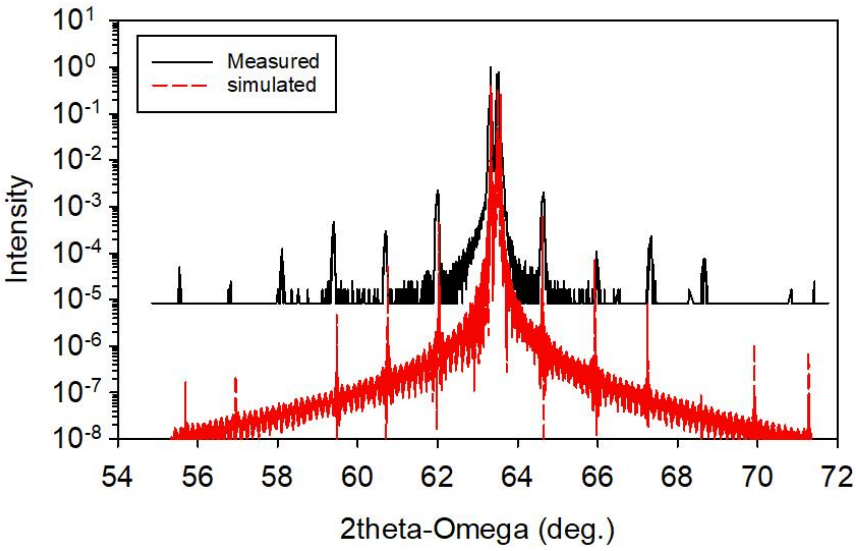

(b)

Figure 4.3: Experimental (black line) and simulated (red line) XRD characteristics of (a) K466 with 8.5 nm T2SL period (b) III-V-5 with 8 nm T2SL period, measured with 0.002 degree between points.

To further resolve the individual layers within the period, TEM was carried out on samples of both wafers. Cross-sectional TEM images, shown in Figure 4.4 (a) and (b) for wafer K466 and III-V-5, respectively, indicate that the T2SL periods are consistent with the XRD results. To extract layer thicknesses within the period from TEM images, the imaging software FUJI (based on imageJ2) was used to extract pixel values.

Analyses were carried out on the TEM images in an attempt to extract more accurate information on thicknesses, using image processing software FIJI and scientifi graph plotting software Sigmaplot. Counting the number of pixels within the scale bar of 50 nm yielded the thickness covered by a pixel in unit of nanometers. These values were then used to estimate

the thicknesses of InGaAs and GaAsSb layers, after counting the number of pixels (± 0.5 pixels on each side, total ± 1 pixel) within each layer. These are shown in Figure 4.4 (c) - (f). For each image (i.e. wafer), the image analysis process was carried out a total of 3 times at different parts of the image. Table 4.3 summarises the mean and standard deviation of the thicknesses of InGaAs and GaAsSb layers for both wafers. The InGaAs/GaAsSb superlattice periods are 7.8 nm for K466 and 8.33 nm for III-V-5. The value for K466 is close to that from XRD data (8.5 nm). Hence the periodicity is taken as 7.8 to 8.5 nm for K466.

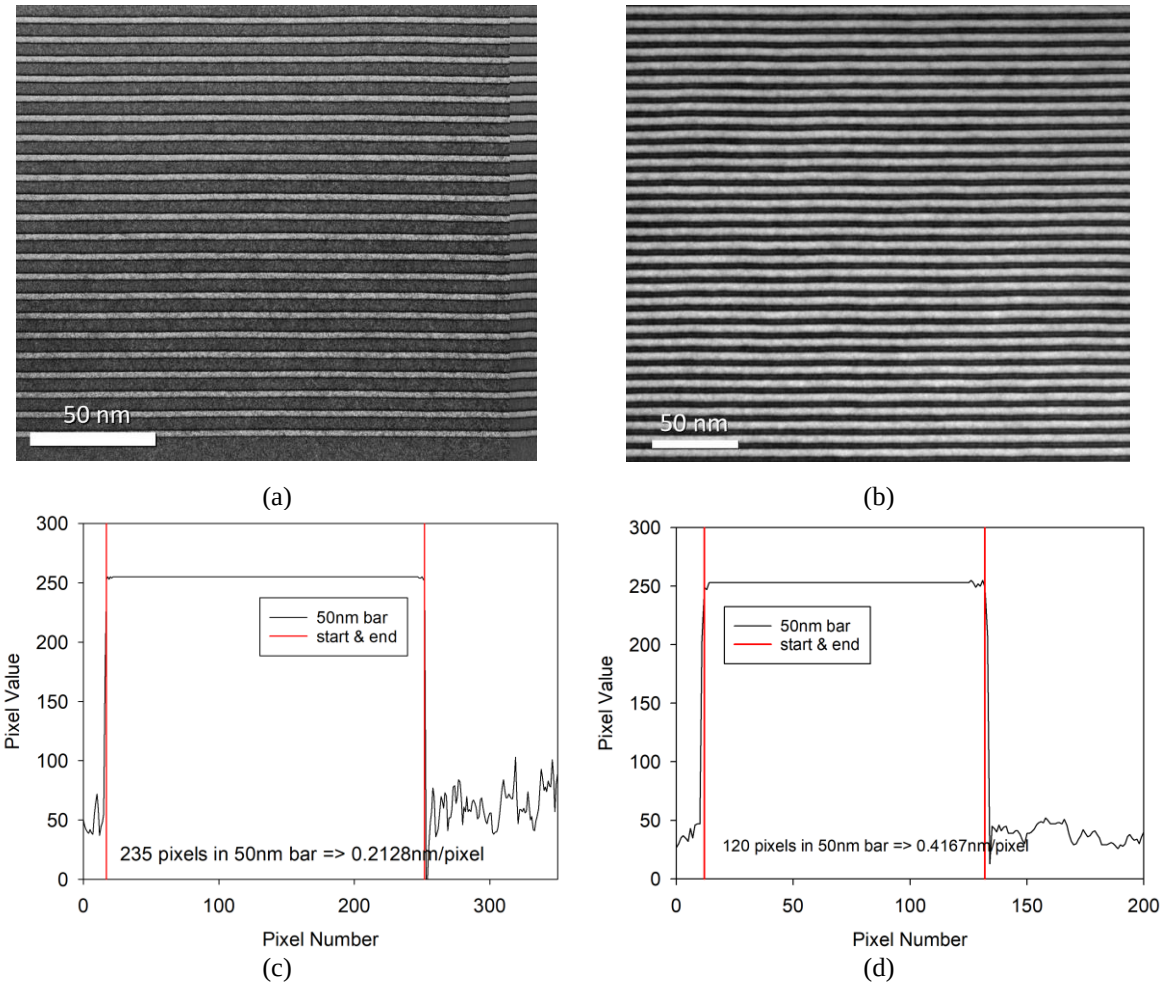

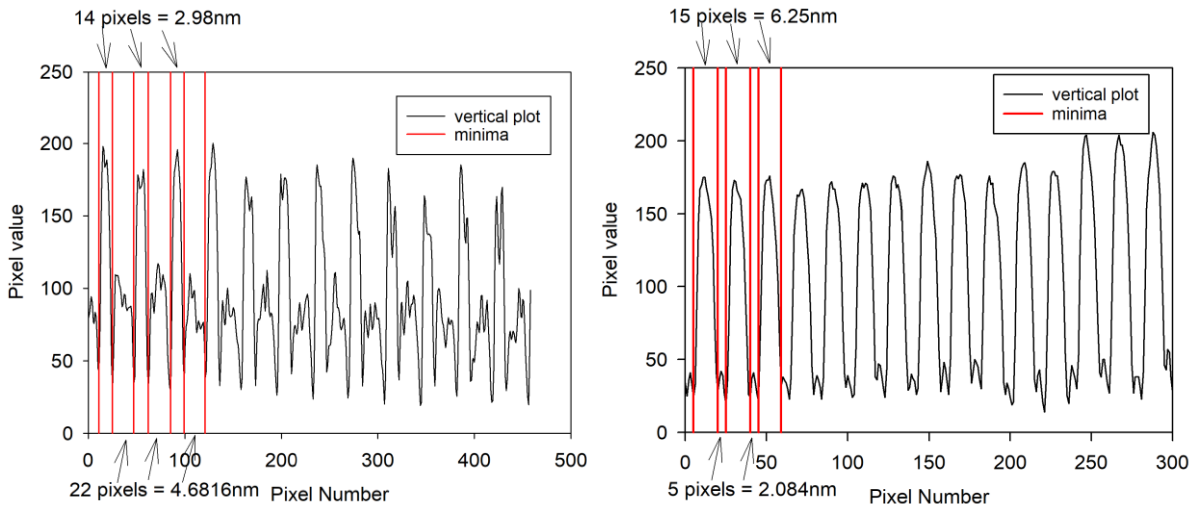

Figure 4.4: TEM images of wafer (a) K466 and (b) III-V-5 supplied by Integrity Scientific Ltd. Image analyses were carried out to extract thickness information for (c)/(e) K466 and (d)/(f) III-V-5.

Table 4.3: the mean and standard deviations of wafers K466 and III-V-5.

samples	Distance /Pixel (nm/pixel)	Mean Thickness of GaAsSb (nm)	Mean thickness of InGaAs (nm)	Total thickness (nm)	stddev thickness of GaAsSb (nm)	stddev thickness of InGaAs (nm)
K466	50/235	3.05	4.75	7.8	0.12	0.12
III-V-5	50/120	6.25	2.08	8.33	0	0

Circular mesa diodes with 420, 220, 120, 70 µm in diameter were fabricated by Dr. Jonathan D. Petticrew using NEWPIN photolithography mask set with the etching pattern of a diluted nitric acid solution of HNO_3: H_2O (ratio 2:3) [5]. This etching process achieved device isolation with clean mesa floors. 20/ 200 nm Ti/Au contacts were deposited on the top of each isolated mesa and the substrates to form *p*- and *n*-contacts, respectively. There were no passivation and anti-reflection coatings on the devices.

4.2. Capacitance-Voltage measurements

C-V characteristics were performed in the dark room using a probe station and a HP4275A LCR meter. In a purely capacitive circuit, current leads voltage, hence the ideal phase angle difference between I_{AC} and V_{AC} is 90˚. In this work, the phase angles of most devices tested are from 85˚ to 90˚. Capacitances are expected to vary with the diodes' areas. Moreover, the device

area may vary from the dimensions in the photolithography masks used to define either the Zn-diffusion area or the mesa area, for the planar and mesa photodiodes, respectively.

4.2.1. C-V of planar photodiodes

Room temperature C-V experimental data were obtained from planar devices of wafers III-V-1 to III-V-4. The C-V data of III-V-2 and III-V-4 were inconsistent, for given device radius, for they are not shown here. The C-V data of III-V-1 and III-V-3 scale well with device area, when the radius values were adjusted by adding 3.9 and 4.0 µm, respectively. The data are presented as capacitance density in Figure 4.5. In contrast to apply subtraction to radius values for mesa devices, the additions to radius values for these planar devices show that the Zn diffusions into the semiconductor layers have spread laterally, increasing the device areas.

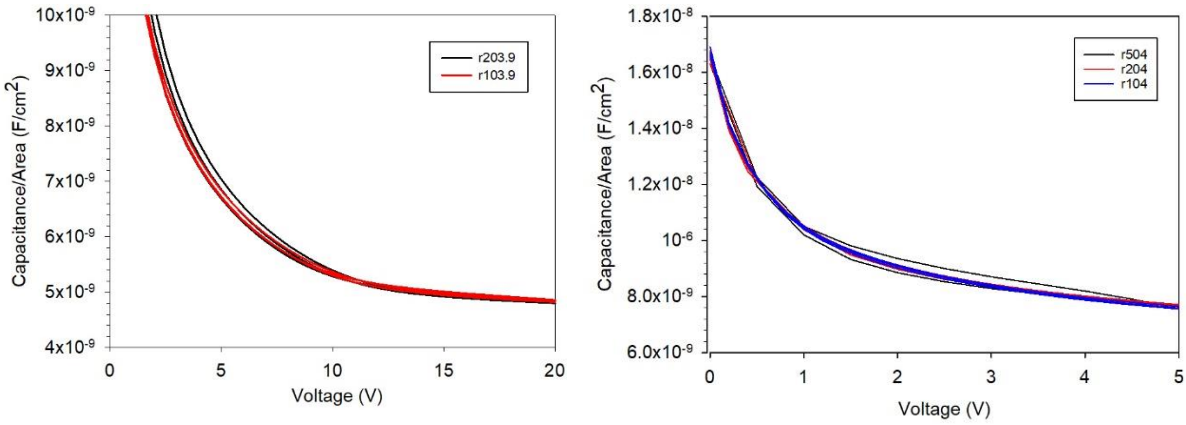

(a) (b)

Figure 4.5: Capacitance density versus reverse bias data for (a) III-V-1 and (b) III-V-3. Larger device radii values compared to Zn-diffusion mask design were used and the additions are (a) 3.9 µm and (b) 4.0 µm.

4.2.2. C-V of mesa photodiodes

Room temperature C-V data of devices with 420, 220, 120 and 70 µm diameter from K466 and III-V-5 are shown in Figure 4.6. For wafer K466, the capacitance density results from different sized devices are in agreement, as shown in Figure 4.6 (a), without any adjustment of radius values. For III-V-5, the radial correction needed was - 5 µm. InGaAs layers are fully depleted at ~ - 6 and ~ - 4 V, for wafer K466 and III-V-5, respectively.

Doping profile and i-layer thickness were extracted from the C-V data of wafer K466 and III-V-5. The relative permittivity assumed for the i-layer was 14, which is the weighted mean of

the relative permittivity values of $In_{0.52}Al_{0.48}As$, $In_{0.53}Ga_{0.47}As$, and $GaAs_{0.51}Sb_{0.49}$ (12.46, 13.9, and 14.4 [6]). The estimated doping profiles are also shown in Figure 4.6. The i-InGaAs and i-T2SL intrinsic regions have different unintentional doping levels. The first intrinsic level (~ 1×10^{15} atoms/cm^{-3}) has a thickness of 1000 nm, suggesting that this is the i-InGaAs layer. The other intrinsic level (~ 8×10^{15} atoms/cm^{-3}) has a thickness of ~ 1.0 and 2.0 µm, for wafer K466 and III-V-5, respectively. These values match with the intended thicknesses of T2SL layers in K466 and III-V-5 as well as the values from TEM data (975 and 2082 nm, respectively). Hence this unintentionally doped region (~ 8×10^{15} atoms/cm^{-3}) corresponds to the T2SL layers.

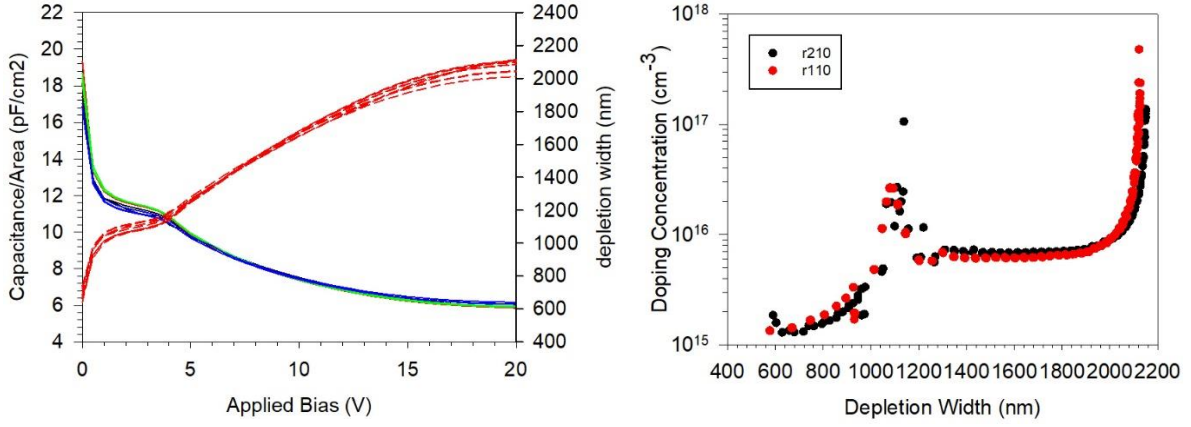

(a)

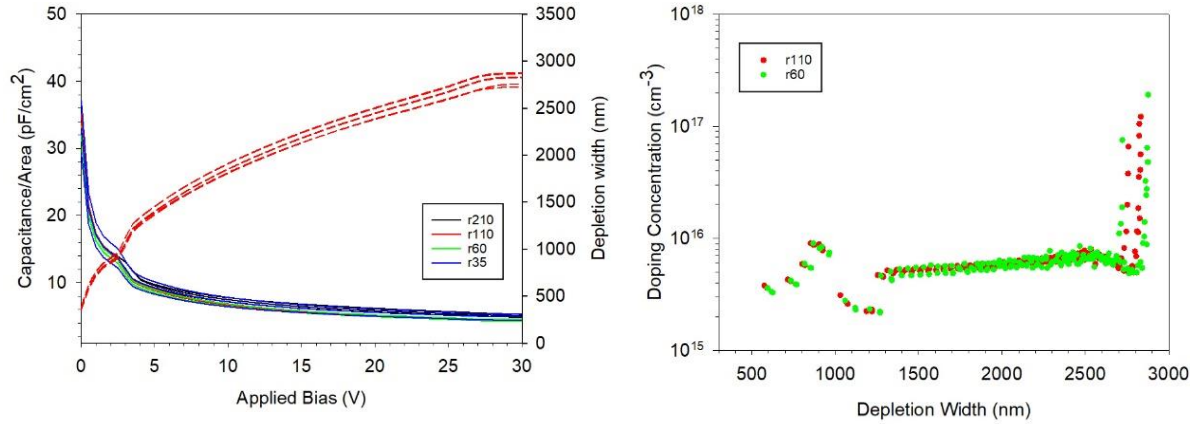

(b)

Figure 4.6: Reversed Capacitance/area data (solid lines, left axis) and total depletion widths with applied bias (dashed lines, right axes) for (a) wafer K466 and (b) wafer III-V-5.

4.3. Current-voltage measurements

4.3.1. I-V of planar photodiodes

Room temperature dark current data were obtained from wafer III-V-1 and III-V-3 using planar devices with 500, 200, 100, 50, and 25 radii. The dark current densities from the different-sized devices are in agreement (with radius additions were applied), as shown in Figure 4.7. This indicates that dark currents within the narrow voltage range at room temperature are dominated by bulk leakage mechanism(s).

Dark current densities of III-V-1 and III-V-3 at - 0.1 V were 35 - 145 and 2 - 20 µA/cm^2, respectively. Although, these are very low compared to typical T2SL dark current densities (e.g. 2.6 mA/cm^2 from [7]), it is emphasised that they are likely to correspond to only the i-InGaAs part of the wafers and do not include dark currents from the T2SL, based on I-V data of mesa photodiodes (presented below). Due to Zn diffusion issues (such as potential peripheral leakage currents), these devices were not characterised by high reverse voltages.

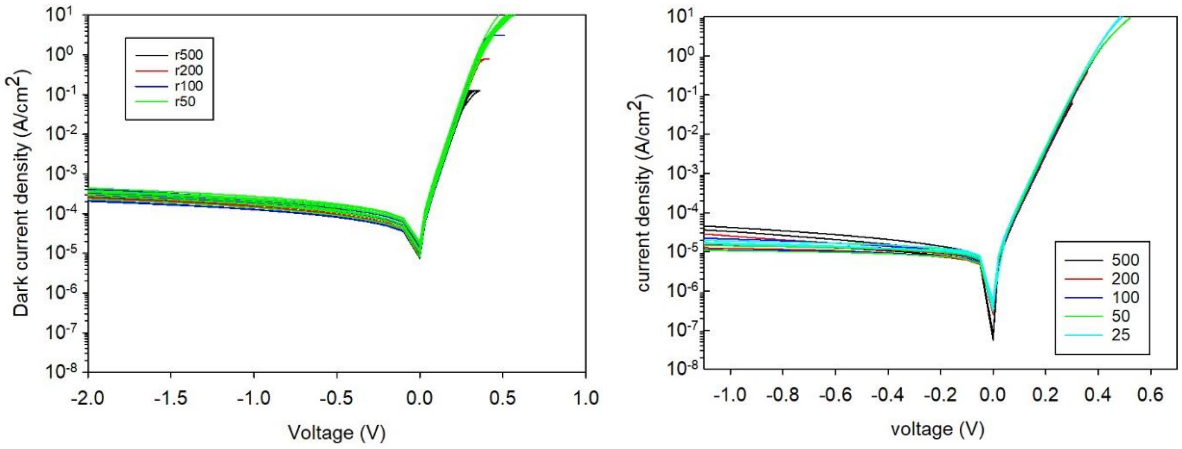

(a) (b)

Figure 4.7: Dark current density data of wafers (a) III-V-1 and (b) III-V-3 at room temperature. Data are from devices with radii of 500, 200, 100, 50 and 25 µm.

4.3.2. I-V of mesa photodiodes

Forward and reverse dark current characteristics of mesa samples K466 and III-V-5 were placed in a low-temperature probe station and measured at room temperature to 200 K. Figure 4.8 compares the forward and reverse dark current density characteristics of devices with 420, 220, 120 and 60 µm diameters from wafer K466 and III-V-5. For both wafers, the J_{dark} data exhibit a step increase (more abruptly in K466 than in III-V-5) at high reverse voltage. These

voltage points are consistent with those in the C-V data (~ - 6 V for K466 and - 4 V for III-V-5).

When using dark current densities of T2SL wafers for comparisons, it is therefore important to choose the voltage points appropriately. Room temperature T2SL-related dark current densities of K466 at -6 V and III-V-5 at - 4 V were ~ 55 and 300 µA/cm^2, respectively.

For voltages beyond these key voltage points, the dark current densities from different-sized devices are in good agreement, for a given wafer. Therefore, dark currents from the T2SL layers are dominated by bulk leakage mechanisms. For both wafers, dark current densities decrease as temperature decreases. This is expected due to the strong temperature dependence of bulk leakage mechanisms such as diffusion and generation-recombination currents.

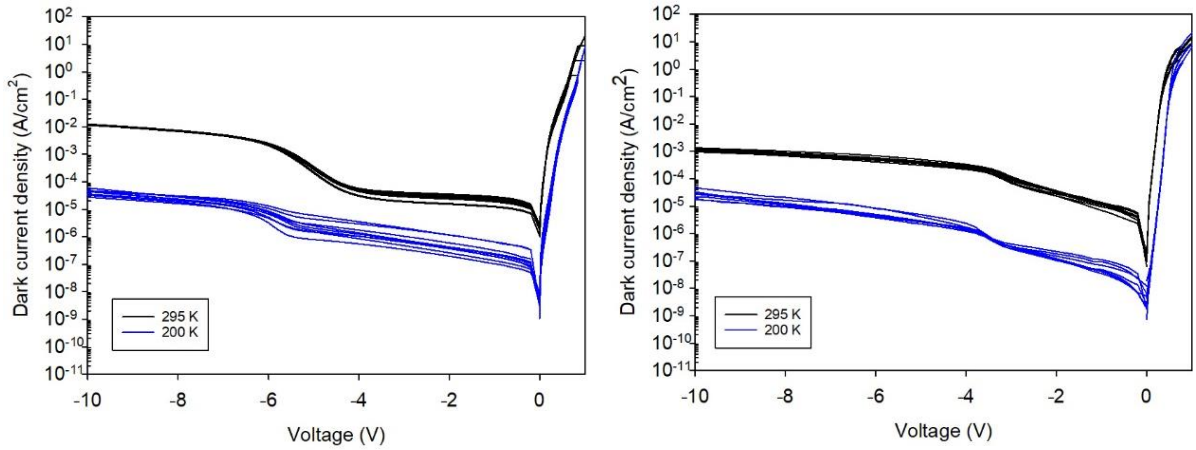

Figure 4.8: Dark current density data of wafers (a) K466-070621and (b) III-V-5. at 295 and 200 K. Data are from devices with diameter of 420, 220, 120 and 60 µm.

Figure 4.9 compares dark current density of K466 and III-V-5 at - 5 V to that of $In_{0.53}Ga_{0.47}As/GaAs_{0.51}Sb_{0.49}$ T2SL photodiodes at - 1 V at different temperatures from the literature, with cutoff wavelengths of 2 to 3 µm [7]–[9]. The T2SL layers used in these photodiodes from the literature are 5nm/5nm. Dark current densities of K466 and III-V-5 are at least ~ one order of magnitude lower than others, and only ~ one order of magnitude higher than values obtained using Rule 07 at a function of temperature from 300 to 180 K.

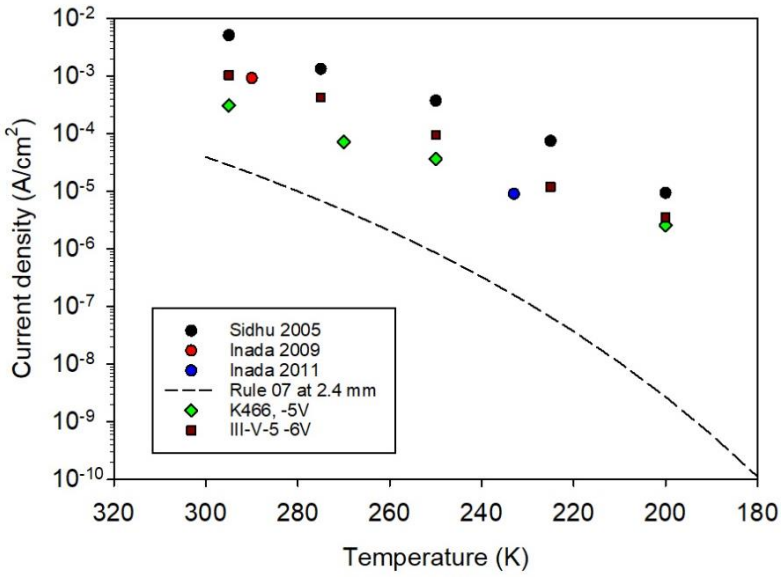

Figure 4.9: Comparison of dark current densities at different temperatures for K466, III-V-5 (at - 5 V) and T2SL InGaAs/GaAsSb photodiodes (at -1 V).

4.4. Temperature dependent photoresponse characterisation

Temperature dependent photocurrent versus wavelength measurements were carried out on the device-under-test (DUT) placed in a low temperature probe station. A monochromator (using a grating with a 2.0 µm blaze wavelength) with a tungsten-halogen lamp provided the optical signal, which was mechanically chopped at 180 Hz before being delivered to the devices via optical fibres connected to the probe station. Two optical long pass filters, FELH0850 and FELH1300, filtered out optical signal with shorter wavelengths. The end of the final optical fibre was positioned above the DUT's optical window. Phase-sensitive detection was employed (with a lock-in amplifier) to measure the resultant photocurrent flowing in the DUT in the presence of reverse dark current. For each wafer and temperature, data were obtained from three same-sized devices.

A commercial photodiode FD05D with a known responsivity versus wavelength characteristic was used to obtain the measurement system response. i.e. optical power versus wavelength characteristic, $P_{opt}(\lambda)$. This was used to extract the DUT's responsivity, $R_{DUT}(\lambda) = I_{ph}(\lambda) / P_{opt}(\lambda)$. The DUT's quantum efficiency was then calculated using $\eta(\lambda) = R_{DUT}(\lambda) / R_{ideal}(\lambda)$, where R_{ideal} is given by Eqn. (2.4). Figure 4.10 shows room temperature photocurrent characteristics of K466-070621 at reverse biases from - 0.2 to - 7 V. For a given wavelength, rate of photocurrent

increase with reverse bias slows after - 6V. This is consistent with the devices being fully depleted by ~ - 6 V. Similar observations were made on wafer III-V-5 at ~ - 4 V.

Assuming the same amount of light was radiated on the diodes, the devices of K466-070621 achieved up to 60 % quantum efficiency without antireflection coating at reverse biases from - 0.2 to - 7 V, across the measured wavelengths (900 - 1600 nm). Quantum efficiency will then drop rapidly when light wavelengths close to λ_c.

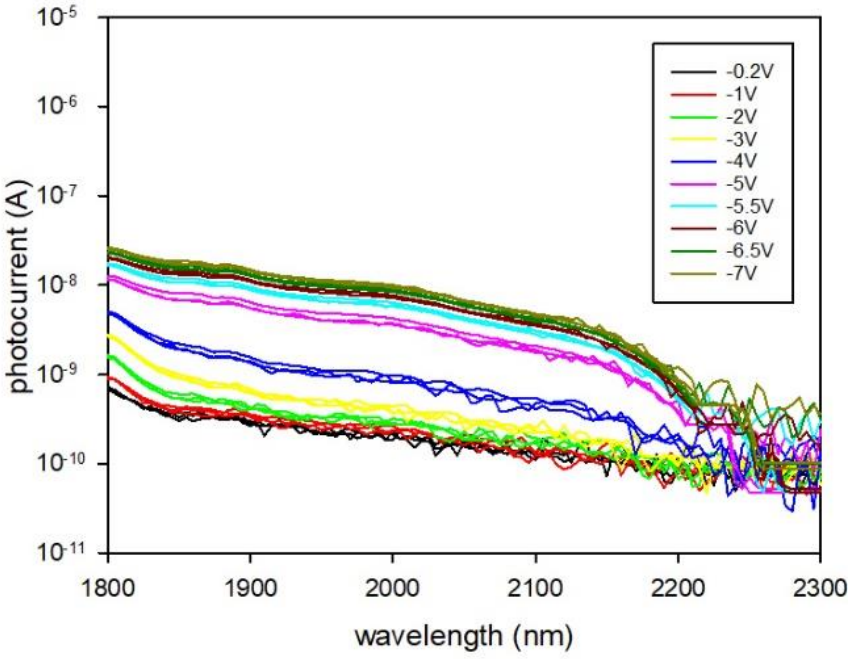

Figure 4.10: Room temperature photocurrent characteristics of K466-070621 by applying biases from - 0.2 to - 7 V.

These observations above informed experimental conditions of analyses to extract λ_c as a function of temperature for both wafers. For a given wafer and temperature, photoresponse data at appropriate reverse bias (-7 V for K466 and -6 V for III-V-5) were used. For each wafer and temperature, $\eta^2(\lambda)$ data were obtained from three same-sized devices. λ_c for a given temperature was extracted by linear regression fitting to the $\eta^2(\lambda)$ characteristics. From these linear regressions λc was defined where η^2 reaches zero, as shown in Figure 4.11. λ_c at room temperature of K466 and III-V-5 is 2200 and 2070 nm, respectively. The full temperature dependence of λ_c were used as reference data for validating nextnano simulation model for T2SL. In some T2SL works, λc is defined by 50 % of the maximum photocurrent or responsivity value. Such definition was not used for this work because it can be affected by

features in the photocurrent or responsivity versus wavelength characteristics (e.g. Fig. 4 in ref [5]).

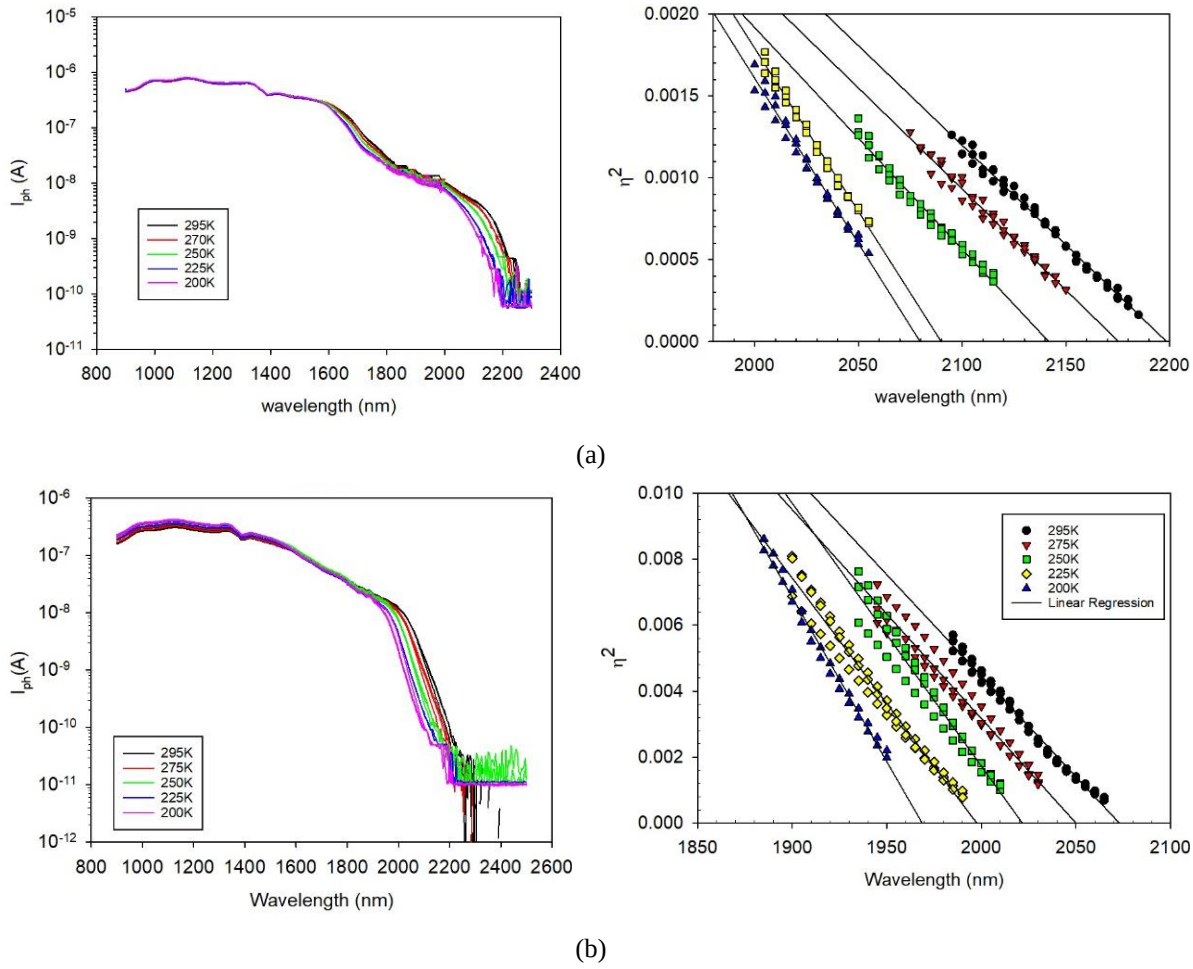

Figure 4.11: Temperature dependence of photocurrent characteristics and extraction of λc using linear regression of η^2 for (a) K466 (at - 7 V) and (b) III-V-5 (at - 6 V) from 295K to 200K.

4.5. Nextnano simulation

Nextnano simulations were completed on nextnano++ versions 4.2.7.9 using single band Kronig-Penney (k.p) theory [10]. Temperature dependence was enabled in all simulations. The full T2SL structure was included in the simulation, rather than relying on periodic boundary conditions. A grid spacing of 0.25 nm was used. A smaller grid spacing was considered, but the effect on λ_c was negligible.

In the simulations, the device structure consists of a 20 nm thick InGaAs layer at either side of the T2SL region, which replaces the entire non-T2SL layers. It was determined through

comparisons that this simplification had no effect on the simulated values of λ_c. Using the default parameter values, temperature dependence of cutoff wavelength for 5.0nm/5.0nm $In_{0.53}Ga_{0.47}As/GaAs_{0.51}Sb_{0.49}$ type-II superlattice were simulated by using nextnano. Figure 4.12 compares the simulation results to experimental results from [2] and [11]. There is a significant offset of ~ 0.6 µm over the temperature range investigated.

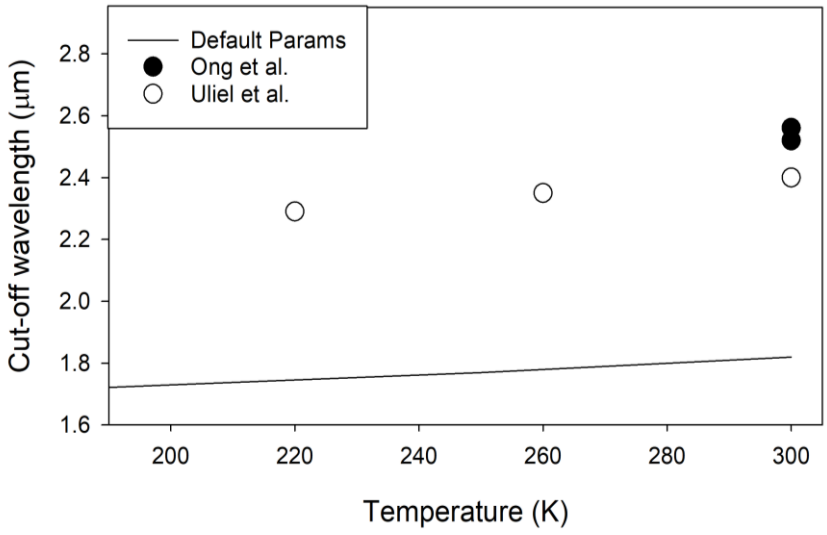

Figure 4.12: Comparison between default nextnano simulation and experimental λ_c values for 5 nm/5 nm InGaAs/GaAsSb type-II superlattice.

Since λ_c values from T2SL structures are heavily influenced by the valance band offset (VBO) between the two constituent materials (InGaAs and GaAsSb), adjusting the VBO value(s) used in the simulations can effectively minimise the discrepancy between experimental simulation and results observed in Figure 4.12. To adjust the VBO value between InGaAs and GaAsSb, nextnano's bowing parameter for calculation of VBO values for GaAsSb (from VBO values of the binary materials, GaAs and GaSb) was adjusted. By modifying the GaAsSb VBO bowing parameter (which was calculated by bowing between the absolute VBOs of GaAs and GaSb.) from its default value of 0 eV to 1.06 eV [12], good agreement between the simulation and validation data for the investigated temperature range was attained, as shown in Figure 4.13. The value of -1.06 eV is within the 1.0 – 1.2 eV range from a number of absorption studies [13]–[15].

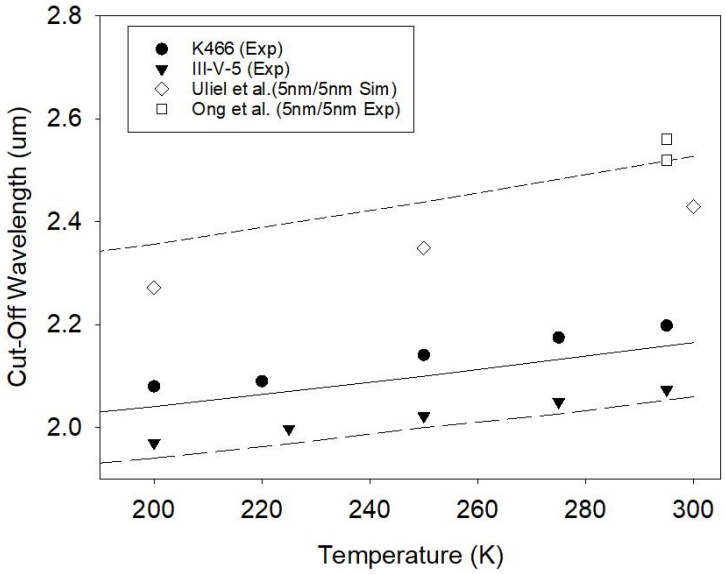

Figure 4.13: Comparison between simulations from this work (lines) using a $GaAs_{1-x}Sb_x$ valence band offset of -1.06 eV, experimental results from this work (closed symbols), experimental results (diamonds [2] and squares [11]).

Validation data consisted of the experimental results for temperature dependence of λ_c from wafers K466 and III-V-5 (earlier in this chapter) as well as those of 5 nm/5 nm $In_{0.53}Ga_{0.47}As/GaAs_{0.51}Sb_{0.49}$ T2SL (lattice-matched to InP substrates) from refs ([2] and [11]). Note that the former group is lattice-matched T2SL whereas the latter group are strained T2SL. Consequently, the validated model for temperature dependence of cutoff wavelength is applicable for both strained and lattice matched T2SL structures.

4.6. Conclusion

I-V, C-V and photoresponse data of two InGaAs/GaAsSb T2SL *p-i-n* photodiodes with strained and lattice-matched $GaAs_{1-x}Sb_x$ (x = 0.4 and 0.49) have been measured. From the literature, dark current density of K466 and III-V-5 are at least ~ one order of magnitude lower than other 5 nm/5 nm InGaAs/GaAsSb T2SL photodiodes, and ~ one order of magnitude higher than values obtained using Rule 07 at a function of temperature from 300 to 180 K. From photoresponse data between room temperature and 200 K, temperature dependence of cut-off wavelength can be determined. By increasing the thicknesses of InGaAs well or GaAsSb barrier, the cut-off wavelengths will be increased. These temperature dependence data were utilised to validate the nextnano model for InGaAs/GaAsSb T2SL. After adjusting the GaAsSb

valence band offset bowing parameter to -1.06 eV, both lattice-matched and strained T2SL show good agreement over the entire temperature range.

4.7. Reference

[1] J. Easley, C. R. Martin, M. H. Ettenberg, and J. Phillips, 'InGaAs/GaAsSb Type-II Superlattices for Short-Wavelength Infrared Detection', *J. Electron. Mater.*, vol. 48, no. 10, pp. 6025–6029, Oct. 2019, doi: 10.1007/s11664-019-07441-x.

[2] Y. Uliel *et al.*, 'InGaAs/GaAsSb Type-II superlattice based photodiodes for short wave infrared detection', *Infrared Phys. Technol.*, vol. 84, pp. 63–71, Aug. 2017, doi: 10.1016/j.infrared.2017.02.003.

[3] B. Chen, W. Y. Jiang, and A. L. Holmes, 'Design of strain compensated InGaAs/GaAsSb type-II quantum well structures for mid-infrared photodiodes', *Opt. Quantum Electron.*, vol. 44, no. 3, pp. 103–109, Jun. 2012, doi: 10.1007/s11082-011-9524-1.

[4] Sergey A. Stepanov, 'X-ray server: an online resource for simulations of x-ray diffraction and scattering', presented at the Proc.SPIE, Oct. 2004, vol. 5536. doi: 10.1117/12.557549.

[5] D. S. G. Ong, J. S. Ng, Y. L. Goh, C. H. Tan, S. Zhang, and J. P. R. David, 'InAlAs Avalanche Photodiode With Type-II Superlattice Absorber for Detection Beyond 2 μm', *IEEE Trans. Electron Devices*, vol. 58, no. 2, pp. 486–489, Feb. 2011, doi: 10.1109/TED.2010.2090352.

[6] P. Bhattacharya and INSPEC (Information service), Eds., *Properties of lattice-matched and strained indium gallium arsenide*. London: INSPEC, Institution of Electrical Engineers, 1993.

[7] R. Sidhu, Ning Duan, J. C. Campbell, and A. L. Holmes, 'A long-wavelength photodiode on InP using lattice-matched GaInAs-GaAsSb type-II quantum wells', *IEEE Photonics Technol. Lett.*, vol. 17, no. 12, pp. 2715–2717, Dec. 2005, doi: 10.1109/LPT.2005.859163.

[8] H. Inada *et al.*, 'Low dark current SWIR photodiode with InGaAs/GaAsSb Type II quantum wells grown on InP substrate', in *2009 IEEE International Conference on Indium Phosphide & Related Materials*, Newport Beach, CA, USA, May 2009, pp. 149–152. doi: 10.1109/ICIPRM.2009.5012464.

[9] H. Inada *et al.*, 'MOVPE grown InGaAs/GaAsSb type II quantum well photodiode for SWIR focal plane array', presented at the SPIE Defense, Security, and Sensing, Orlando, Florida, United States, May 2011, p. 801220. doi: 10.1117/12.888096.

[10] R. De. L. Kronig and W. G. Penny, 'Quantum mechanics of electrons in crystal lattices', *R Soc*, vol. 130, no. 814, p. 15, 1931, doi: 10.1098/rspa.1931.0019.

[11] D. S. G. Ong, J. S. Ng, Y. L. Goh, C. H. Tan, S. Zhang, and J. P. R. David, 'InAlAs Avalanche Photodiode With Type-II Superlattice Absorber for Detection Beyond 2 $\mu\hbox{m}$', *IEEE Trans. Electron Devices*, vol. 58, no. 2, pp. 486–489, Feb. 2011, doi: 10.1109/TED.2010.2090352.

[12] I. Vurgaftman, J. R. Meyer, and L. R. Ram-Mohan, 'Band parameters for III–V compound semiconductors and their alloys', *J. Appl. Phys.*, vol. 89, no. 11, pp. 5815–5875, Jun. 2001, doi: 10.1063/1.1368156.

[13] G. A. Antypas and L. W. James, 'Liquid Epitaxial Growth of GaAsSb and Its Use as a High-Efficiency, Long-Wavelength Threshold Photoemitter', *J. Appl. Phys.*, vol. 41, no. 5, pp. 2165–2171, Apr. 1970, doi: 10.1063/1.1659183.

[14] R. E. Nahory, M. A. Pollack, J. C. DeWinter, and K. M. Williams, 'Growth and properties of liquid-phase epitaxial GaAs $_{1-x}$ Sb $_{x}$', *J. Appl. Phys.*, vol. 48, no. 4, pp. 1607–1614, Apr. 1977, doi: 10.1063/1.323841.

[15] N. N. Sirota and E. E. Matyas, 'Reflection and absorption spectra of GaAsxSb1-x solid solutions', *Phys. Status Solidi A*, vol. 4, no. 2, pp. K143–K146, Feb. 1971, doi: 10.1002/pssa.2210040245.

5. Short-wave Infrared AlInAsSb Photodiodes

By adjusting the compositions, AlInAsSb grown lattice matched to InP, InAs and GaSb substrates can be used as photodiodes or APDs. Alternatively, a SAM-APD can be designed. In a SAM-APD, the absorption and multiplication materials are separated allowing for independent optimization, while also limiting the electric field in the absorber (reducing tunneling currents). A SAM-APD using different AlInAsSb compositions for absorption and multiplication (lattice matched to GaSb) was demonstrated [1].

Previous reports on AlInAsSb lattice matched to GaSb used x = 0.3 - 0.8 [2], [3], and 0.15 [4]. Those with high Al (x) compositions exhibited high avalanche multiplication, low dark currents, and electron dominated impact ionization, which are desirable characteristics for avalanche materials. To achieve λ_c approaching 3 µm, however, a low Al composition is required. There are no experimental avalanche multiplication results for AlInAsSb with low Al compositions, preventing evaluation of (i) its potential as a multiplication material, or (ii) an upper limit of the electric field to prevent undesirable impact ionization if used as the absorber. In this chapter, the first study of avalanche multiplication in random alloy $Al_{0.1}In_{0.9}As_{0.83}Sb_{0.17}$ diodes, which are lattice matched to GaSb substrates and have an expected bandgap of 0.35 eV [5], is presented.

5.1. Device structure of mesa AlInAsSb photodiodes

Four $Al_{0.1}In_{0.9}As_{0.83}Sb_{0.17}$ wafers, SF1436, SF1437, SF1438 and SF1439, were grown using MBE on (100) n^+ GaSb substrates by the National Epitaxy Facility in Sheffield. Their wafer structures are summarised in Table 5.1 and a schematic cross-sectional view of the device is shown in Figure 5.1. All wafers were homojunction *p-i-n* structures and their nominal *i*-layer thicknesses were either 2.0 or 4.0 µm. Doping densities in the *p*- and *n*-AlInAsSb layers adjacent to the i-layer were relatively low (compared to usual *p-i-n* diodes), in an attempt to avoid edge breakdowns in mesa diodes made with narrow bandgap materials [6].

The composition of $Al_{0.1}In_{0.9}As_{0.83}Sb_{0.17}$ was selected to match the bandgap of InAs (0.35 eV), using Equation (1.1). The lattice matching conditions for $Al_xIn_{1-x}As_ySb_{1-y}$ with x = 0.1 on GaSb substrates can be obtained by using the simple expression of $y = \frac{A_0+B_0x}{C_0+D_0x}$, where A_0: 0.3834, B_0: 0.3439, C_0: 0.4211 and D_0: 0.0530 [7]. XRD data supplied by the National Epitaxy Facility

indicate peak split of 0.065˚, 0.055˚, 0.101˚, and 0.08˚, for SF1436, SF1437, SF1438, and SF1439, respectively. X-Ray Server was used to perform the fitting to the XRD experimental data [8]. XRD experimental and fitting data for wafer SF1439 are shown as an example in Figure 5.2. The fitting data suggested that Al fraction varies between 0.093 and 0.104.

Table 5.1: Wafer structures of AlInAsSb wafers SF1436, SF1437, SF1438 and SF1439.

Thickness (nm)	**Material**	**Doping type**	**Doping density (cm^{-3})**
300	$Al_{0.1}In_{0.9}As_{0.83}Sb_{0.17}$	P	2.0E18
200	$Al_{0.1}In_{0.9}As_{0.83}Sb_{0.17}$	P	2.0E17
2000 (SF1436, SF1437, SF1438) or 4000 (SF1439)	$Al_{0.1}$ $In_{0.9}As_{0.83}Sb_{0.17}$	Undoped	N/A
200	$Al_{0.1}$ $In_{0.9}As_{0.83}Sb_{0.17}$	N	2.0E17
500	$Al_{0.1}$ $In_{0.9}As_{0.83}Sb_{0.17}$	N	2.0E18
n-GaSb substrate (doping ~ 5.0E17 cm^{-3})			

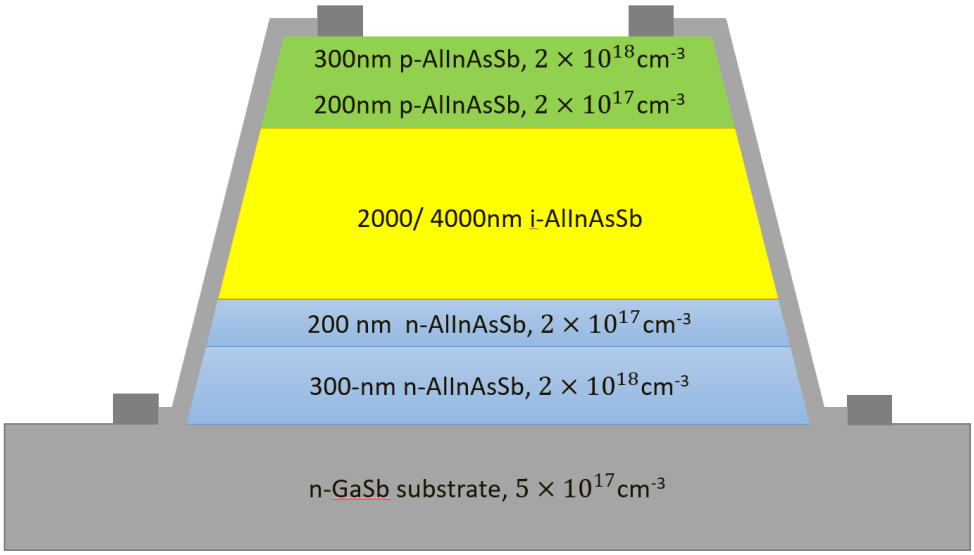

Figure 5.1: Schematic cross-sectional view of the mesa AlInAsSb photodiodes used in this work.

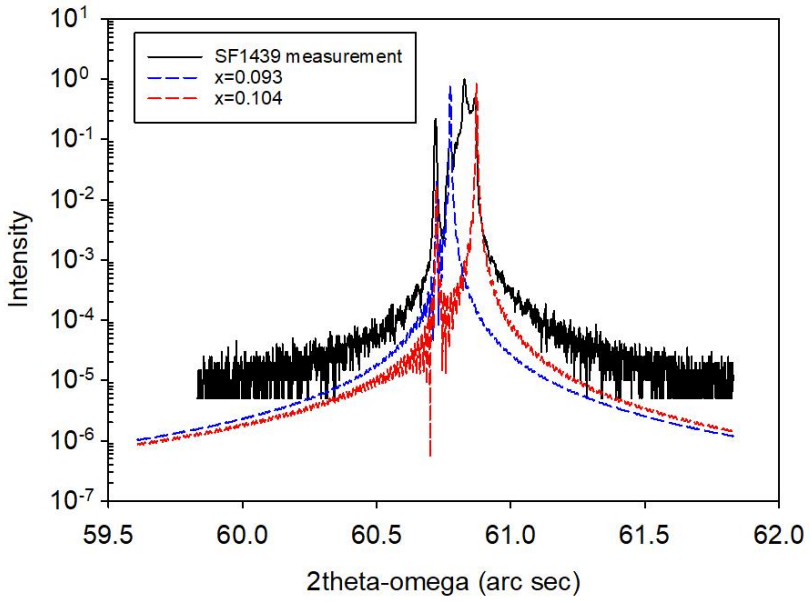

Figure 5.2: Experimental (solid line) XRD characteristics of wafer SF1439 and fitted (dash line) data.

5.2. Device fabrication of AlInAsSb mesa photodiodes

Device fabrications were carried out by Dr. Leh Woon Lim and Dr. Jonathan D. Petticrew at the University of Sheffield. Circular mesa diodes with 420, 220, 120 and 70 µm in diameter were fabricated using standard UV photolithography (NEWPIN mask set) and wet chemical etching. For each fabrication run, two etchants were used to create the mesas. The first, main etchant was a solution of phosphoric acid: hydrogen peroxide: de-ionised water (H_3PO_4: H_2O_2: H_2O) in a ratio of 1:1:1. Different solutions/ratios were trialed as additional etchant in devices fabrication runs (details later), due to an initial lack of direct experience with wet chemical etching of AlInAsSb. For all runs, Ti/Au (20/200 nm) were deposited as the *p*- and *n*-contacts via electron-beam evaporation.

All samples were passivated with negative photoresist SU-8 in the final fabrication processing step to preserve the surface conditions. Compared to SiO_2 or SiN_x, SU-8 is considered as a more appropriate passivation material for narrow bandgap materials and has been used extensively to passivate InAs photodiodes [9]. This is because of much lower processing temperatures required for SU-8 (< 100 °C) compared to those used in standard dielectric depositions (>150 °C).

The finishing etchants (for 30 seconds) with the associated ratios trialled included are: (A) H_3SO_4: H_2O_2: H_2O (1:8:80), (B) HCl: H_2O_2: H_2O (1:1:5) and (C) HCl: H_2O (1:5). These

resulted in different combinations summarised in Table 5.2. The H_3SO_4 solution was trialled because it is used as a finishing etchant for InAs, in combination with H_3PO_4: H_2O_2: H_2O (1:1:1) [10]. Following device fabrication, room temperature I-V characteristics of different-sized devices from the samples were obtained. Samples that suffered catastrophic failures during I-V measurement or did not exhibit I-V diode characteristics were considered as having poor I-V characteristics.

Samples with poor I-V characteristics (i.e. inconsistent data from same-sized devices for a given sample) are dominated by those using only etchant A or B as the additional etchant and they are shaded in Table 5.2. For the remaining samples, they all exhibited extremely poor I-V characteristics unless etchant C was used, as shown in Figure 5.3. HCL may have removed the surface oxidation left from etchants A or B, smoothing the surface sidewalls and yielding more consistent I-V characteristics. However, even in the 'best' samples, some surface leakage currents were present, based on comparison of dark current densities from different sized devices. Samples which used etchant C remained stable for period of weeks to months.

When etchant A was avoided and etchant C was used, there were no significant difference in the I-V data whether etchant B was used, as shown in Figure 5.4.

*Table 5.2: Etchants used in device fabrication of the AlInAsSb mesa photodiodes. Samples marked with * were used for subsequent measurements.*

Wafer no.	**Sample name**	**Etchant**				**Etch depth (µm)**	**I-V quality**
		H_3PO_4: H_2O_2: H_2O (1:1:1)	**(A) H_3S0_4: H_2O_2: H_2O (1:8:80)**	**(B) HCl: H_2O_2: H_2O (1:1:5)**	**(C) HCl (1:5) clean**		
SF1436	191020	✓	✓			3	Poor
SF1437	191020	✓	✓			3.2	Poor
	101120-1	✓			✓	3.4	Good
	101120-2	✓		✓	✓	4.4	Good
SF1438	201020	✓	✓			3.1-3.2	Poor
	111120 *	✓		✓	✓	3	Good
SF1439	201020	✓				4.9	Poor
	101120-1	✓			✓	4.6	Good
	101120-2	✓		✓	✓	5.2	Good
	111120	✓		✓	✓	5.4	Good
	170521-A	✓		✓	✓	4.7	Poor (metal)
	170521-B*	✓		✓	✓	4.8	Good

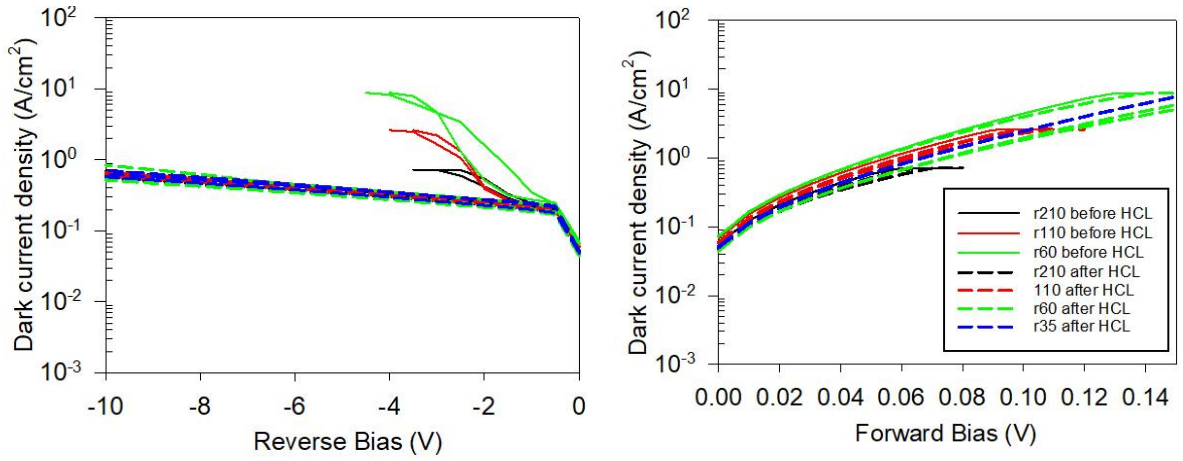

Figure 5.3: Comparisons of room temperature dark current densities of SF1439 mesa diodes before and after using etchant (C).

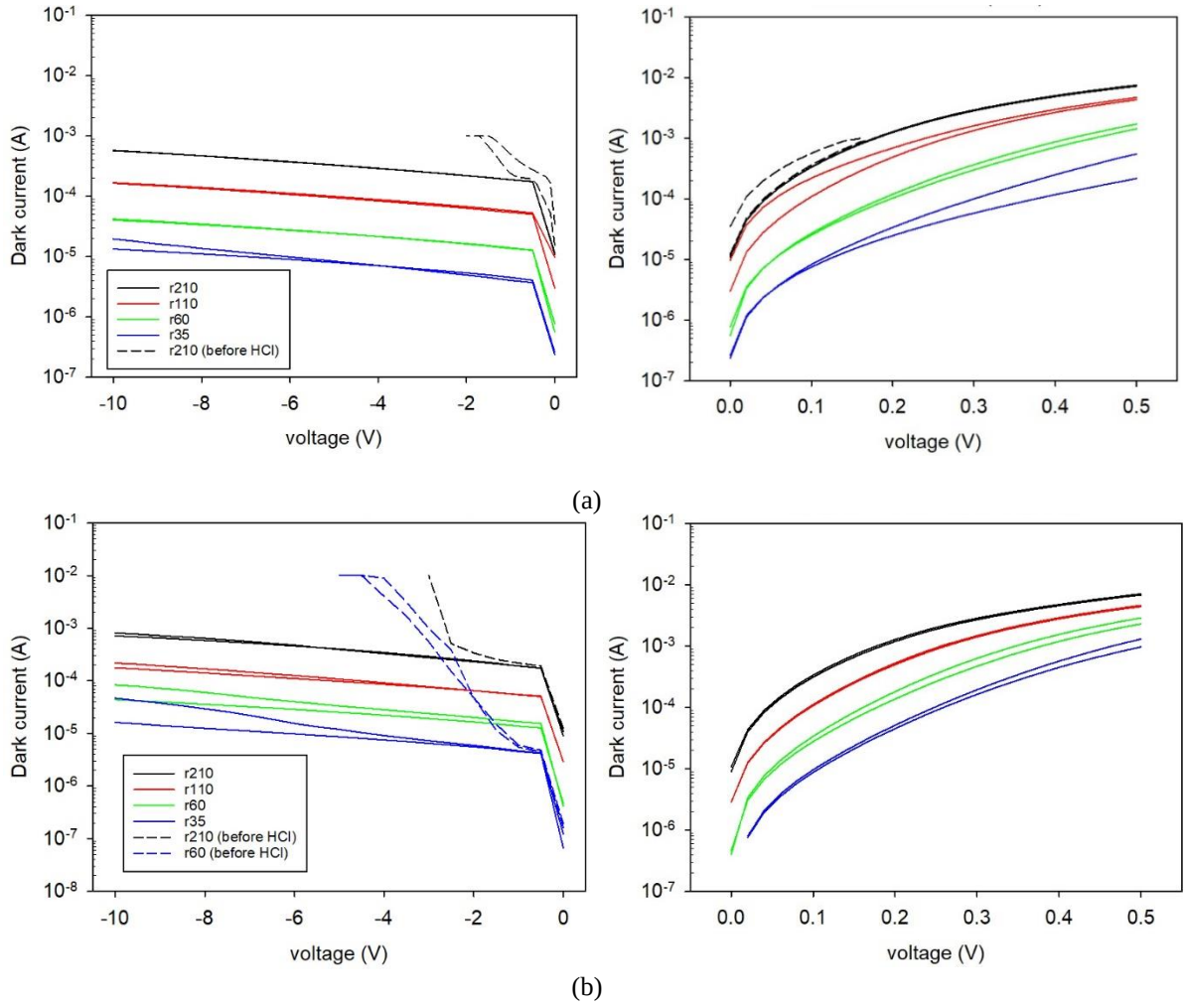

Figure 5.4: Room temperature I-Vs of SF1437 mesa diodes fabricated (a) without or (b) with etchant (B). These data were obtained from sample SF1437-101120-1 and sample SF1437-101120-2, respectively.

Wafers SF1436 and SF1437 have identical structures as wafer SF1438, but Nomarski microscopy revealed that they have more growth defects (Figure 5.5). Hence subsequent results

in this chapter are from wafers SF1438 and SF1439. The samples used are marked with asterisks in Table 5.2.

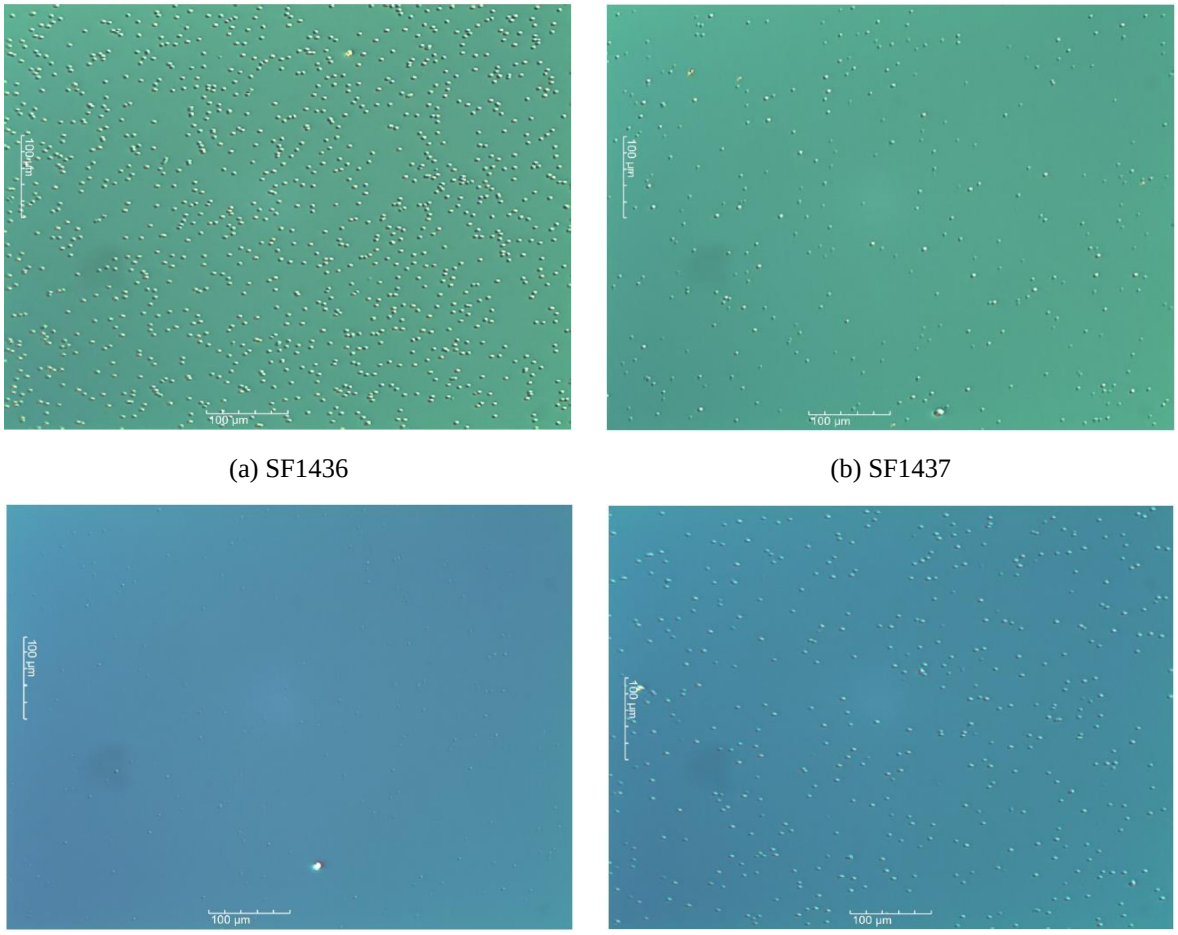

(a) SF1436 (b) SF1437

(c) SF1438 (d) SF1439

Figure 5.5: Surface images of the AlInAsSb wafers from Nomarski microscopy.

5.3. Low temperature Capacitance-Voltage measurements

C-V measurements were performed on the samples to extract doping profiles. The C-V characteristics of *p-i-n* diodes with 420, 220 and 120 µm in diameter from SF1438 and SF1439 at 200 K are shown in Figure 5.6. The C-V profiles of the diodes were found to scale well with device area without any radius correction, verifying the diodes are properly isolated.

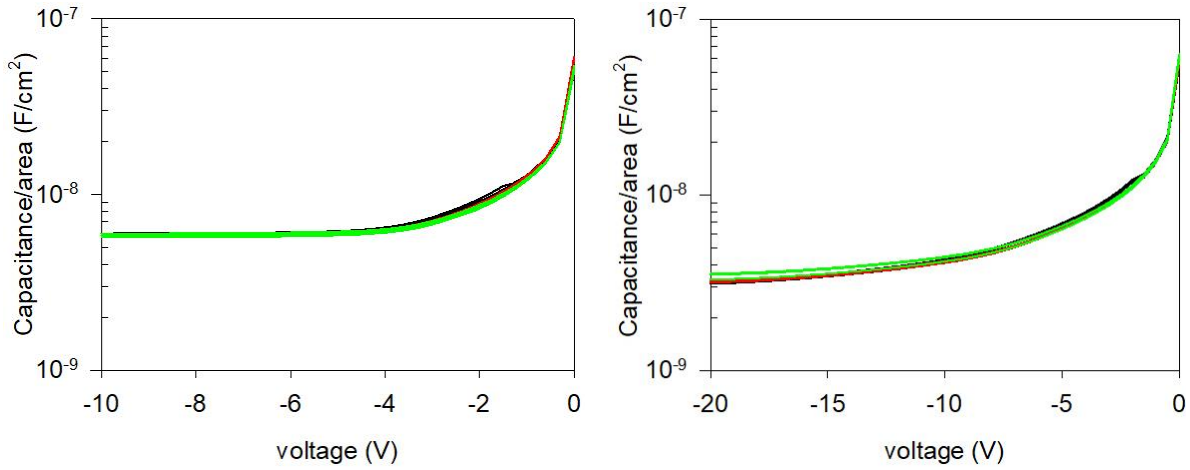

Figure 5.6: C-V characteristics of p-i-n diodes with 420, 220 and 120 µm diameter from (a) SF1438 and (b) SF1439. The data are presented as capacitance density.

Assuming 3-region abrupt doping profiles, a built-in voltage of 0.1 V and a dielectric constant of 14.65, C-V fitting was performed. Comparisons between the C-V data and the fittings for both wafers are shown in Figure 5.7.

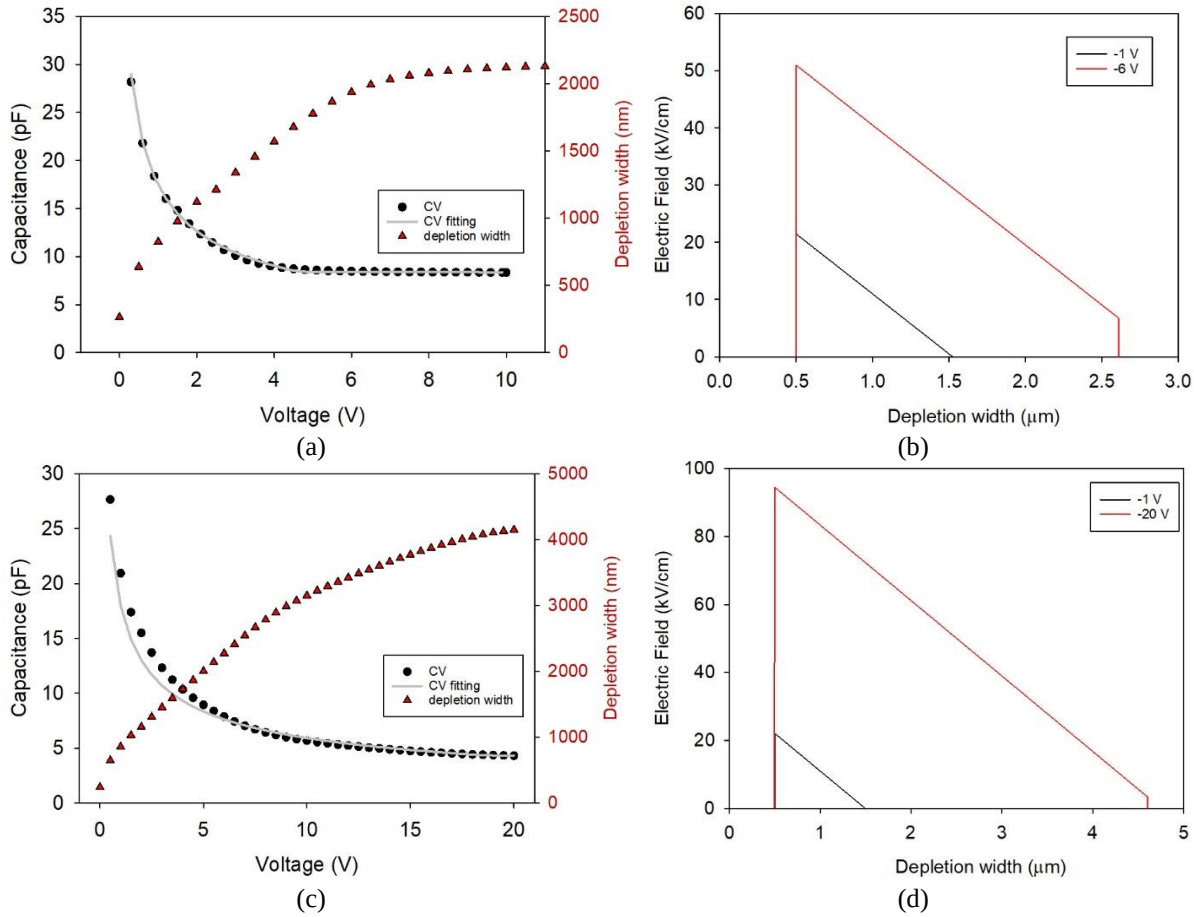

Figure 5.7: Reversed C-V data (black circles, left axis) and fitting (lines, left axis) for (a) wafer SF1438 and (c) wafer SF1439. The results are for 420 µm diameter devices. The total depletion widths are shown in the right axes. Electric field profiles as functions of reverse bias for (b) wafer SF1438 and (d) wafer SF1439.

The extracted doping profiles are summarised in

Table 5.3 The estimated *i*-layer thicknesses are 2.11 and 4.1 µm, for wafer SF1438 and SF1429, respectively. These are ~5 % thicker than the intended values but they do not prevent subsequent measurements. The corresponding unintentional doping densities are ~ 1.7×10^{15} and 1.8×10^{15} cm^{-3}, which are low given the material's narrow bandgap.

The dielectric constant of $Al_{0.1}In_{0.9}As_{0.83}Sb_{0.17}$ was obtained from linear interpolation between the four binary materials that make up AlInAsSb. Consider a quaternary material $A_xB_{1-x}C_yD_{1-y}$ made up of four binary materials: AC, AD, BC, and BD. Applying linear interpolation, the quaternary material's parameter Q is given by

$$Q(x,y) = xyB_{AC} + x(1-y)B_{AD} + (1-x)yB_{BC} + (1-x)(1-y)B_{BD}\ . \qquad [7]$$

Substituting dielectric constants of InAs, InSb, AlSb, and AlAs (14.6 [11], 17.7 [12], 12.04 [13], and 10.06 [14], respectively) into Equation 5.8 yielded a final value of 14.65.

Using the extracted doping profiles, electric field profiles as functions of reverse bias were calculated for the wafers. SF1438 and SF1439 would be fully depleted at ~ - 6 V and - 20 V, respectively, as shown in Figure 5.7 (b) and (d).

Table 5.3: Doping profiles used in C-V fittings of wafer SF1438 and SF1439, assuming built-in voltage of 0.1 V and dielectric constant of 14.65.

Layer thickness used in C-V fitting (nm)	**Doping level (cm^{-3})**
500	+1.5E18
2110 (SF1438) 4100 (SF1439)	-1.7E15 (SF1438) -1.8E15 (SF1439)
700	-1.5E18

5.4. Temperature dependence of dark current

Dark I-V measurements at temperatures from 295 to 80 K were performed using diodes with diameters of 120, 220 and 420 µm placed in a low-temperature probe station. The data are presented as dark current densities in Figure 5.8. For temperature ≥ 200 K, dark current

densities from the different-sized devices are in agreement, indicating that dark currents at these temperatures are dominated by bulk leakage mechanism(s). For a given temperature, the dark current densities increase rapidly with reverse bias for bias beyond ~15 to 17 V (temperature dependent). This is attributed to band-to-band tunnelling current (details later).

To compare with InAs diodes [15], [16], mean dark current densities from only the 420 µm diameter diodes on both wafers are plotted as functions of temperature in Figure 5.9. Values of J_{dark} at – 0.5 V from these AlInAsSb photodiodes are similar to the best value from InAs mesa diodes [15].

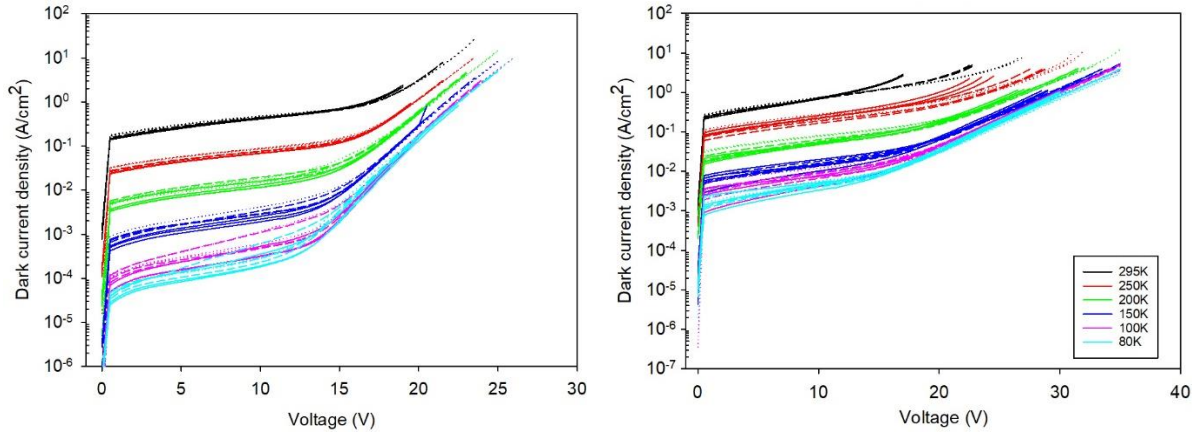

Figure 5.8: Reverse dark current density data of wafers (a) SF1438 and (b) SF1439 at 295 to 80 K. Data are from devices with diameter of 420, 220 and 120 µm.

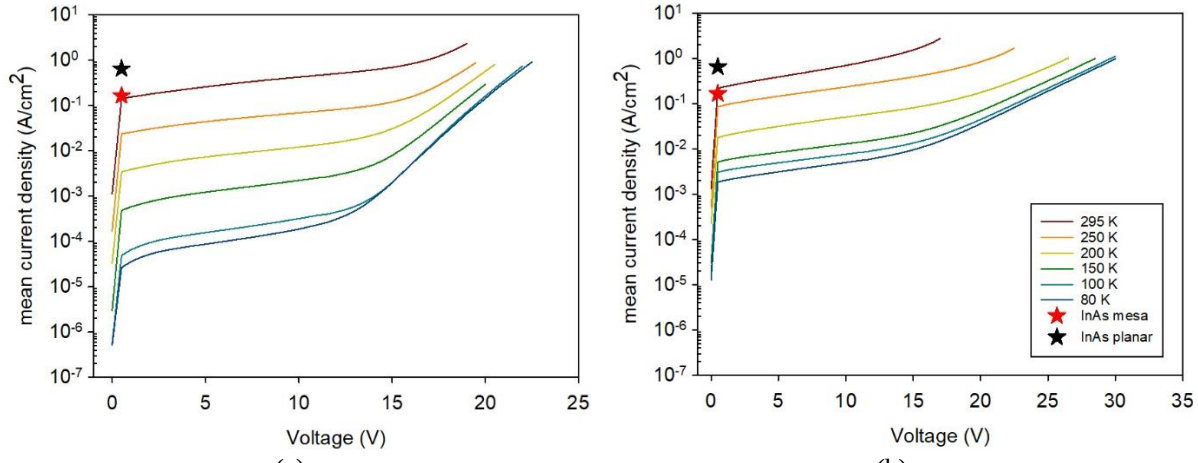

Figure 5.9: Mean J-V characteristics of 420 µm diameter devices for (a) SF1438 and (b) SF1439 at 295 to 80 K. J_{dark} at -0.5 V and 300 K for mesa [15] and planar InAs APDs [16] are included for comparison.

Further dark current analyses were carried out to estimate the values of J_{bulk} and J_{surf} over the range of bias. For a given reverse bias and temperature, the dark current data were plotted

against the device radius and fitted with Equation (3.8). Example data and fitting for devices with different radii on wafer SF1438 (at 295 K and - 0.5 V) is shown in Figure 5.10, with the fitted J_{bulk} = 134.1 mA/cm^2 and J_{surf} = 100 µA/cm.

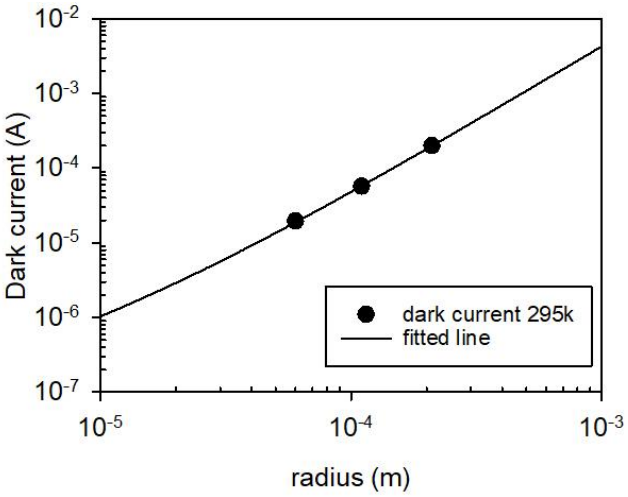

Figure 5.10: Example dark current data and fitting (SF1438 at T = 295 K and V_b = 0.5 V) to estimate J_{bulk} and J_{surf}.

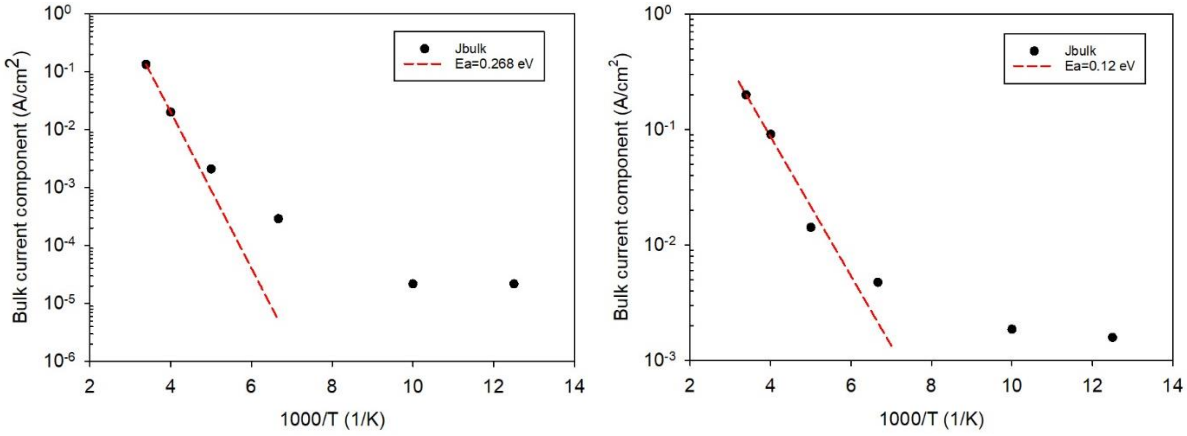

(a) (b)

Figure 5.11: Arrhenius plots of the estimated bulk leakage currents from (a) samples SF1438 and (b) SF1439.

Dark current analyses to estimate the values of J_{bulk} and J_{surf} were repeated over for data obtained at 295 to 80 K, yielding J_{bulk} as functions of temperature. Values of J_{bulk} at -0.5 V are plotted inverse temperature for both wafers in in Figure 5.11. Fittings using the Arrhenius equation, $J_{bulk}(T) = \forall \exp\left(-\frac{E_a}{kT}\right)$, where E_a is the activation energy of bulk dark current density, are also shown. Due to insufficient shielding from blackbody radiation within the low temperature probe station, dark current data at T < 200 K contain background-induced photocurrent (see section 5.6) so are excluded from the Arrhenius fittings. Activation energy

values within the temperature range of 295 to 200 K are 0.268 and 0.12 eV for SF1438 and SF1439, respectively. The value for SF1438 is close to the expected room temperature bandgap of AlInAsSb, indicating minority diffusion current is a dominant mechanism. The value for SF1439 is significantly lower, indicating that carrier recombination is a dominant mechanism. This could be caused by a higher level of wafer defects in SF1439 compared to SF1438 (Figure 5.5).

5.4.1. Tunnelling current fitting

To evaluate if the rapid increase in dark current density at high reverse bias observed is caused by band-to-band tunnelling currents, data fittings were carried out using Equation (3.6). Since this rapid increase is more obvious at lower temperatures, the focus was on data obtained at 200 K or below. Using parameter values summarised in Table 5.4, the 200 K data and fittings are in broad agreement, as shown in Figure 5.12. This confirms that tunnelling current is the dominant leakage mechanism at high reverse bias (above -22 V and -30 V for wafer SF1438 and SF1439, respectively). Additional fittings carried out for 150 K data are also shown in Figure 5.12.

Tunnelling current has a weak temperature dependence via the temperature dependence of bandgap. As temperature decrease, the material's bandgap increases, which reduces tunnelling current for a given reverse bias. The λ_c, which is taken at the 50 % of the peak response, at 200 and 150 K were determined from the spectral responses (Appendix B).

Table 5.4: Parameters used for tunnelling current fitting at 200 and 150 K.

Parameters	**Values (SF1438)**		**Values (SF1439)**	
Temperature	**200 K**	**150 K**	**200 K**	**150 K**
Electron charge, q	1.60×10^{-19} C		1.60×10^{-19} C	
Planck's constant, h	6.63×10^{-34} C		6.63×10^{-34} C	
Electron effective mass, m_e	$0.04\times9.11\times10^{-31}$ kg		$0.04\times9.11\times10^{-31}$ kg	
Bandgap, E_g	0.43 eV	0.45 eV	0.43 eV	0.45 eV
Built-in voltage, V_{bi}	0.1 V		0.1 V	
Electric field, E	From CV fitting		From CV fitting	
Junction area, A	πr^2		πr^2	
Tunnelling fitting parameter, σ_{tun}	1.5	1.42	1.1	1.05

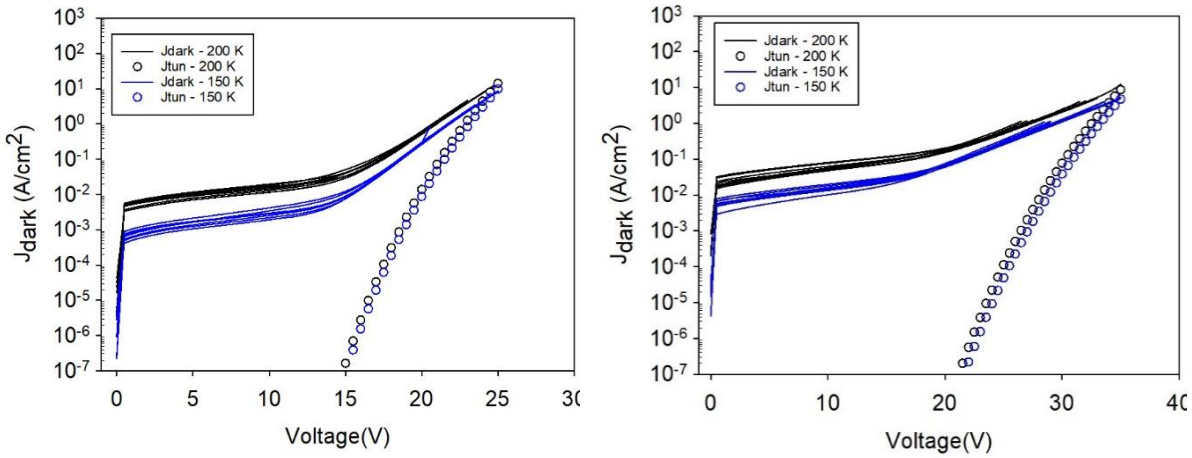

Figure 5.12: Dark current density data (line) and tunnelling fittings (open circle) for (a) SF1438 and (b) SF1438 at 200 K and 150 K.

5.5. Low temperature avalanche gain

To establish the relationship between electron and hole impact ionisation coefficients, the type of unintentional doping in the i-InAlAsSb layer must be determined. This is important because the doping type affects the expected rate of increase in photocurrent with reverse bias one can expect to result from carrier collection efficiency improving with reverse bias. If the i-InAlAsSb layer is n-type, then the depletion region begins at the p/I junction (close to the wafer top surface, which is also where carriers will be generated through photon absorption) and photocurrent increase with reverse bias should be small. In contrast, if the i-InAlAsSb layer is p-type, then the depletion region begins at the i/n junction (far from the photon absorption locations). Then photocurrent may increase significantly with reverse bias due to improved carrier collection efficiency.

This crucial check was carried out on an additional pair of SF1438 and SF1439 samples containing partially etched diodes, which are depicted schematically in contrast with the usual fully etched diodes in Figure 5.13. Room temperature J_{dark} of partially etched diodes (420, 220 and 120 µm diameter) are compared with those of fully etched diodes for both wafers in Figure 5.14. For a given wafer, there is no noticeable difference within the voltage range, indicating that the partially etched diodes had sufficient electrical isolation from each other. This is only possible if the i-InAlAsSb layers in both wafers are *n*-type.

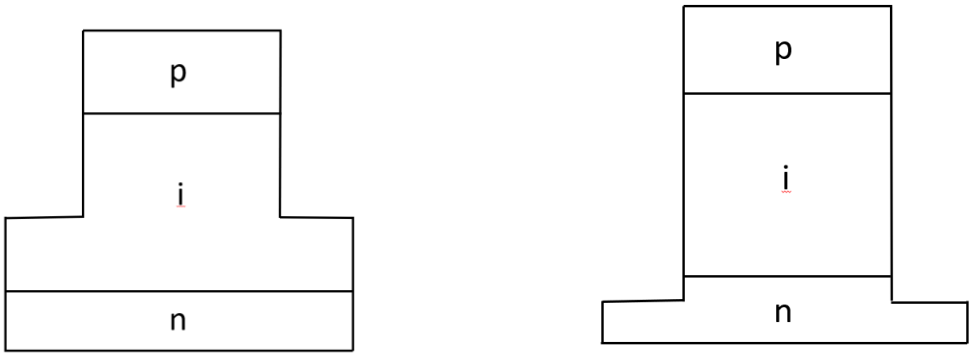

Figure 5.13: cross-sectional schematic diagrams of partial and fully etched diodes.

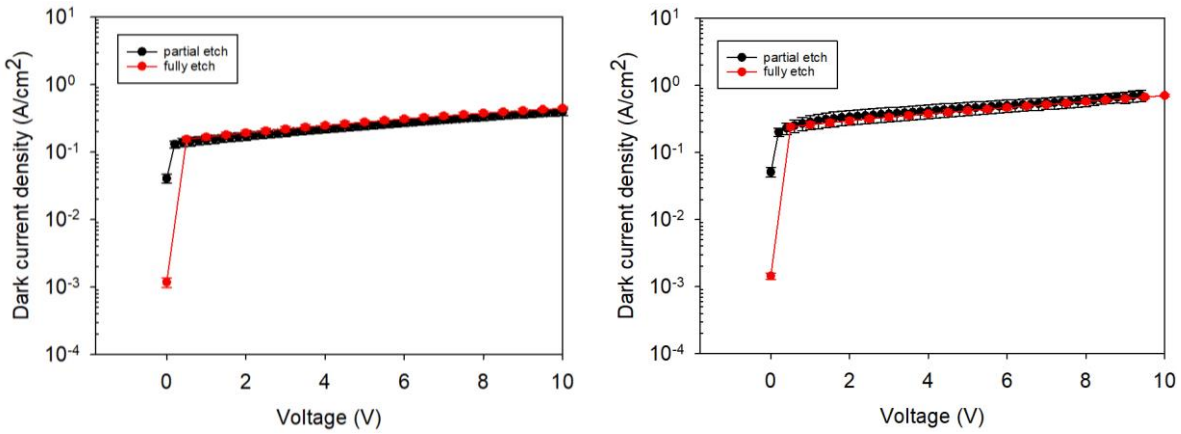

(a) (b)

Figure 5.14: Room temperature dark current densities of devices from partially etched sample and fully etched sample for wafers (a) SF1438 and (b) SF1439.

Further C-V data support this observation. Forward C-V characteristics of devices with 420 and 220 µm diameter from fully and partially etched samples are compared in Figure 5.15. Again, there is no significant differences for a given device diameter and wafer, indicating sufficient electrical isolation between the devices from the partially etched samples. Having established that the i-InAlAsSb layers in both wafers are *n*-type, it is expected that any significant increase in photocurrent with reverse bias beyond a very small reverse bias (around -0.5 V) can be attributed to impact ionisation.

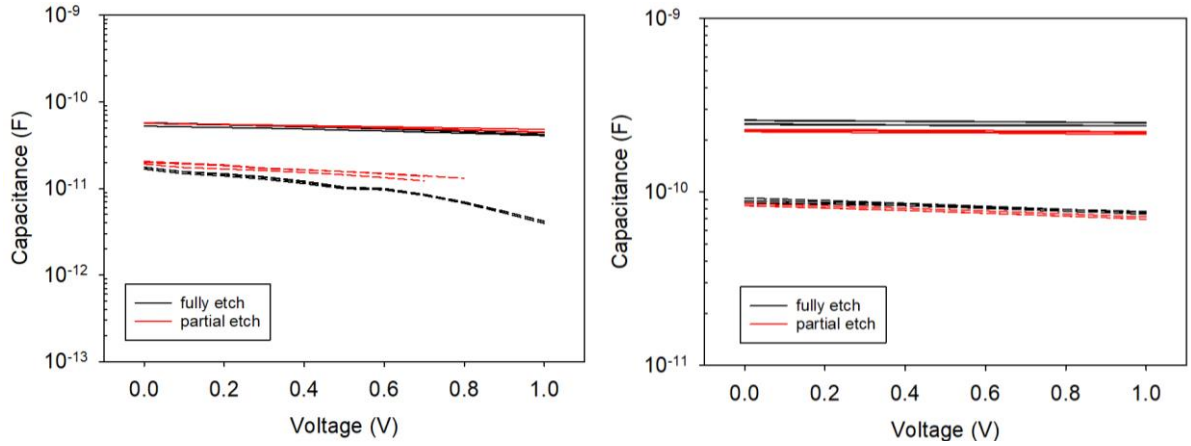

Figure 5.15: Room temperature forward C-V characteristics of devices with 420 and 220 µm diameter for wafers (a) SF1438 and (b) SF1439.

Due to relatively high dark currents at room temperature, the *M*(*V*) measurements were performed on cooled devices at temperatures of 200, 150 and 80 K using a Janis low temperature probe station. The full etched samples were used for these measurements and device diameter used was limited to 220 µm (a result of balancing the needs of the minimising dark current and maximising optical window area).

Phase-sensitive detection of photocurrent was implemented with a lock-in amplifier and an internally/ externally modulated laser to further improve the data robustness. The device was reverse-biased using a source-measure-unit via a 1k Ω series resistor. *M*(*V*) measurements were repeated for 3 lasers chosen to produce different carrier injection profiles, as summarised in Table 5.5. Laser 1 with 633 nm wavelength provided *M(V)* resulting from pure electron injection photocurrent measurements. At this wavelength, ~ 99 % of the incident photons will be absorbed within the top 380 - 400 nm of the device, i.e. outside the depletion regions. This was estimated using absorption coefficients for AlInAsSb with x = 0.15 [4] and InAs [17], due to a lack of absorption coefficients for AlInAsSb with x = 0.10.

Table 5.5: 3 lasers chosen to produce different carrier injection profiles.

Laser number	**Laser wavelength (nm)**	**Carrier injection profile**	**Multiplication factor**
1	633	Pure electron	M_e
2	1550	Mixed (with a lower proportion of holes than in laser 3)	M_{mix1}
3	2004	Mixed (with a higher proportion of holes than in laser 2)	M_{mix2}

Laser 1 was an internally modulated (370 Hz) semiconductor laser, whereas Laser 2 and 3 were continuous-wave so they required a mechanical chopper (180 Hz) placed in the laser beam path to modulate the light. Light from the laser delivered into the low temperature probe station through a single mode fibre, so that the laser spot could be positioned within the optical window of the devices to produce pure electron and mixed carrier injection profiles. Photocurrent was measured via the voltage drop across the series resistor as a function of reverse bias. Using -0.5 V as the unity gain point, $M(V)$ data were obtained from the photocurrent data.

For a given wafer, temperature and laser, $M(V)$ data were obtained from five devices. These data are presented as mean and standard deviation in Figure 5.16. For given reverse bias and temperature, the avalanche gain factors decrease as the proportion of hole in the carrier injection profile increases (from M_e through M_{mix1} to M_{mix2}). Identical observation can be made from the 3 temperature points covered on both wafers. The data show that in this material electrons impact ionise more readily than holes so $\alpha > \beta$.

As temperature decreases, the avalanche gain decreases slightly (shown in Figure 5.16 (a), (b), and (c)). This indicates that the avalanche gain and hence the ionisation coefficients have a positive dependence on temperatures. This is in line with the temperature dependence of InAs [17], as shown in Figure 5.17. The gain at a given bias is higher by applying a thicker avalanche region [18]. These trends are similar to those reported for InAs APDs [17], [19]. At 200K, as reverse voltage increases, the avalanche gain data were affected by increasing voltage drop across the series resistor used in the measurement setup. For example, a leakage current of 10 µA at 0.5 V would give rise to a voltage drop of 10 mV across the 1 kΩ resistor, reducing actual voltage drop across the AlInAsSb diode. This causes the avalanche gain readings to be lower than their true values. The use of phase-sensitive detection technique only helps in recovering the modulated photocurrent signal and does not alleviate the voltage drop issue caused by the high dark currents.

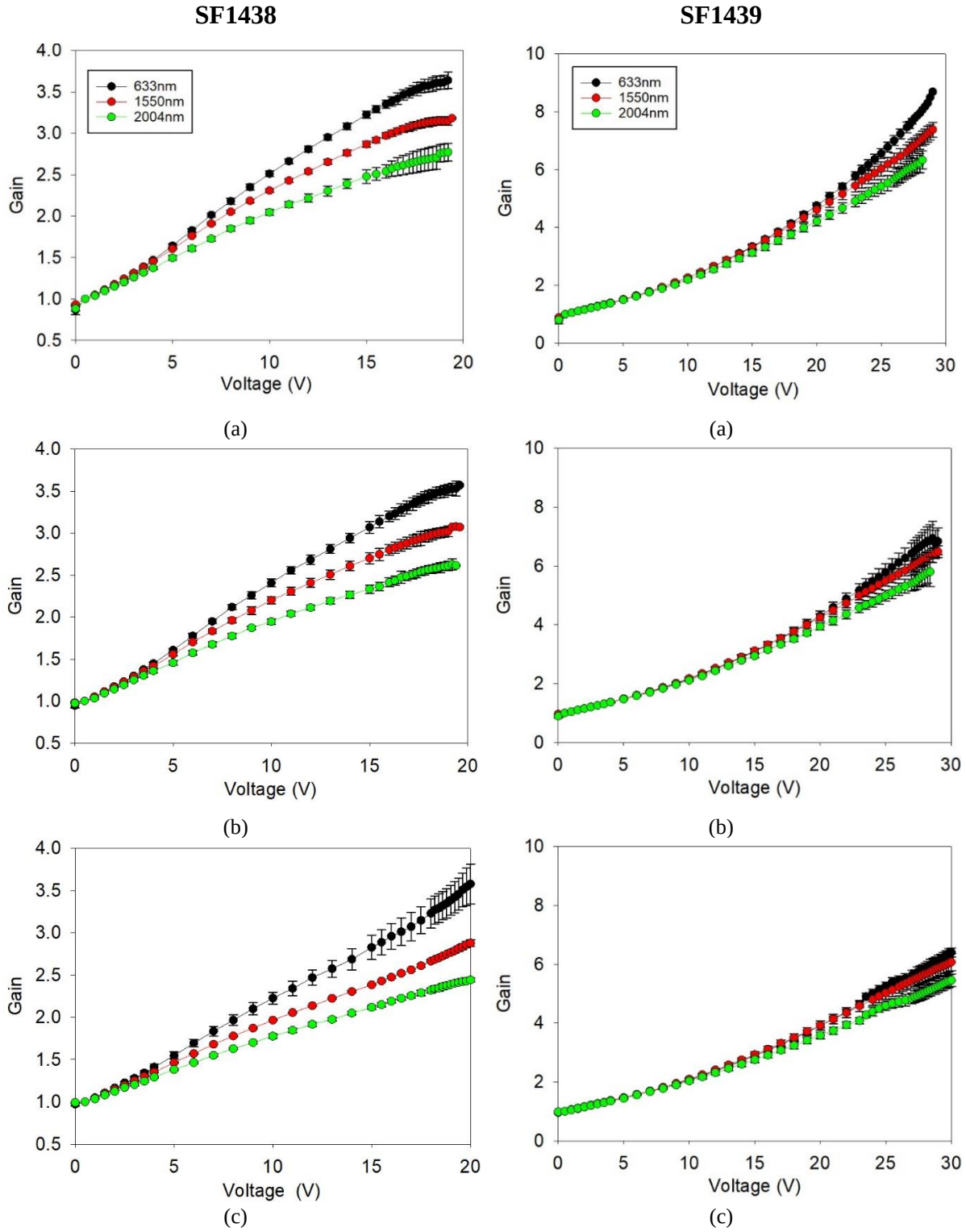

Figure 5.16: Avalanche gain data using 633, 1550 and 2004 nm lasers on SF1438(left) and SF1439 (right) at (a) 200, (b) 150 and (c) 80 K.

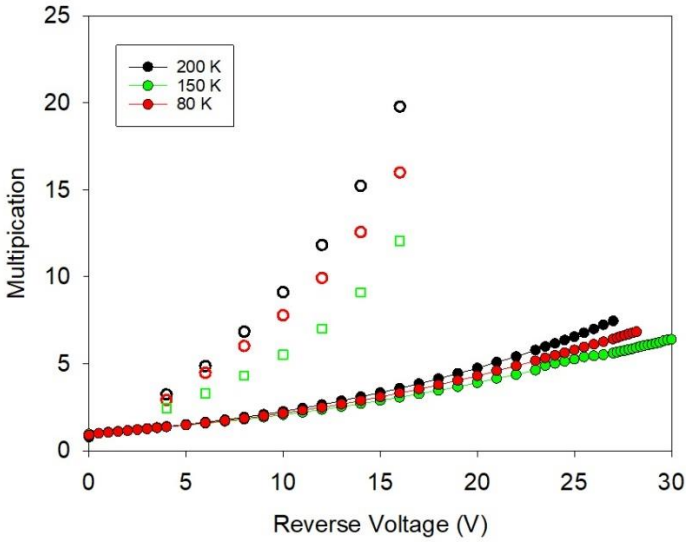

Figure 5.17: The comparisons of avalanche gain data between SF1439 (closed symbols) and InAs eAPDs (opened symbols) [17] by using 633 nm laser at 200, 150 and 80 K.

Impact ionization coefficient for electrons, α, is much larger than that for holes, β, in InAs and the gradually rising gain presented in Figure 5.16 shows the same trends [21]. This gradually rising gain is indicative of a single carrier impact ionization process as two carrier impact ionization has a much sharper rise. α much larger than β has also been observed in digital AlInAsSb with x = 0.7 [20] and 0.8 [3]. Assuming $\beta = 0$ and $\alpha = \beta$, α of samples SF1438 and SF1439 can be estimated from $\alpha(E(V)) = \frac{1}{w}\ln(M)$ and $\alpha(E(V)) = \frac{1}{w}\frac{M-1}{M}$, respectively, where *W* and *E(V)* are the voltage dependent depletion width and electric field calculated from the *C-V* fitting data using an ideal *p-i-n* diode structure assumption. The estimated *α(E)* was then empirically fitted using the expression $\alpha(E) = A\exp\left(-\frac{B}{|E|}^{C}\right)$, where A, B and C are constants whose values are shown in Table 5.6 for 80, 150 and 200 K. Values of α at 200 K estimated using these assumptions and M(V) data of of SF1438 and SF1439 are shown in Figure 5.18. These values are similar to reported data of InAs at 200 K [21].

Table 5.6. Estimated electron ionization coefficients at 80, 150, and 200 K.

Temperature (K)	A (10^5 V/m)	B (10^6 V/m)	C
200	8.77	3.4	0.94
150	8.6	3.45	0.91
80	7.71	3.74	0.87

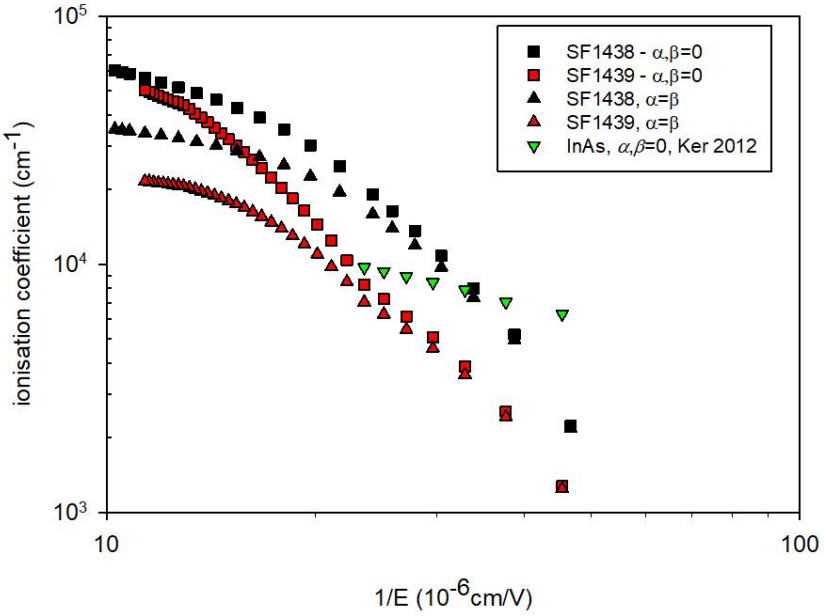

Figure 5.18: Comparison of alpha from SF1438 and SF1429, and InAs at 200 K.

A commercial photodiode FD05D with known responsivity versus wavelength characteristic was used to obtain the system response. At – 1 V and – 6 V bias, the 200 K responsivity of wafers SF1438 and SF1439 at 1550 and 2004 nm wavelengths are summarised in Table 5.7. Compared to the responsivity of InAs APDs without depositing antireflection coating (0.62 A/W at – 0.3 V [16], $\lambda_c \sim 3.5$ µm), the responsivity results are slightly higher.

Table 5.7: Responsivity at 200K for SF1438 and SF1439.

Wafers		**Responsivity (A/W)**	
		1550 nm laser	**2004 nm laser**
SF1438	- 1 V	1.635	1.04
	- 6 V	2.7465	1.649
SF1439	- 1 V	1.59	1.08
	- 10 V	3.617	2.41

5.6. Conclusion

The temperature dependence of dark current, capacitance, and avalanche gain results of AlInAsSb photodiodes with bandgap ~ 0.4 eV were presented from the devices with 2 and 4 µm nominal intrinsic region widths. Experimental results at temperatures ranging from 295 to 77 K showed that the dark currents of both photodiodes were significantly reduced with

decreasing the temperature. The room temperature dark currents were bulk-dominated and compared well against optimized planar InAs APDs operating at similar wavelength. Band-to-band tunnelling currents were observed in the narrow bandgap AlInAsSb photodiodes at high electric field. Using three laser wavelengths to produce three carrier injection profiles, extensive avalanche gain data were obtained at three temperatures (200 – 80 K). The data show that electron ionisation coefficient, α, is larger than hole ionisation coefficient, β. $Al_{0.1}In_{0.9}As_{0.83}Sb_{0.17}$ is not an appropriate avalanche material but can be used as the absorber material in SWIR SAM-APDs.

5.7. References

[1] A. H. Jones, S. D. March, S. R. Bank, and J. C. Campbell, 'Low-noise high-temperature AlInAsSb/GaSb avalanche photodiodes for 2-μm applications', *Nat. Photonics*, vol. 14, no. 9, pp. 559–563, Sep. 2020, doi: 10.1038/s41566-020-0637-6.

[2] M. Ren, S. J. Maddox, M. E. Woodson, Y. Chen, S. R. Bank, and J. C. Campbell, 'Characteristics of AlxIn1-xAs ySb1-y (x:0.3-0.7) Avalanche Photodiodes', *J. Light. Technol.*, vol. 35, no. 12, pp. 2380–2384, Jun. 2017, doi: 10.1109/JLT.2017.2681041.

[3] A. H. Jones, A.-K. Rockwell, S. D. March, Y. Yuan, S. R. Bank, and J. C. Campbell, 'High Gain, Low Dark Current $Al_{0.8}In_{0.2}As_{0.23}Sb_{0.77}$ Avalanche Photodiodes', *IEEE Photonics Technol. Lett.*, vol. 31, no. 24, pp. 1948–1951, Dec. 2019, doi: 10.1109/LPT.2019.2950616.

[4] A. A. Dadey *et al.*, 'Narrow bandgap $Al_{0.15}In_{0.85}As_{0.77}Sb_{0.23}$ for mid-infrared photodetectors', *Opt. Express*, vol. 30, no. 15, p. 27285, Jul. 2022, doi: 10.1364/OE.461854.

[5] S. J. Maddox, S. D. March, and S. R. Bank, 'Broadly Tunable AlInAsSb Digital Alloys Grown on GaSb', *Cryst. Growth Des.*, vol. 16, no. 7, pp. 3582–3586, Jul. 2016, doi: 10.1021/acs.cgd.5b01515.

[6] B. S. White, I. C. Sandall, J. P. R. David, and Chee Hing Tan, 'InAs Diodes Fabricated Using Be Ion Implantation', *IEEE Trans. Electron Devices*, vol. 62, no. 9, pp. 2928–2932, Sep. 2015, doi: 10.1109/TED.2015.2456434.

[7] S. Adachi, *Properties of semiconductor alloys: group-IV, III-V and II-VI semiconductors*. Chichester, U.K: Wiley, 2009.

[8] Sergey A. Stepanov, 'X-ray server: an online resource for simulations of x-ray diffraction and scattering', presented at the Proc.SPIE, Oct. 2004, vol. 5536. doi: 10.1117/12.557549.

[9] P. J. Ker, A. R. J. Marshall, C. H. Tan, and J. P. R. David, 'Surface passivation of InAs avalanche photodiodes for low-noise infrared imaging', in *2016 IEEE 6th International Conference on Photonics (ICP)*, Kuching, Sarawak, Malaysia, Mar. 2016, pp. 1–3. doi: 10.1109/ICP.2016.7510018.

[10] A. R. J. Marshall, C. H. Tan, J. P. R. David, J. S. Ng, and M. Hopkinson, 'Fabrication of InAs photodiodes with reduced surface leakage current', presented at the Optics/Photonics in Security and Defence, Florence, Italy, Oct. 2007, p. 67400H. doi: 10.1117/12.740700.

[11] S. Adachi, 'Optical dispersion relations for GaP, GaAs, GaSb, InP, InAs, InSb, $Al_xGa_{1-x}As$, and $In_{1-x}Ga_xAs_yP_{1-y}$', *J. Appl. Phys.*, vol. 66, no. 12, pp. 6030–6040, Dec. 1989, doi: 10.1063/1.343580.

[12] J. R. Dixon and J. K. Furdyna, 'Measurement of the static dielectric constant of the InSb lattice via gyrotropic sphere resonances', *Solid State Commun.*, vol. 35, no. 2, pp. 195–198, 1980, doi: 10.1016/0038-1098(80)90244-6.

[13] A. S. Verma, N. Pal, B. K. Sarkar, R. Bhandari, and V. K. Jindal, 'Dielectric constants of zinc-blende semiconductors', *Phys. Scr.*, vol. 85, no. 1, p. 015705, Jan. 2012, doi: 10.1088/0031-8949/85/01/015705.

[14] S. Adachi, 'GaAs, AlAs, and $Al_xGa_{1-x}As$: Material parameters for use in research and device applications', *J. Appl. Phys.*, vol. 58, no. 3, pp. R1–R29, Aug. 1985, doi: 10.1063/1.336070.

[15] X. Zhou *et al.*, 'Proton radiation effect on InAs avalanche photodiodes', *Opt. Express*, vol. 25, no. 3, p. 2818, Feb. 2017, doi: 10.1364/OE.25.002818.

[16] L. W. Lim, C. H. Tan, J. S. Ng, J. D. Petticrew, and A. B. Krysa, 'Improved Planar InAs Avalanche Photodiodes With Reduced Dark Current and Increased Responsivity', *J. Light. Technol.*, vol. 37, no. 10, pp. 2375–2379, May 2019, doi: 10.1109/JLT.2019.2905535.

[17] P. J. Ker, J. P. R. David, and C. H. Tan, 'Temperature dependence of gain and excess noise in InAs electron avalanche photodiodes', *Opt. Express*, vol. 20, no. 28, p. 29568, Dec. 2012, doi: 10.1364/OE.20.029568.

[18] A. R. J. Marshall, J. P. R. David, and C. H. Tan, 'Impact Ionization in InAs Electron Avalanche Photodiodes', *IEEE Trans. Electron Devices*, vol. 57, no. 10, pp. 2631–2638, Oct. 2010, doi: 10.1109/TED.2010.2058330.

[19] W. Sun *et al.*, 'High-Gain InAs Avalanche Photodiodes', *IEEE J. QUANTUM Electron.*, vol. 49, no. 2, p. 8, 2013.

[20] Y. Yuan, J. Zheng, A. K. Rockwell, S. D. March, S. R. Bank, and J. C. Campbell, 'AlInAsSb Impact Ionization Coefficients', *IEEE Photonics Technol. Lett.*, vol. 31, no. 4, pp. 315–318, Feb. 2019, doi: 10.1109/LPT.2019.2894114.
[21] P. J. Ker, 'PhD Thesis: Development of high speed low noise InAs electron avalanche photodiodes', in Electronic & Electrical Engineering: The University of Sheffield, 2012.

6. Conclusions

6.1. Conclusion

Short wavelength infrared range has received increasing interest due to its improved eye safety [1] and use for greenhouse gas sensing. Ideal SWIR photodiode characteristics include high quantum efficiency for light detection, low dark current, low capacitance, and low noise at room temperature while maintaining low cost. Currently, competing SWIR photodiode systems depend upon a number of semiconductor materials, including MCT, InAs, ex-InGaAs, InGaAs/GaAsSb type-II superlattice (T2SL) and AlInAsSb. However, the application of SWIR photodetectors brings additional challenges, such as MCT photodiodes are limited to particular space and military applications that can afford their comparatively high cost, ex-InGaAs photodiodes have large lattice mismatch, and InAs photodiodes often require significant cooling to operate. In T2SL structures, the thermal carrier generation is lower than that in the case of a direct band gap transition. The SL period composition has implications on both the signal and the noise of the photodetector, and its optimization can lead to better device performances [2]. With AlInAsSb bandgap tunability, high dark current problems caused by narrow bandgap materials' carrier recombination and band-to-band tunnelling at room temperature can be alleviated by SAM-APD structures. Therefore, two detector materials for the SWIR detection range at ~2 µm, which are InGaAs/GaAsSb type-II superlattice (lattice matched to InP substrates) and $Al_{0.1}In_{0.9}As_{0.83}Sb_{0.17}$ (lattice-matched to GaSb substrates), become more attractive.

In this PhD project, 2-µm cutoff wavelength InGaAs/GaAsSb T2SL *p-i-n* diodes with stained and lattice-matched $GaAs_{1-x}Sb_x$ (x = 0.4 and 0.49) have been demonstrated and characterised. Compared to previous 5nm/5nm T2SL InGaAs/GaAsSb photodiodes, dark current densities of K466 and III-V-5 are at least ~ one order of magnitude lower at a function of temperature from 300 to 180 K. From photoresponse data between room temperature and 200 K, the temperature dependence of the cutoff wavelength can be estimated by linear regression fitting to the η^2 versus wavelength characteristics. These temperature dependence data were utilised to validate the nextnano model for InGaAs/GaAsSb T2SL. After adjusting the GaAsSb valence band offset bowing parameter to -1.06 eV, both lattice-matched and strained T2SL show good agreement over the entire temperature range.

$Al_{0.1}In_{0.9}As_{0.83}Sb_{0.17}$ *p-i-n* photodiodes grown on GaSb (RT E_g: 0.35 eV, cutoff wavelength λ_c: 3540 nm) with 2 and 4 µm intrinsic regions were characterised. Temperature dependent I-V measurements from 295 to 77 K showed that the dark currents of both photodiodes were significantly reduced with decreasing the temperature. Band-to-band tunnelling currents were observed in the narrow bandgap AlInAsSb photodiodes. Compared to InAs APDs, similar dark current but much lower gains can be achieved by AlInAsSb photodiodes. $\alpha > \beta$ can help to design the SAM-APD structures by using narrow bandgap AlInAsSb as the absorption layer material.

6.2. Future work

As mentioned before, the performances of InP based InGaAs/GaAsSb T2SL *p-i-n* photodiodes for the SWIR spectral regions using strain compensated and lattice matched superlattice layers under high operating temperature were presented. The advantages of strain compensated InGaAs/GaAsSb T2SL structures with different Sb compositions have not been fully explored yet, Since the potential to detect SWIR wavelengths of around 2 µm has not been fully accomplished. Further work is to grow strained and lattice-matched InGaAs and GaAsSb T2SL layers with high quality and different compositions. Under strain-compensated conditions, the simulation could be utilised to maximise the transition wavelength and wave function overlap.

The optical and electrical characteristics of $Al_{0.1}In_{0.9}As_{0.83}Sb_{0.17}$ with 3.5 µm cutoff wavelength have been demonstrated. As E_a fitting for temperature dependent I-V data were relatively poor, optimising wafer growth and fabrication techniques is anticipated to produce in wafers with improved performance. By increasing the *i*-region thicknesses, the properties of $Al_{0.1}In_{0.9}As_{0.83}Sb_{0.17}$ APDs may be compared to those of InAs APDs in order to determine their comparability.

Also, the bandgap of $Al_xIn_{1-x}As_ySb_{1-y}$ varies with Al contents [3], Al fraction can be slightly increased from 0.1 to 0.3, which corresponds to the reduced optical cutoff wavelength of approximately 2 µm. The further work could be to investigate 2-µm SAM APD by combining narrow bandgap AlInAsSb absorber ($\alpha > \beta$) and wide bandgap avalanche region ($\alpha > \beta$), and compare 2-µm SAM APD to InGaAs/GaAsSb T2SL *p-i-n* photodiodes. The narrow bandgap of AlInAsSb reveals a significant susceptibility to band-to-band tunnelling current. The

difficulty will be in obtaining an ideal charge layer doping while keeping the low background doping of AlInAsSb absorber in order to minimise energy change across the absorber.

6.3. Reference

[1] K. Scholle, '2 µm Laser Sources and Their Possible Applications', in *Frontiers in Guided Wave Optics and Optoelectronics*, vol. 21, Samir Lamrini, Ed. Rijeka: IntechOpen, 2010. doi: 10.5772/39538.

[2] J. B. Rodriguez, C. Cervera, and P. Christol, 'A type-II superlattice period with a modified InAs to GaSb thickness ratio for midwavelength infrared photodiode performance improvement', *Appl. Phys. Lett.*, vol. 97, no. 25, p. 251113, Dec. 2010, doi: 10.1063/1.3529940.

[3] M. Ren, S. J. Maddox, M. E. Woodson, Y. Chen, S. R. Bank, and J. C. Campbell, 'Characteristics of AlxIn1-xAs ySb1-y (x:0.3-0.7) Avalanche Photodiodes', *J. Light. Technol.*, vol. 35, no. 12, pp. 2380–2384, Jun. 2017, doi: 10.1109/JLT.2017.2681041.

Appendix A: FD05 D Responsivity Graph

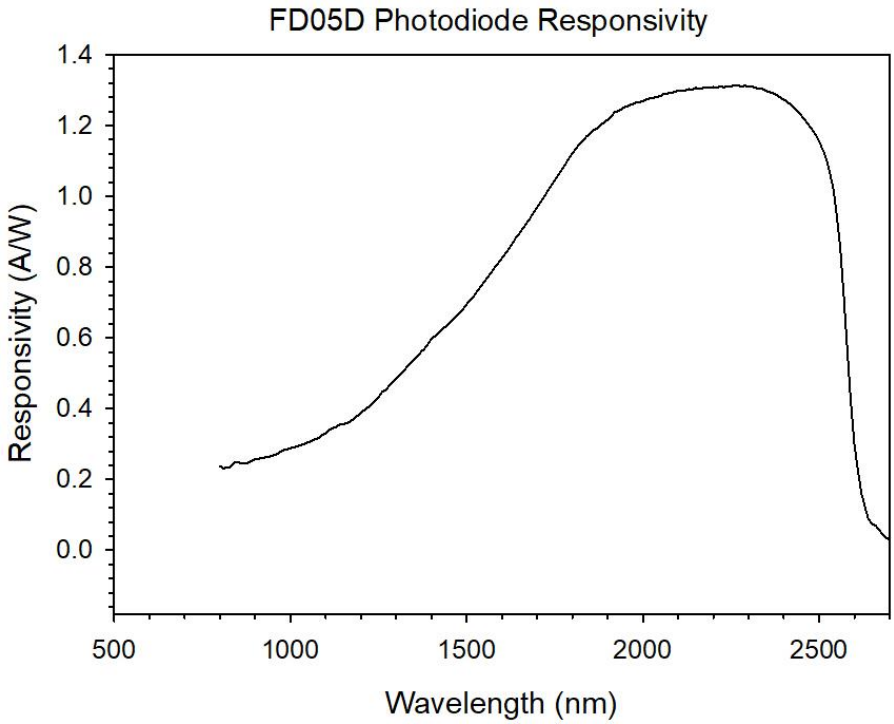

Figure A.0.1: Responsivity varies with the wavelength of the incident light for InGaAs FD05D [1].

[1] 'InGaAs photodiode - FD05D'. Accessed: Jun. 12, 2022. [Online]. Available: https://www.thorlabs.com/drawings/e9ce1ea564cbd16c-773224F4-E0E7-AE18-CBE0C38F41528CC5/FD05D-SpecSheet.pdf

Appendix B: Temperature dependent photoresponse of SF1438

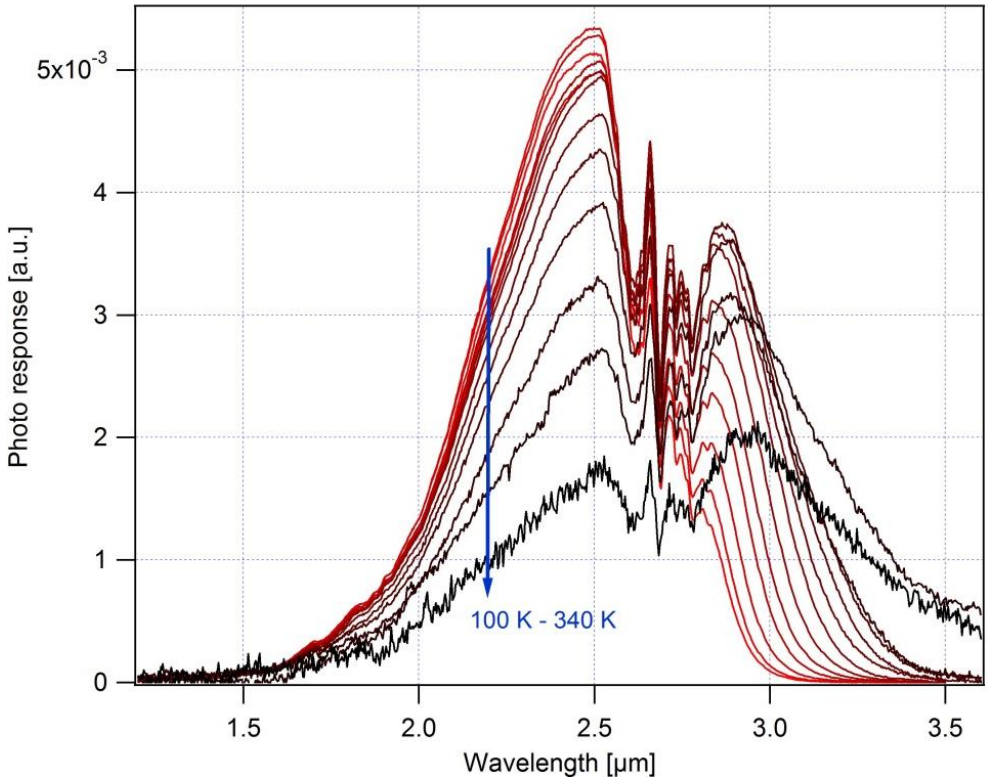

Figure B.0.1: The photo response, in arbitrary unit, of the device with diameter of 420 um on sample SF1438 as a function of temperature from 100 to 340 K.

Appendix C: Effects of background radiation on dark currents

Due to the small bandgap of this material, it was necessary to assess whether photocurrent due to background radiation may affect dark current measurements at low temperatures. Three samples (with different packaging) from the two wafers were used for dark I-V measurements using different setups, as summarised in Table C.0.1. Devices in the probe station is likely to receive more background radiation compared to the liquid helium cryostat due to the probe station having a much bigger sample chamber. Since J-V data of larger diameter devices are more likely to be dominated by bulk leakage mechanism(s), the comparisons below use only J-V data from 420 μm diameter devices.

Table C.0.1. The sample package details.

Wafer	Sample packaging	I-V measurement setup
SF1438	Bare die	Low temperature probe station
	TO-can (with or without lid)	Closed cycle liquid helium cryostat
SF1439	Bare die	Low temperature probe station

Reverse dark J-V of devices in TO-can package were measured as a function of temperature from 340 to 100 K in increments of 20 K. Two sets of measurements were carried out, with or without the lid on the TO-can. The data are compared in Figure C.2. For a given temperature, the measured dark current density from device with lid is lower when those without no lid. The difference is attributed to the lid acting as a cooled shield against the background radiation. J-V data of the bare dies at temperature from 295 to 80 K were obtained from the low temperature probe station, with 80 K being the lower temperature limit of the probe station.

Figure compares temperature dependence of dark current densities at -1 V from the three samples. At temperature above 200 K, data of bara die samples were one order of magnitude higher than those of packaged sample with the lid on. The difference is smaller when compared to the packaged sample without the lid. As temperature decreases, the difference in J_{dark} between bare die samples and packaged sample grows. Hence J_{dark} obtained from bare dies is influenced by background radiation when temperature below 200 K.

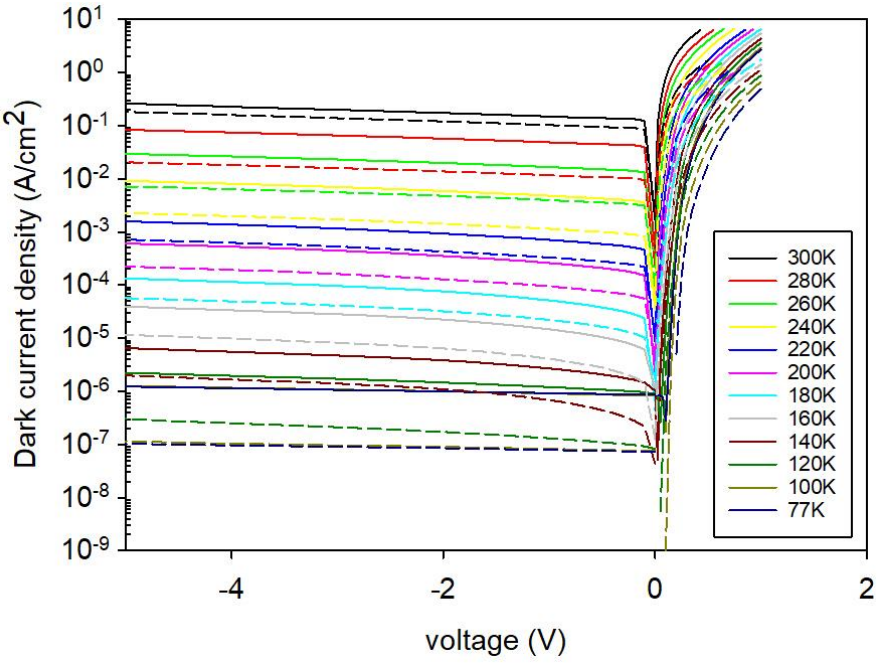

Figure C.2: Comparisons of dark J-V data for SF1438 devices packaged into TO-can, with (dashed lines) or without (solid lines) the TO-can lid, at temperatures from room temperature to 77 K.

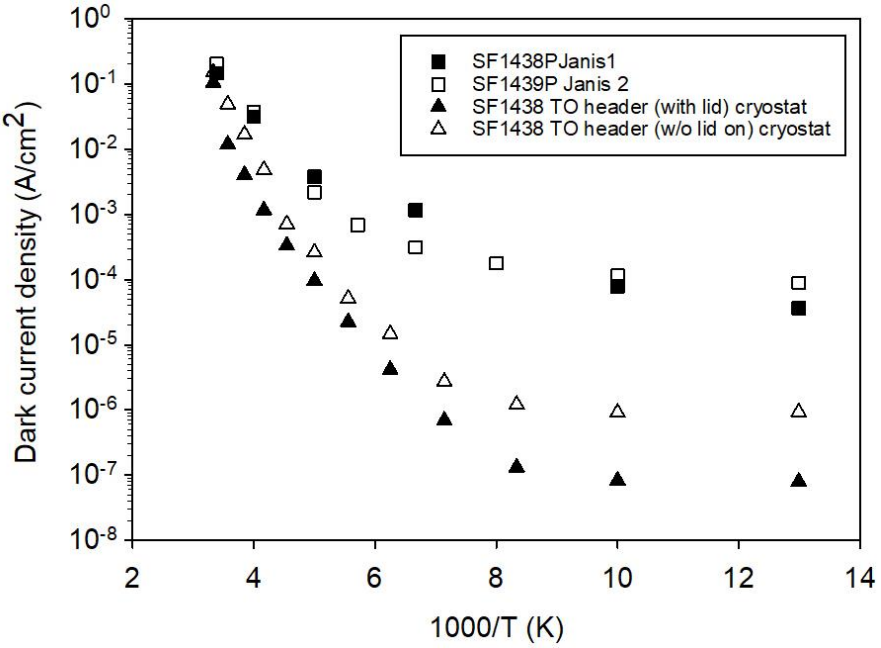

Figure C.3: Comparisons of dark current densities at -1.0 V for bare die and packaged samples at room temperature to 77 K. Data were obtained from 420µm diameter devices.